The Effect of Substrate Stiffness on Endothelial Cell Stiffness and Monolayer Permeability in Response to Inflammation

A Thesis

Submitted to the Faculty

of

Drexel University

by

Rebecca Lownes Urbano

in partial fulfillment of the

requirements for the degree

of

Doctor of Philosophy in Mechanical Engineering

August 2015

© Copyright 2015

Rebecca Jane Urbano. All Rights Reserved.

Acknowledgements

First, I would like to thank my advisor, Dr. Alisa Morss Clyne, for the opportunity to pursue this doctorate degree. You have invested an incredible amount of energy and resources into my development over the past years—for this I can't thank you enough. This time, which has brought me such great personal and professional growth, would not have been possible without your guidance.

I would like to thank my committee members—Dr. Kenneth Barbee, Dr. Alan Lau, Dr. Lin Han, and Dr. Moses Noh—for the time and effort you have dedicated to considering my work and providing thoughtful feedback. I would especially like to thank our collaborator Dr. Patrick Osei-Owusu, who not only helped broaden the scope of this work but also provided very useful advice and enjoyable scientific discussions. I would also like to thank and acknowledge the members of the Osei-Owusu lab—Elizabeth Owens and Li Jie—for their kind assistance with the mouse work.

I feel incredibly fortunate to have found a lab full of friendly and generous people, and this work would have been so much more difficult (and much less enjoyable) without a great group of labmates. Thank you to all the members of the Vascular Kinetics Lab. In particular, thanks to Danni Figueroa and Steve Kemeny for your patience in training me as a new lab member. A big thank you to those of you who shared in the everyday struggles and successes—Justin Mathew, Gary Tang, Stephanie Cicalese, Olivia Ngo, and Adam Canver—I count myself very lucky to have you as both labmates and friends. Some of my best experiences as a doctoral student have come through building strong mentor-mentee relationships with Isabel Buckner and Christina Furia. Thank you for your hard work, but most of all for your enthusiasm; you both have helped and taught me more than you probably realize.

Next I would like to thank my family—both the Lownes and Urbano families—for their constant love and support. Spending time with you at holidays and special occasions always grounded me, brought me joy, and reminded me what is most important in life. Thanks especially to my parents, Bruce and Paula Lownes, who have been my model for work ethic and resiliency. To Kara Spiller and Elise Bryers—your enduring friendship and encouragement have made the hard times easier and the good times even better. Last but not least, I would like to acknowledge my husband, Lenny Urbano. Thank you for your love, humor, and eagerness to learn some biology so that we could have meaningful conversations about my work. You inspire me to strive for the best possible version of myself—this would not have been possible without you.

Table of Contents

List of Tables

List of Figures

Abstract

The Effect of Substrate Stiffness on Endothelial Cell Stiffness and Monolayer Permeability in Response to Inflammation
Rebecca Lownes Urbano
Alisa Morss Clyne, PhD

Cardiovascular diseases represent a major risk to global health, contributing to approximately one-third of all deaths worldwide. Inflammation and arterial stiffening are key in the pathogenesis of many cardiovascular diseases, including hypertension and atherosclerosis. However, little is known about their combined impact on vascular endothelial dysfunction. The central objective of this thesis is to investigate the contribution of arterial stiffness to endothelial cell stiffening and barrier loss in response to inflammation through actinomyosin contractility and reactive oxygen species.

A novel dielectrophoretic (DEP) device for assessing deformability of micropatterned single attached cells was simulated, fabricated, and tested. The device was validated by showing that endothelial cells with cytoskeletal disruption and epithelial cells with induced tumorigenicity were softer by atomic force microscopy (AFM) and more deformable in response to directed DEP pushing force. Next, the effect of sub-endothelial stiffness on endothelial monolayer permeability in response to inflammation was explored *ex vivo* and *in vitro*. Elastin haploinsufficient (ELN+/-) mice exhibited stiffer sub-endothelium by AFM and increased vinculin at aortic endothelial cell-cell junctions. *In vitro,* porcine aortic endothelial cells (PAEC) on collagen-coated polyacrylamide gels of varying stiffness (6-50 kPa) showed increased vinculin localization to cell-cell junctions and junction loss in response to tumor necrosis factor alpha (TNF-α) and thrombin. These effects were abolished when cell contraction was inhibited. Substrate stiffness also enhanced functional barrier loss in response to thrombin, but not TNF-α; however, cells exhibited substrate-dependent stiffening following TNF-α exposure. Lastly, substrate stiffness enhanced endothelial reactive oxygen species (ROS) production in response to phorbol 12-myristate 13-acetate (PMA). On stiff substrates PMA-induced ROS elicited greater actin fiber formation and cell-cell junction loss, which was independent of cell contractility but prevented by ROS scavenging. *Ex vivo*, peripheral actin fiber formation was greater in the ELN+/- mouse abdominal aorta following exposure to PMA.

These results demonstrate that sub-endothelial stiffness affects endothelial cell contractile and non-contractile (ROS-mediated) mechanisms of endothelial barrier dysfunction. This research supports studying the integrated effects of arterials stiffness and inflammation to develop new therapies to prevent endothelial dysfunction.

1. Background

1.1. Clinical motivation

1.1.1. Hypertension

Approximately 37% of American adults suffer from hypertension, according to the Centers for Disease Control and Prevention (CDC, 2011). Recent studies indicate that out of the approximately 76 million hypertensive Americans, 39 million are undiagnosed, untreated or suffer from uncontrolled high blood pressure [1]. Overall, the prevalence of hypertension is approximately equal in men and women. Prevalence steadily increases with age, from about 10% of individuals age 20-34 to about 70% of individuals over the age of 75. Hypertension was a primary or contributing factor in 348,000 deaths in 2009 and costs approximately $47.5 billion annually to treat (CDC). By 2025, the number of individual with hypertension is projected to reach 1.56 billion [2]. Clearly, hypertension is a widespread and costly affliction, and the number of hypertensive individuals will continue to rise as the American population ages.

Hypertension is defined as chronic elevated blood pressure, resulting in cardiac, vascular, renal and/or retinal damage. There are two main classifications of hypertension: primary/essential and secondary. Primary hypertension, which accounts for more than 90% of cases, is not attributable to another pathological condition and can be associated with a myriad of factors. Some of these factors include inappropriate dietary consumption (inadequate calcium/potassium or excessive long-term sodium intake), increased activation of the renin-angiotensin-aldosterone system, increased sympathetic nervous system (SNS) stimulation, and decreased availability of vasodilators. Increased blood pressure as a consequence of other pathologies, including renovascular disease and sleep apnea, is classified as secondary hypertension. The disease progression is characterized into three stages. In the least severe stage, Stage 1, resting blood pressure is >115/75 mm Hg. Individuals in Stage 1 begin to show early signs of hypertensive effects (e.g., increased central arterial or small artery stiffness, increased atrial filling pressure), but do not yet display signs of target organ damage (e.g., mild or severe left ventricular hypertrophy, peripheral or carotid arterial disease). In Stage 2, resting blood pressure is >140/90 mm Hg. Individuals begin to display multiple hypertensive effects and may show signs of early target organ damage. In Stage 3, both resting blood pressure is regularly >140/90 mm Hg or higher and target organ damage has occurred [3].

Hypertension is associated with increased arterial stiffness. Pulse wave velocity (PWV), a direct indicator of arterial stiffness, was 8.6 ± 1.5 m/s in normotensive individuals [4]. In individuals with increased blood pressure, PWV significantly increased to 10 ± 2.5 m/s [5]. In 2001, a large clinical study of 1980 patients showed that increased PWV was significantly associated with cardiovascular mortality in hypertensive individuals [6]. In a larger and more recent clinical study, increased PWV was found to be a predictor of cardiovascular events, even after adjusting for age, sex, systolic blood pressure and cholesterol, among other factors [7]. Interestingly, elevated aortic stiffness was significantly associated with future development of hypertension, suggesting that stiffness changes may precede blood pressure changes [8]. PWV is also correlated with higher cardiovascular mortality, coronary heart disease, and stroke in outwardly healthy older adults [9], and fatal stroke in individuals with hypertension [10].

Several animal models of hypertension exist: diet-induced hypertensive rats and mice (obesity and high salt intake), L-NAME infused rats, Dahl salt-sensitive rats, spontaneously hypertensive rats (SHR), DOCA-salt rats, and elastin haploinsufficient (ELN+/-) mice) [11-13], which can also be used to study the effects of arterial stiffness. Mice fed a high-fat/high-sucrose diet (HFHS) developed stiffened arteries by PWV at 1 month and showed increased systolic blood pressure at 6 months [11]. PWV was approximately 1.4-fold higher in SHR compared to normotensive Wistar-Kyoto (WKY) rats [14]. Thus, arterial stiffening has been shown to precede hypertension in both humans and animal models.

Inflammation plays a role in hypertension, although the exact nature of this role remains to be elucidated. While many inflammatory cytokines exist, this work focuses on the effects of tumor necrosis factor alpha (TNF-α). TNF-α is expressed by several cell types, including macrophages, fibroblasts, neuronal cells, and endothelial cells [15]. Blood levels of TNF-α were elevated in individuals with both hypertension and pre-hypertension, suggesting a role in the progression of the disease [16]. Specifically, TNF-α production by T-cells has been implicated in the hypertension progression [17].

In general, people with hypertension have elevated levels of the inflammatory molecules C-reactive protein, tumor necrosis factor-α (TNF-α), interleukin-6 (IL-6), and adhesion molecules such as P-selectin and sICAM-1 [18]. TNF-α and IL-6 are also elevated in women with preeclampsia [19]. RAG-1-/- mice, which lack both T cells and B cells immune cells, show less hypertension from chronic angiotensin II infusion. Adoptive T cell transfer restored angiotension II-induced hypertension in these mice [20]. These studies further showed that chronic angiotensin II infusion increases activated effector T cells in the circulation and perivascular fat. Thus hypertensive stimuli may lead to activated T cell perivascular accumulation and the local release of cytokines such as TNF-α. In this work, the TNF-α antagonist etanercept reduced hypertension caused by angiotensin II. In a mouse model of hypertension induced through high fructose diet, chronic treatment with etanercept prevented an increase in blood pressure and rescued acetylcholine-stimulated vasodilation and eNOS expression, but did not affect levels of angiotensin II [21]. Inflammation can also increase arterial stiffness through ECM changes [22]. In patients with hypertension, arterial stiffness (measured by pulse wave velocity) was increased in patients with elevated TNF-α levels in the blood, among other inflammatory markers [23].

1.1.2. Atherosclerosis

Atherosclerosis is an inflammatory disease characterized by hardening of the arteries and the formation of sub-endothelial plaques [24, 25]. In early stages of the disease, “fatty streaks” form under the endothelial layer that contain lipids, macrophage foam cells, and T-cells. Low-density lipoprotein (LDL) binding to proteoglycans in the extracellular matrix (ECM) leads to sub-endothelial accumulation, a development which is considered one of the earliest steps in atherosclerotic pathogenesis [26]. Accumulated LDL can be modified through oxidation or enzymatic degradation. This modified LDL stimulates an immune response from surrounding endothelial cells, resulting in up-regulated expression of cell-surface receptors such as vascular-cell adhesion molecule-1 (VCAM-1) that recruit circulating monocytes to the plaque [27]. The plaque continues to grow with increased migration of immune cells into the region and develops a fibrous cap. Eventual plaque rupture leads to clot formation (thrombosis), which can result in the restriction of blood flow to the immediate area or other tissues should the clot become dislodged [24]. In fact, large atherosclerotic plaques (>4mm thick) were associated with brain infarction in individuals older than 60 years of age [28]. While the roles of inflammation and endothelial barrier dysfunction in atherogenesis are well-established, the early triggers are less well understood.

1.1.3. Motivation summary

Hypertension is a major risk factor for atherosclerosis and exacerbates atherogenesis [29, 30]. In addition, recent studies suggest arterial stiffening both precedes and follows increased blood pressure in hypertension [7]. We hypothesize that early reversible increases in arterial stiffness in conjunction with inflammation worsens endothelial barrier loss. This work investigates the mechanisms involved in the substrate-dependent aggravation of endothelial dysfunction (specifically endothelial monolayer permeability) in response to inflammation, as a way to better understand the role of arterial stiffening in the progression of hypertension and atherosclerosis.

1.2. Aorta Structure and Vascular Stiffness

1.2.1. Aortic wall structure

The aortic wall is constructed of three domains moving out radially from the vessel lumen – the tunica intima, the tunica media, and the tunica adventitia [31]. The tunica intima consists of the endothelium, which lines the lumen in a single cell layer and acts as a barrier between the blood and the vessel wall. Beneath the endothelium is a basement membrane consisting of collagen type IV, laminin, and perlecan among other components [32]. The internal elastic lamina (IEL) separates the tunica intima from the tunica media. The tunica media is constructed of alternating layers of vascular smooth muscle cells (VSMC) and elastin lamina, and its outer border is marked by the external elastic lamina. Collagen types I, III, and V are found near the elastin lamina [33]. Collagen type I and III are localized to the tunica media, but absent from the tunica lamina [34]; these two types of collagen make up approximately 90% of the aorta's collagen content [32]. Collagen type IV is found to a lesser extent in the tunica media, although it is distinctly present in the basement membrane of the tunica intima [34]. The outermost layer of the aorta is the tunica adventitia, which contains collagen fibers along with fibroblast and nerve cells. The vasa vasorum is a network of smaller vessels that innervates the tunica adventitia and the outer layers of the tunica media to supply the thickest, most proximal part of the aorta with nutrients [31].

1.2.2. Passive and active control of aortic stiffness

The extracellular matrix (ECM), a protein mesh that mechanically and biochemically supports cells, affects arterial stiffness following changes in the balance of collagen and elastin. Collagen and elastin play complimentary roles in the mechanical behavior of the aorta; elastin confers the vessel its compliance and collagen provides vascular strength [35]. In the arteries of healthy individuals, the vessel ECM is constructed of fenestrated elastin sheets interwoven with collagen fibers (type I and III). The elastin, which is highly distensible, gives the blood vessel its elasticity. Collagen distributed through the elastin meshwork and in the tunica adventitia provides structural support and strengthens the vessel wall, particularly at high strains [35]. At low pressures, when circumferential stretch is low, highly distensible elastin fibers in the aortic wall bear the load while less than 10% of collagen fibers straighten [36]. At higher pressures, when circumferential stretch is high, collagen fibers are engaged and circumferential stress increases with stretch at a faster rate [37]. The importance of elastin in vascular mechanics can be seen in the effects elastin-related diseases and aging.

Arterial stiffening can occur due to changes in extracellular matrix composition or more active processes, such as endothelial cell nitric oxide release and VSMC hypertrophy. Increases in "passive" arterial stiffness can be due to several factors, including decreased elastin content due to degradation by matrix metalloproteases (MMPs) and increased collagen cross-linking by advanced glycation end products (AGEs) [38, 39]. Elastin degradation is also responsible for increased arterial stiffness that occurs with aging [40]. In addition to elastin degradation or cross-linking, genetic deletion results in increased arterial stiffness. In humans, elastin gene (*ELN*) mutations and *ELN* allele deletion (Williams-Beuron syndrome) are both associated with hypertension [41-43]. In genetically modified elastin haploinsufficient (ELN+/-) mice, the elastin layer beneath the endothelial cell layer is severely diminished, and sub-endothelial cell ECM deposition is increased [44]. In one study, arterial compliance was decreased in ELN+/- mice by postnatal day 7; by postnatal day 14, systolic blood pressure in ELN+/- was significantly higher than the wild type [45]. These findings demonstrate that increased blood pressure followed arterial stiffening, suggesting that the increase in pressure was not solely due to decreased elastin content.

Endothelial cells, which line all blood contacting surfaces in the body, control "active" arterial stiffness through production and release of the vasodilator nitric oxide (NO) and the vasoconstrictor endothelin-1. NO is produced by endothelial cells in response to a variety of biochemical and biophysical stimuli, including vascular endothelial growth factor (VEGF), acetylcholine, and shear stress. Upon stimulation, the enzyme endothelial nitric oxide synthase (eNOS) converts oxygen and L-arginine to nitric oxide, producing citrulline as a by-product. NO readily diffuses to the intima media, where it causes VSMC relaxation and an effective decrease in vascular stiffness [46]. Production of NO by eNOS is crucial to blood pressure regulation, as mice lacking eNOS due to genetic mutations (eNOS -/-) display a 15% increase in blood pressure over eNOS +/+ mice [47]. Endothelial cells also produce the peptide endothelin-1 (ET-1), which can cause contraction of VMSC [48]. ET-1 stimulates contraction through increasing intracellular calcium in VSMC; it is also capable of stimulating cell growth and mitogenesis [49]. NO and ET-1 represent two major endothelium-produced effectors of VSMC in the regulation of vascular tone.

Smooth muscle cells, which form the vascular media surrounding the endothelial cells, determine vascular tone through their contractility. VSMC contractility is controlled in part by endothelial cell paracrine signaling through NO and endothelin-1, as previously mentioned. VSMC contraction is also determined by the renin-angiotensin-aldosterone system (RAAS). Angiotensin II, one peptide in this system, acutely stimulates VMSC contraction. Prolonged angiotensin II stimulation results in increased VSMC proliferation (hyperplasia) and increased sized (hypertrophy) in the intima media [50]. Both VSMC hyperplasia and hypertrophy occurs in animal models of hypertension (SHR) [51] and hypertensive humans [52].

The endothelium must react to changes in the complex environment of the aortic wall to maintain vascular homeostasis. Vascular stiffness, controlled actively and passively as described above, is one of the many stimuli experienced by the endothelium. A summary of the literature relevant to endothelial cell response to substrate/tissue stiffness is provided below.

1.3. Cell-matrix attachment

1.3.1. Substrate stiffness introduction

Adherent cell types require a surface on which to attach for proper cell function. *In vivo*, this surface is the tissue in which the particular cell type resides. *In vitro*, plastic tissue culture dishes have historically been used to grow adherent cell types. The term "substrate stiffness" refers to the elastic modulus of the material on which a cell is attached. Most cells *in vivo* attach to soft tissues. The elastic moduli for brain, muscle and bone are approximately 1, 10, and 100 kPa, respectively [53], whereas normal substrates for *in vitro* studies (glass or plastic) are orders of magnitude stiffer. While early studies used thin sheets of silicon rubber, one way of controlling the stiffness of cell culture substrates is the use of polyacrylamide (PA) gels [54, 55]. PA gels are hydrogels formed through the cross-linking of acrylamide and bis-acrylamide monomers. The stiffness of the gel is controlled though the relative amount of acrylamide and bis-acrylamide. Since polyacrylamide is non-adhesive for cells, an ECM protein is covalently linked to the gel surface [56]. One limitation to the use of PA gels for the study of cell-substrate mechanics is their behavior as an elastic material, as opposed to the viscoelastic behavior of most biological tissues [55, 57]. Although protein-conjugated PA gels are far less complex than actual tissue, they provide a means to study the effects of tissue stiffness *in vitro* and have been used extensively is substrate stiffness studies [58].

1.3.2. Endothelial cell response to substrate stiffness

Substrate stiffness affects a wide variety of cell types, including endothelial cells, fibroblasts, breast cancer cells, and stem cells [58, 59]. *In vivo*, tumors are stiffer than their surrounding environment. Specifically, in the MMTV-Neu rat model of breast cancer, mammary gland stiffness increased during the transition from normal to cancerous tissue due to increased ECM collagen cross-linking [60]. In humans, elastography, which uses tissue stiffness measurements to detect disease, is used to diagnose liver fibrosis and breast cancer [61, 62]. In healthy individuals and those with either risk factors for or established coronary artery disease, flow-mediated dilation increased with increasing aortic compliance, indicating an effect of vascular stiffness on endothelial cell function [63].

In vitro studies of cell response to substrate stiffness began when Pelham and Wang first used protein-coated polyacrylamide gels to show that both rat kidney epithelial and 3T3 fibroblast spread to a greater extent on stiff substrates (~0.73 N/m) than soft (~0.046 N/m) substrates [55]. Since that seminal paper, many cells types were shown to change their morphology [64-67], motility [68, 69], differentiation [53, 70] and proliferation [71, 72] in response to substrate stiffness. For endothelial cells specifically, single cell spread area increases with substrate stiffness [73]. When single bovine aortic endothelial cells (BAECs) were grown on polyacrylamide gels of increasing stiffness (180, 2900, or 28600 Pa), cell area increased. However, as cells proliferated and reached confluency, substrate-dependent differences in cell area were no longer observed [74]. BAECs have also been used on type I collagen-coated polyacrylamide gels to demonstrate that both substrate stiffness and ligand density affect endothelial cell network assembly, with enhanced network formation on soft substrates (200 kPa) compared to stiffer substrates (>1000 kPa) [64]. Endothelial cell motility is directed toward areas of higher substrate stiffness, a phenomenon called durotaxis observed in many cell types, as demonstrated by bovine pulmonary arterial endothelial cell movement away from soft PDMS areas (12 kPa) to micropatterned stiff PDMS areas (2.5 MPa) after 24-48 hours [75]. Durotaxis occurs due to several factors, including the force generated by the cell on its substrate, which is referred to as traction force. When single BAECs were seeded on collagen-coated polyacrylmade gels ranging from 1-10 kPa, both cell area and traction stress increased with substrate stiffness [76]. Substrate stiffness can also affect endothelial cell proliferation; the percent of proliferative HUVECs (as measured by BrdU) decreased with decreasing stiffness over a range of 1.72 to 21.5 kPa on fibronectin-coated polyacrylamide gels [77].

Substrate stiffness can modulate cell mechanics. Endothelial cell stiffness (measured by atomic force microscopy), and cell-matrix and cell-cell forces (measured by traction force microscopy) all increased with substrate stiffness [78]. Single endothelial cells show similar stiffening in response to stiffer substrates; individual BAECs on 9 kPa fibronectin-coated polyacrylamide gels were more stiff than cells on 1.7 kPa gels as measured by microaspiration [79]. When in a confluent monolayer, there was a significant increase in HUVEC stiffness on 0.87 kPa versus 280 kPa gels coated with fibronectin; however, no significant difference in cell stiffness was observed between cells on 0.87 or 5 kPa gels [80]. To provide better insight into how endothelials sense and respond to substrate stiffness, cellular structures involved in this process are reviewed in the following sections.

1.3.3. Focal adhesion structure

Focal adhesions

Cellular response to substrate stiffnesss begins at specialized structures called focal adhesions. Focal adhesions are punctate structures at the basolateral cell surface at which specialized proteins that bind the ECM aggregate [81]. Focal adhesions act as conduits of information between the cell's substrate and the inside of the cell. Integrins, discussed in detail below, are a main feature as they span the outer cell membrane and are composed of extracellular ECM-binding domains and intracellular cytoskeletal-linking domains. On the intracellular side of the focal adhesion, integrins bind many proteins that provide structural support, such as the ability to bind the actin cytoskeleton. In fact, more than 50 intracellular proteins have been localized to focal adhesions [82]. Some of these intracellular focal adhesion proteins can also serve as signaling molecules, interacting with other proteins to trigger signaling cascades. Key focal adhesions proteins are detailed below.

Integrins

Integrins are heterodimers of transmembrane proteins largely responsible for the interaction between adherent cells and the ECM, although some non-integrin adhesion receptors exist [83]. All integrins are composed of two sub-units, termed the α and β sub-units. There are 18 α and 8 β sub-units, and these components form 24 known combinations [84]. The particular combination of individual sub-units determines the specificity of the integrin-ECM interaction; for example, $\alpha_2\beta_1$ binds collagen while $\alpha_v\beta_3$ binds multiple proteins including fibronectin and vitronectin [85]. Integrin binding of ECM proteins allows cells to contract and pull against the resistance provided by their environment. This cell-generated force is called a “traction force” [54, 86]. Interestingly, the force that a cell exerts on ECM proteins through integrin interactions can cause the uncoiling of some ECM proteins, such as fibronectin [87]. This applied force reveals previously unavailable cryptic binding sites and allows for increased integrin-ECM interaction.

Integrin binding induces cytoskeletal changes and activates intracellular signaling pathways through the vast number of focal adhesion-associated proteins. Integrins are unable to interact with the actin cytoskeleton directly; actin-binding proteins such as talin, vinculin, filamin, and tensin act as linkers between integrins and the cytoskeleton [88]. Scaffolding proteins, such as paxillin, contain binding sites for multiple proteins and thus contribute to the construction of focal adhesions. Paxillin can bind the signaling proteins focal adhesion kinase (FAK) and Src, both of which are tyrosine kinases and play an important role in integrin-mediated signal transduction pathways [89-91]. Integrins play a role in the RhoA/ROCK signaling pathway, which is key to cell contractility and will be discussed in more detail. For example, applying tension to integrins results in the activation of the RhoA signaling pathway through the guanine nucleotide exchange factors (GEFs) LARG and GEF-H1 [92].

Just as environmental cues are transmitted into the cell through focal adhesions, “inside-out” activation of integrins is also possible, meaning cells can activate integrins prior to extracellular integrin-ECM interaction [93]. For example, talin interaction with the β sub-unit is sufficient for integrin activation without external interactions with ECM proteins [94, 95]. Talin binding to the β3 sub-unit disrupts an inhibitory interaction between the tails of α and β sub-units [96]. In addition, the intracellular protein migfilin also activates β sub-units by displacing filamin from integrins [97]. Filamin also acts as an actin-crosslinking protein; inhibiting “inside-out” integrin activation is not its sole function [98]. Thus, both integrins and the intracellular proteins they interact with are key to focal adhesion structure and function.

Vinculin

Vinculin, a highly conserved 117 kDa intercellular protein, was first described in the literature by Geiger et al. in 1980 and shown to locate to cell-matrix and cell-cell adhesions [99-101]. Study of vinculin’s structure by electron microscopy revealed an N-terminal head, a flexible neck, and a C-terminal tail region [102, 103]. Intramolecular interaction between the head and tail regions results in self-inactivation, masking binding sites for multiple binding partners including talin, actin, α-actinin, and vasodilator-stimulated phosphoprotein (VASP) [104-107]. This self-inactivation can be disrupted by binding of phosphatidylinositol-4,5-bisphosphate (PIP_2) to vinculin’s tail region [108]. Other vinculin binding partners include paxillin, ponsin and vinexin [109-111]. As discussed in the following section, vinculin also binds the cell-cell junction protein alpha-catenin. Due to its ability to bind several cytoskeletal proteins, vinculin plays a key role in regulating a cell’s attachment to its substrate and neighboring cells.

Focal adhesions and mechano-sensing

Focal adhesions are integral to cellular mechano-sensing capability, specifically the ability to differentially respond to substrates of different stiffness [112, 113]. One way that focal adhesions enable mechano-sensing is through cytoplasmic mechano-sensitive proteins at the intracellular side of integrins. For example, talin is unfolded by the application of force, and this unfolding results in the unveiling of a vinculin binding site [114]. Vinculin binding following force application stabilizes the focal adhesion structure [115]. Focal adhesion kinase (FAK) is another intracellular focal adhesion protein involved in mechanosensitive signal transduction. *In vitro* cyclic stretch induces phosphorylation of FAK in multiple endothelial sub-types, including bovine aortic endothelial cells and human lung endothelial cells [116, 117]. In epithelial cells, FAK phosphorylation at Y397 was significantly lower on soft substrates (< 2 kPa) compared to stiff substrates (24 kPa), and FAK activation was linked to Rac-dependent differences in cell cycle progression on substrates of varying compliance [118]. Downstream of FAK, force-activated stretching is also thought to play a role in increased activation of p130Cas, a signaling molecule phosphorylated by Src upstream of Rap-1 [119]. Force-induced unwinding of filamin A, which causes dissociation of the Rac-inactivator FilGAP and unveils cryptic binding cites for the β_7 integrin sub-unit, may also play a role in increased cell contraction on stiffer substrates [120, 121]. Thus, while focal adhesions are key to cell-substrate mechano-sensing, the exact mechanisms involved are still an area of intensive study.

1.3.4. Cell contractility signaling and substrate stiffness

Substrate stiffness determines the level of resistance a cell experiences when it contracts and pulls against the surface to which it is attached. Thus, the study of cell contractility mechanisms is key to better understanding how tissue stiffness, specifically blood vessel wall compliance, modulates cell function. The Rho family of GTPases contains over 20 different proteins; the most widely studied of these are RhoA (Ras homolog gene family, member A), Rac1 (Ras-related C3 botulinum toxin substrate 1), and Cdc42 (Cell division control protein 42 homolog). Rho GTPases are bound by GTP in their activated state or GDP in their inactive state [122]. Guanine nucleotide exchange factors (GEFs), GTPase activating factors (GAPs), and guanine dissociation inhibitors (GDIs) control the activation state of these proteins. GEFs, such as p115RhoGEF, LARG, and GEF-H1, activate Rho GTPases. Interestingly, some GEFs interact with the outer cell membrane and thereby control the localization of Rho activation. GAPs, such as p190RhoGAP and p73RhoGAP, inactivate Rho. GDIs down-regulate Rho activity by blocking Rho GTP activation [123]. Several sub-types of Rho GAPs and GEFs are expressed in endothelial cells *in vitro* and *in vivo*, and play key roles in endothelium barrier function [124, 125].

Although other members of the Rho GTP family also influence actin reorganization, RhoA is particularly important in cell contractility signaling due to its effects on the serine/threonine kinase Rho-associated protein kinase (ROCK). ROCK contains an auto-inhibitory region that is deactivated through interaction with active Rho-GTP. Downstream of RhoA, ROCK increases the pool of active phosphorylated myosin light chain (MLC) through inhibition of MLC phosphatase, which de-phosphorylates

MLC [126]. Active myosin then interacts with the actin cytoskeleton to produce intracellular contractile forces [127].

Myosin light chain kinase (MLCK) also plays a role in modulating cell contractility, controlled through direct interaction with the Ca2+/calmodulin complex. Binding of Ca2+ to calmodulin induces a conformational change necessary for MLCK activation [128]. Interaction with Ca2+/calmodulin releases an auto-inhibitory domain in MLCK and triggers direct phosphorylation of MLC [129]. MLCK can also be activated by other kinases, such as protein kinase A [130]. Activation of MLC induces myosin filament formation along actin fibers [131]. Early studies on myosin phosphorylation, actin fiber formation and endothelium monolayer contractility were conducted using a custom isometric tension monitoring apparatus capable of detecting contractility of endothelial layers in culture. Thrombin-induced contraction of a HUVEC monolayer preceded actin stress fiber formation [132]. In a follow-up study, treatment of HUVECs with thrombin was found to increase phosphorylated myosin at serine-19/threonine-18 and induce co-localization of myosin II with actin fibers, in addition to spurring measurable cell contraction [133]. Traction force microscopy, which measures deformation of a pliable substrate due to cellular forces, is also used to study the state of cell contraction; traction forces of single endothelial cells were diminished following the inhibition of ROCK, indicating decreased cell contractility [86, 134].

Chemical inhibitors of signaling molecules in the contractility pathway are widely available. ROCK can be inhibited by the small molecule Y-27632 [(+)-(*R*)-*trans*-4-(1-aminoethyl)-*N*-(4-pyridyl)cyclohex- anecarboxamide dihydrochloride], which binds to its catalytic site [135, 136]. Multiple inhibitors exist for MLCK, including ML-7 (1-(5-

Iodonaphthalene-1-sulfonyl)-1H-hexahydro-1,4-diazepine hydrochloride) and ML-9 (1-(5-Chloronaphthalenesulfonyl)homopiperazine hydrochloride), which work by binding MLCK near its ATP-binding site [137]. In addition, the small molecule blebbistatin affects myosin directly by preventing its association with actin [138]. While both MLCK and ROCK are instrumental in determining the level of activated myosin, studies suggest their control of actin fiber formation may be specific to different intracellular locations. Interestingly, inhibition of ROCK decreases longitudinal stress fibers while inhibition of MLCK decreases peripheral actin bundles in single fibroblasts [139]. Similar results have been observed in sub-confluent fibroblasts [140].

Rho/ROCK signaling is activated in response to thrombin *in vitro* and *ex vivo*, and thrombin-induced Rho/ROCK signaling is amplified on stiff substrates *in vitro*. Thrombin is a protease in the cascade responsible for blood clot formation [141]. It is known to induce endothelial contraction though the activation of both MLCK and the Rho/ROCK pathways [142]. *In vitro*, treatment with thrombin results in increased levels of phosphorylated MLC in several endothelial cell types [143, 144]. In the endothelium of intact rat renal arteries, pre-treatment with Y-27632 attenuated actin fiber formation and MLC phosphorylation in response to thrombin [145]. Thrombin-stimulated RhoA signaling was increased to a greater extent in cells on 90 kPa polyacrylamide gel versus 1.2 kPa gel [146]. In sub-confluent monolayers of human lung microvascular endothelial cells, MLC phosphorylation magnitude and duration in response to thrombin treatment increased with increasing substrate stiffness (from 0.55 to 42 kPa) [147].

As this dissertation aims to investigate how substrate stiffness affects cell-cell junctions, key intercellular junction components are described below followed by a background on the mechanisms involved in endothelial monolayer permeability.

1.4. Cell-cell attachment

1.4.1. Cell-cell attachment structure

Inter-cellular attachment is crucial to endothelial barrier function. Specialized structures form endothelial cell-cell junctions: tight junctions and adherens junctions. Tight junctions and adherens junctions differ in their components, particularly the transmembrane adhesion proteins that form homophilic linkages between adjacent cells. Claudins, occludin, junctional adhesion molecules (JAMs), and nectin compose tight junctions while cadherins (particularly VE-cadherin in the endothelium) compose adherens junctions [148]. VE-cadherin is supported by several intracellular proteins that link VE-cadherin to the actin cytoskeleton. Discussed in more detail below, α-catenin and β-catenin co-localize at the membrane in adherens junctions. Plakoglobin (γ-catenin) also localizes to adherens junctions, but only in stably confluent monolayers [149]. While endothelial cells expressing truncated VE-cadherin (unable to form the cadherin-catenin complex) formed cell-cell contacts, these cells could not establish an effective barrier to high molecular weight molecules [150]. Thus, the cadherin-catenin complex is necessary for proper endothelial barrier function. In addition to linking VE-cadherin to the cytoskeleton, intracellular adherens junction proteins also play a role in signal transduction pathways. For example, p120-catenin binds VE-cadherin but none of the adherens junction actin-binding proteins; p120-catenin acts as a substrate for the signaling molecule Src [151]. Similar to focal adhesions, adherens junctions represent an area in the cell where structural and signaling components spatially coincide.

VE-cadherin/Cadherin-5

Vascular endothelial cadherin (VE-cadherin) was first identified in 1992 and is an endothelial-specific protein at cell-cell junctions both *in vivo* and *in vitro* [152]. VE-cadherin belongs to the cadherin superfamily of glycoproteins [153, 154]. The superfamily includes several subfamilies: the "classical" cadherins (including E-, N-, P- and VE-cadherin), desmosomal cadherins, proto-cadherins, 7TM-cadherin, T-cadherin, and FAT-family cadherin. Along with VE-cadherin, endothelial cells also express N-cadherin [155]. Most cadherins, excluding T-cadherin, span the cell membrane with both extracellular and intracellular regions. The extracellular region is comprised of multiple cadherin repeats and allows for calcium-dependent homophilic binding of cadherin molecules between adjacent cells [156, 157]. The intracellular tail of VE-cadherin contains several binding sites for other intracellular proteins at cell-cell junctions which link cell-cell junctions to both the actin cytoskeleton and intermediate filaments [158]. Two proteins instrumental in the linkage between VE-cadherin and the actin cytoskeleton—alpha- and beta-catenin—are detailed below.

Alpha-catenin

The role of alpha-catenin (α-catenin) at adherens junctions is still debated and an area of ongoing research [159]. β-catenin binds the intracellular tail of VE-cadherin, and α-catenin binds β-catenin forming the cadherin-catenin complex [160, 161]. Alpha-catenin is capable of binding actin directly [162]; however, the ability of α-catenin to simultaneously bind VE-cadherin/β-catenin and actin was called into question [163, 164]. Recently, an *in vitro* optical trap-based assay using purified VE-cadherin, β-catenin, α-catenin and F-actin demonstrated that tension strengthens the interaction between the cadherin-catenin complex and F-actin up until approximately 10 pN of applied force, after which the duration of the bond decreases [165]. In addition to its direct interaction with actin, α-catenin also binds several other actin-binding adherens junction proteins including vinculin and α-actinin, an intracellular adherens junction protein very similar sequence to vinculin [166].

Beta-catenin

Beta-catenin (β-catenin) was first identified as a 92 kDa cadherin-associating protein in epithelial cells in 1991 [167]. β-catenin is highly conserved and structurally similar to γ-catenin, another intracellular cell-cell junction protein [168]. Conditional deletion of β-catenin in mice resulted in pericardial swelling and other vascular abnormalities; *in vitro* endothelial cells lacking β-catenin exhibited low levels of α-catenin at cell-cell junctions and lack of barrier function [169]. Aside from its role in stabilizing adherens junctions, β-catenin functions as a nuclear co-transcription factor in T-cell factor/leukocyte enhancing factor (TCF/LEF) inducible gene transcription [170]. The behavior of β-catenin as a co-transcription factor has been well-studied as part of the Wnt signaling pathway in non-vascular cells; however, recent evidence suggests possible cross-talk between the Wnt pathway and cell-cell junction signaling through β-catenin in vascular development and disease [171]. For example, in thrombin-treated HUVECs cell-cell junction disruption increased nuclear p120-catenin and β-catenin, where it induced target gene expression [172]. In addition, increased TCF/β-catenin transcription was observed in both sub-confluent and VE-cadherin-null cells [173]. Thus, there exists some interaction between β-catenin's roles as an adherens junction protein and co-transcription factor. This work, however, will focus only on β-catenin at cell-cell junctions.

1.4.2. Effect of force on adherens junctions

Forces at adherens junctions increase as cells contract. Similar to the force-responsive elements of focal adhesions, certain proteins localized to adherens junctions are sensitive to changes in intracellular tension. For example, the three dimensional structure of α-catenin endows this protein with mechano-sensitive properties. Specifically, the application of tension (~5 pN) to α-catenin using magnetic tweezers causes it to unfold and unveil a binding site for vinculin; vinculin binding then prevents α-catenin refolding [174]. Local creation of tension by magnetic twisting cytometry with E-cadherin coated beads in MDCK epithelial cells resulted in vinculin recruitment that required α-catenin [175]. In multiple studies, treatment of several epithelial cell types with blebbistatin abolished vinculin from apical cell-cell junctions [176, 177]. In HUVECs vinculin was recruited to adherens junctions following VEGF, TNF-α, and thrombin treatment; vinculin localization to junctions was abolished by the Rho inhibitor C3 transferase, Y-27632, blebbistatin, and a VE-cadherin blocking antibody (to disrupt VE-cadherin homophilic intercellular binding). Interestingly, the cell-cell junctions of HUVECs expressing an α-catenin variant without the vinculin binding site were disrupted more severely and took more time to reform following thrombin treatment, compared to the control. This study suggested that vinculin recruitment to adherens junctions functions to reinforce cell-cell contacts in response to tension [178].

While increased tension at cell-cell junctions is often associated with junction loss, some basal level of force is needed for proper maintenance of junctions. Using a non-endothelial cell type (C2 mouse myogenic cells), it was shown that single cells spread to a greater extent on stiffer cadherin-coated polyacrylamide gel surfaces, and that blebbistatin treatment to inhibit cell contractility abolished cadherin adhesions [179]. Cellular traction forces can be measured using arrays of polydimethylsiloxane (PDMS) microneedles, and these substrates have also been used to better understand the relationship between cell-matrix forces and cell-cell junctions. Human pulmonary artery endothelial cells (HPAECs) were seeded on micropatterned microneedle arrays to form interacting cell pairs of controlled size and shape, and the size of the junctional area between the cell pair was determined using β-catenin labeling. Treatment of cells with blebbistatin and Y-27632 decreased both the force at the junction (calculated using the traction force) and the junction size. However, treatment with thrombin also decreased junction size [180]. These and similar studies have indicated that the state of endothelial adherens junctions is force-sensitive.

1.4.3. Mechanisms of adherens junction disruption

The disruption of adherens junctions can occur due to several mechanisms. Two types of mechanisms key to this work are discussed below—barrier disruption due to cellular contractility and the production of reactive oxygen species.

Contractility dependent adherens junction disruption: Rho/ROCK-mediated permeability

The role of Rho signaling in endothelial monolayer permeability is well-established and plays a role in barrier disruption due to several agents, such as thrombin, lipopolysaccharide (LPS), TNF-α, and VEGF [181]. *In vitro*, the ROCK inhibitor Y-27632 prevented thrombin-induced adherens junction disruption and decreased the diffusion of fluorescent molecules through bovine pulmonary arterial endothelial cell monolayers [182]. In addition, Y-27632 has been shown to attenuate barrier loss in bovine pulmonary artery endothelial monolayers following thrombin treatment using transendothelial resistance (TER, also known as transendothelial electrical resistance or TEER) [143]. While TNF-α activation of the Rho family of proteins is well-established, the role of cell contraction in TNF-α-induced endothelial permeability is more controversial [183, 184]. In HUVECs, phospho-MLC was increased after 30 minutes of TNF-α treatment, but inhibition by Y-27632 or ML-7 was reported to not prevent TNF-α-stimulated endothelial permeability; however, these inhibitors were only added to the culture for the last hour of a 24-hour TNF-α treatment [185]. Y-27632 did not attenuate HUVEC endothelial permeability measured by TER following TNF-α; in this study Y-27632 was added 30 minutes after treatment with TNF-α [186]. Yet, in another work, Y-27632 did prevent adherens junction disruption due to TNF-α [187]. In other studies using human lung microvascular endothelial cells, Y-27632 did prevent TNF-α-induced permeability by TER [188]. The role of contractility in endothelial permeability following exposure to TNF-α may depend on endothelial sub-type (i.e. macrovascular or microvascular) and represents an area of active research.

Contractility independent adherens junction disruption: Reactive oxygen species

Endothelial cells produce reactive oxygen species (ROS), which are highly reactive oxygen-containing molecules including superoxide (O_2^-), hydrogen peroxide

(H_2O_2), hydroxyl radical ($^{\bullet}OH$), and peroxynitrite ($ONOO^-$). In the endothelium, ROS can play both physiological and pathological roles and have been implicated in both hypertension and atherosclerosis [189]. ROS are formed in response to a variety of stimuli, including peptides (angiotensin II, endothelin-1), growth factors (VEGF), cytokines (TNF-α), and shear stress. Both NADPH oxidase and xanthine oxidase produce superoxide; superoxide dismutase converts superoxide to hydrogen peroxide [190]. Specifically, NADPH oxidase was shown to produce the majority of superoxide in cultured bovine coronary artery endothelial cells [191]. NADPH oxidase function requires the translocation of multiple sub-units, including Rac, p40phox, p47phox, p67phox, and NOX (NOX-1, 2, 3, 4, or 5) [192]. The NOX-2 homolog (also known as gp91phox) has been implicated in endothelial-dependent aortic relaxation; the aortae of NOX-2 knock-out mice (gp91phox-/-) displayed greater acetylcholine-induced relaxation compared to aortae from the wild-type mice, and this difference was abolished by treatment with the superoxide scavenger tiron [193]. Both p47phox and Rac play key roles in the control of NADPH oxidase assembly and activation [194, 195]. Interestingly, Rac activation affects both actin redistribution and superoxide production, and the balance between these dual responsibilities may be determined by the specific Rac GEF involved [183, 196, 197].

ROS production is known to induce actin fiber formation and disrupt endothelial cell-cell junctions. The interaction between ROS and actin can be both direct and indirect, through physical modification of actin and stimulation of intracellular signaling pathways, respectively. [198]. Effects of superoxide and its byproduct hydrogen peroxide on actin fibers have been demonstrated in many studies, although the observed changes in actin structure may be dependent on endothelial cell sub-type and oxidant source [199]. Actin stress fibers formed in sub-confluent re-oxygenated hypoxic cultured aortic endothelial cells. In this study actin fiber formation was inhibited by overexpression of superoxide dismutase, suggesting a key role for the sustained presence of superoxide [200]. In migrating mouse aortic endothelial cells, incorporation of actin monomers into actin fibers was diminished following treatment with the NADPH oxidase inhibitor diphenylene iodonium (DPI) and a superoxide dismutase mimetic [201]. In the protrusions of epithelial cells, treatment of cells with H_2O_2 resulted in increased actin polymerization, increased cofilin activity, and increased barbed ends; interestingly, myosin IIA did not co-localize with actin fibers in protrusions of H_2O_2-treated cells [202]. In addition to its role in actin remodeling, ROS may increase endothelial permeability through mediating the phosphorylation of adherens junctions proteins. Phosphorylation of adherens junction proteins is associated with junction disruption; treatment of cultured endothelial cells with permeability agonists, such as VEGF and histamine, results in tyrosine phosphorylation of VE-cadherin [203, 204]. In HUVECs, treatment with the ROS scavenger N-acetyl-L-cysteine (NAC), prevented the phosphorylation of VE-cadherin following TNF-α [205]. In HUVECs, transduction with a constitutively active form of Rac (Tat-RacV12) resulted in actin fiber formation, increased ROS production, increase monolayer permeability and phosphorylation of α-catenin but not VE-cadherin; α-catenin phosphorylation was diminished through ROS scavenging by NAC [206].

One well-characterized inducer of ROS in endothelial cells is phorbol 12-myristate 13-acetate (PMA, also known as 12-O-tetradecanoylphorbol-13-acetate or

TPA). PMA is known to increase ROS production in endothelial cells; 1 µM of PMA resulted in near-immediate increased detection of ROS in HUVECs [193]. Bovine pulmonary artery endothelial (BPAEC) monolayer integrity, as measured by TER, was maximally disrupted by 100 nM PMA after ~90 mins of treatment [207]. Junction loss has been observed at even earlier timepoints (30 min) in other endothelial cell types [208]. In BPAEC, actin fibers formed within 5 minutes of treatment and eventually formed a grid-like pattern; only stress fibers formed in human pulmonary endothelial cells (HPAEC) without formation of the actin grid. Both mono-phosphorylated (Ser19 p-MLC) and di-phosphorylated (Ser19/Thr18 pp-MLC) MLC co-localized with actin fibers. However, in this study PMA did not increase overall phosphorylated MLC by Western blot or MLCK activity, and did not induce wrinkling of the silicon membrane to which the cells were attached (indicating lack of contractility) [207]. In a separate study using BPAEC, PMA did not induce MLC phosphorylation but did increase monolayer permeability [144]. Actin fiber redistribution aside from contractility may be key in PMA-induced endothelial permeability, as stabilizing actin fibers with phalloidin prevented PMA-induced monolayer disruption by TER [209]. PMA initiates intracellular signaling through interaction with protein kinase C (PKC) [210]. Activation of PKC occurs rapidly; after 5 minutes of treatment with 100 nM PMA, 95% of total PKC was found in the membrane fraction of confluent BPAECs, indicating activation [211]. Blocking PKC using calphostin C prevented monolayer disruption produced by PMA [212]. These studies suggest PMA-induced ROS production causes endothelial junction disruption due mainly to actin redistribution instead of increased contractility.

1.4.4. Evidence for substrate-dependent adherens junction disruption and ROS production

While stiffer substrates have been shown to decrease endothelial barrier function *in vitro*, few studies have investigated the role of substrate stiffness on cytokine-induced endothelial permeability. Increasing substrate stiffness from 2.5 to 10 kPa increased the permeability of an unstimulated bovine aortic endothelial cell (BAEC) monolayer through a ROCK-dependent mechanism. *In vivo*, aged mice (20-25 months) showed increased subendothelial stiffness by atomic force microscopy (AFM) and greater permeability to Evan's blue dye compared to young mice (9 weeks) [134]. In groups of confluent HUVECs, thrombin produced greater traction forces and cells experienced greater separation on 11 and 90 kPa PA gels compared to 1.2 kPa gels [213]. One *in vivo* study tested the hypothesis that lung stiffening due to lysyl oxidase ECM cross-linking worsened permeability in response to LPS. Mice treated with the irreversible LOX inhibitor β-aminopropyl nitrile (BAPN) showed decreased LPS-induced pulmonary uptake of injected Evan's blue dye. Interestingly, BAPN treatment also lessened the expression of the RhoGEF GEF-H1 following LPS administration [214].

There is also support in the literature for the hypothesis that substrate stiffness will increase agonist-stimulated ROS production. In sub-confluent epithelial cells, treatment with matrix metalloproteinase 3 (MMP3) induced more ROS with increasing substrate stiffness between 130 and 4020 Pa through a Rac1b-dependent mechanism. Specifically, Rac1b (a highly active variant of Rac1) translated to the membrane on stiff substrates but not soft substrates. In addition, MMP3-induced ROS production was eliminated by knock-down of the β_1 integrin sub-unit [215]. This suggests a link between substrate stiffness, integrin activation, and ROS production. It is known that integrin activation affects Rac localization to the membrane. Rac1 was localized to the membrane in attached fibroblasts but not fibroblasts in suspension. In addition, the activity of the Rac1 effector PAK was increased following serum stimulation of attached but not suspended fibroblasts [216]. Later studies indicated that integrin activation may mediate Rac1 localization through control of lipid rafts [217]. Treatment of bovine coronary arterial endothelial cells with Fas ligand (FasL) induced the clustering of lipid rafts co-localized with gp91phox. Additionally, in bovine small intramural coronary arteries, the prevention of bradykinin-induced vasorelaxation by FasL was attenuated by pre-incubation with apocynin (NADPH oxidase inhibitor) or nystatin (lipid raft disruptor) [218]. In fact, NADPH oxidase may localize to caveolae, a subset of lipid rafts. Constituents of NADPH oxidase (gp91phox, p47phox, and p22phox) were found in caveolae of cultured bovine aortic endothelial cells, and cholesterol depletion inhibited production of superoxide following treatment with either TNF-α or angiotensin II [219]. These studies suggest an integrin-mediated component to NAPDH oxidase control, possibly through lipid rafts; yet, the connection between substrate stiffness and ROS production in confluent endothelial monolayers has not been well-studied.

While these studies support a possible role for substrate stiffness in modulating endothelial barrier loss in response to permeability agonists through contractile and non-contractile (ROS-mediated) pathways, additional study is needed to better understand the interplay between biomechanical and biochemical stimuli in the inflamed endothelium.

1.5. Endothelial cell stiffness

1.5.1. Relation to endothelial cell function

Endothelial cells, in addition to acting as a barrier between the blood and the vessel wall, actively control arterial stiffness through production and release of vasodilators; as previously mentioned, one key vasodilator is nitric oxide (NO). While changes in the actin fiber structure have been implicated in increased endothelial permeability, the actin cytoskeleton is almost a major determinant of endothelial cell stiffness. Endothelial cell stiffness has been linked to the ability to produce NO. Stiffness of both human dermal microvascular endothelial cells (HMEC) and an immortalized HUVEC cell line (EA.hy926) within confluent monolayers anti-correlated with NO concentration over a TNF-α timecourse, as determined by atomic force microscopy and the Griess assay, respectively [220]. One proposed reason for this observation was disruption of the interaction between eNOS and G-actin, which is known to enhance eNOS activity, as G-actin is integrated into actin fibers [221]. Similarly, actin fiber disruption by cytochalasin D (thus increasing the available pool of G-actin) increased NO production in BAECs within a confluent monolayer [222]. The relationship between endothelial stiffening and increased blood pressure due to insufficient NO production has recently been termed “stiff endothelial cell syndrome” [223]. Thus, improved tools for studying endothelial cell stiffness will enhance the study into the mechanisms behind the development of hypertension.

1.5.2. Current analytical techniques

A wide variety of methods exist to test cell mechanical properties. Through techniques such as micropipette aspiration [224, 225], optical tweezers [226, 227], and the optical stretcher [228, 229], forces can be applied across the entire cell to enable measurement of whole cell stiffness. Alternatively, magnetic bead microrheometry [230], magnetic twisting cytometry [113, 231], and atomic force microscopy (AFM) [232, 233] apply forces to specific cell locations to measure the stiffness of specific cellular regions. AFM is widely used to measure cell stiffness and is described in detail below.

The atomic force microscope is a multi-functional instrument consisting of a cantilever used to apply force to a sample and a laser-based detection system to measure the resulting cantilever deflection [232]. It was originally developed in 1986 as a modification to the scanning tunneling microscope (STM), which can only examine conductive samples. The AFM enables researchers to study a vast range of materials under a variety of conditions in both air and liquid [234]. Briefly, at the end of the cantilever is a small tip, usually pyramidal or spherical in geometry. The instrument controls the movement of the cantilever and brings the tip into contact with the sample surface. The control of cantilever movement in the z-direction is generally accomplished using two modes: contact and tapping mode. In contact mode the tip remains in contact with the surface, scanning over areas of the substrate and constructing a topograph. In tapping mode the tip is oscillated over the surface at a user-defined frequency. AFM is often used for studying material mechanical properties (reviewed in [235, 236]). Cantilever deflection is detected using a laser beam, which reflects off the cantilever and hits a photodiode. The deflection can be transformed into force using Hooke's law based on the stiffness coefficient of the cantilever.

Researchers have adapted the AFM to serve many purposes due to its elegant design and ability for high resolution. Its development and application to numerous areas of research have been well reviewed [234, 237]. In addition to the determination of cell stiffness [238, 239], other uses include measurement of the elastic modulus for soft and stiff materials [240], single molecule recognition and interaction [241, 242], imaging of crystals [243], and patterning of molecules with nanoscale resolution [244], among several others. In this work, AFM is used for the measurement of cell, substrate, and sub-endothelial stiffness.

1.5.3. Dielectrophoresis

Dielectrophoresis (DEP) is the force induced on a polarizable particle in a spatially non-uniform electric field. When a polarizable object is placed in an electric field, charges distribute unevenly across the body to create a dipole. In a uniform electric field, this dipole experiences no net force. However, in a non-uniform electric field, the forces exerted on each dipole end are unequal, leading to a net force on the dipole. The force direction is determined by competition between the induced polarization in the cell and the medium. If the cell is less polarizable than the medium, the overall effective dipole draws the particle towards the field minimum (negative DEP) [245, 246].

Dielectrophoresis (DEP) has been effectively used for many biological applications involving bioparticle manipulation. DEP traps immobilized micron sized particles, beads and cells, as well as submicron sized viruses into large arrays using both positive and negative DEP [245, 247-250]. DEP can separate different cell populations based on their dielectric properties. Breast cancer cells have been detected in blood [251], and CD34+ stem cells were enriched from a larger stem cell pool [252]. Additionally, DEP has been used to pattern cells on uncoated substrates [253], on microprinted adhesive regions [254], or within a three-dimensional hydrogel [255]. DEP has also been used to study the morphology and mechanics of floating, unattached cells. Changes in T cell membrane architecture, either during stimulation or apoptosis, were measured by DEP [256, 257]. High DEP forces stretched cell membranes to the point of failure, leading to either cell fission in sea urchin eggs [258] or plasma membrane leakage in erythrocytes [259]. Recently, the mechanical properties of a wide variety of suspended cell types, including Chinese hamster ovarian cells, U937 human promonocytes [260], cancerous (MCF-7) and noncancerous (MCF-10A) breast epithelial cells [261], and cervical cancer cells (SiHa and ME180)[262] were measured using DEP devices. Despite great interest in biological applications for DEP, dielectrophoretic forces have not been used to study global mechanical properties of attached cells.

1.6. Objectives and hypothesis

Arterial stiffness, as measured by pulse wave velocity *in vivo*, is an independent predictor of future cardiovascular events including the development of hypertension and cardiovascular mortality. In addition, hypertension is a major risk factor for atherosclerosis, which develops in part to a loss of endothelial barrier function. In this thesis, arterial stiffness in simulated *in vitro* using polyacrylamide gel substrates of varying stiffness and investigated *ex vivo* using an elastin haploinsufficient mouse model of hypertension. **The central objective of this thesis is to investigate the contribution of arterial stiffness to endothelial cell stiffness and barrier loss through increased**

endothelial cell actinomyosin contractility and reactive oxygen species production. The underlying hypothesis are:

- Dielectrophoresis can be used for measuring changes in single attached cell stiffness following actin cytoskeleton disruption
- Substrate stiffness exacerbates TNF-α-induced disruption of adherens junctions in endothelial cell monolayers through increased cell contractility
- Endothelial cell production of reactive oxygen species is greater on stiff substrates than soft substrates

1.7. Thesis organization

This thesis is composed of five chapters.

Chapter 1 includes the clinical motivation for this work and a summary of relevant background information from the literature, including macroscale aortic structure, cell-matrix attachment, cell-cell attachment, and endothelial cell stiffness. The background is followed by the aims and organization of this thesis.

Chapter 2 presents the development of a dielectrophoretic device used to measure relative changes in single attached cell deformability, including device simulation and microfabrication. Device operation was validated with atomic force microscopy elasticity measurements of single micropatterned cells.

Chapter 3 presents the effect of increasing substrate stiffness (simulating increasing aortic stiffness) on endothelial cell-cell junction loss following treatment with the inflammatory molecules tumor necrosis factor alpha and thrombin. This chapter includes the atomic force microscopy characterization of sub-endothelial stiffness of aortae from genetically modified elastin haploinsufficient mice (ELN+/-, a mouse model of hypertension), in addition to immunofluorescent microscopy labeling of the mouse aortic endothelium.

Chapter 4 presents the effect of increasing substrate stiffness on endothelial production of reactive oxygen species (ROS) and cell-cell junction loss following treatment with the protein kinase C (PKC) agonist phorbol 12-myristate 13-acetate (PMA). This chapter also compares PMA-induced actin redistribution in the aortic endothelium of wild type and ELN+/- mouse vessels.

Chapter 5 concludes the thesis with a discussion of contributions to the field and future work.

2. Microfabrication and validation of a dielectrophoretic device for measurement of attached single cell stiffness

2.1. Introduction

Recently, microfabricated lab-on-a-chip devices for the analysis of single cells have gained popularity [263]. Many miniaturized devices used to study single cells employ microfluidics for high through-put analysis of cell suspensions [264]. However, the use of cells in suspension prevents the study of the effects of cell attachment to a substrate, as most cell types are attached to the surrounding tissue in the body. While endothelial cells exist in a monolayer *in vivo*, the study of single attached cells provides a simplified system that can be used to separate out the relative contributions of cell-matrix and cell-cell interactions. In addition, the study of multiple single cells provides information on the variability among individual cells within a population, as opposed to other methods that pool millions of cells and provide aggregate values. The objective of the device presented in this chapter is to measure the stiffness of single attached cells.

Cell stiffness is mainly determined by the actin cytoskeleton, which has both structural and functional roles within the cell. Along with other cytoskeletal elements, such as microtubules and intermediate filaments, actin fibers provide internal structural support; actin fibers are under tension while microtubules are thought to bear compressive loads [265]. In endothelial cells monomeric actin interacts with the nitric oxide (NO) producing enzyme eNOS to enhance NO production [221]. Thus, the depletion of monomeric actin through actin polymerization into filaments increases cell stiffness while decreasing NO production [222]. Improved analytical tools for measuring cell stiffness will improve our understanding of the link between cell stiffness and endothelial function.

In this chapter, I present the simulation, microfabrication, and testing of an inverted quadrupole dielectrophoretic device. The inverted design of this device is novel and grants several advantages to the study of single attached cell stiffness. Device operation was demonstrated in two scenarios: (1) the comparison of endothelial cells with and without actin cytoskeleton disruption and (2) the comparison of tumorigenic (MCF-10A NeuT) and non-tumorigenic (MCF-10A) mammary epithelial cells. Both these conditions (actin disruption and induced tumorigenicity in MCF-10A cells) have previously been shown to affect cell stiffness [266, 267]. Device validation was demonstrated through comparison with the gold standard for attached cell stiffness, atomic force microscopy.

2.2. Methods

2.2.1. Electric and force field modeling

A quadrupole electrode configuration was simulated using the three-dimensional AC/DC module of COMSOL Multiphysics software (version 4.3a). The quadrupole electrode device was designed as four opposing electrodes (40 μm diameter) with a central space (60 μm diameter) large enough to enable the electrodes to be lowered over a single attached cell. Since the device is symmetrical, half of the device was modeled in COMSOL. Voltages and ground were set as shown in Figure 2.1a. A range of voltages was simulated using the root mean square voltage corresponding to each peak-to-peak voltage (V_{pp}) in Table 2.1 [268]. Frequency was set to 1 MHz. Distributed impedance boundary conditions were set along the sides and top of the modeled electrode, and the bottom surface was set as an electrically insulating boundary. The DEP force was defined as [269]:

$$F_{DEP} = 2\pi\varepsilon_m r^3 Re[CM(\omega)]\nabla|E|^2$$

where ε_m, r, ω, and E are relative medium permittivity, cell radius, angular frequency, and electric field strength, respectively. For a spherical particle, the Clausius-Mossotti factor (CM) was defined as:

$$CM = \frac{\varepsilon_p^* - \varepsilon_m^*}{\varepsilon_p^* + 2\varepsilon_m^*}$$

where ε_p^* and ε_m^* are the complex permittivities of the particle and the medium, respectively. The complex permittivity of the medium was calculated as:

$$\varepsilon_m^* = \varepsilon_m + \frac{\sigma_m}{j\omega}$$

where is σ_m the conductivity of the medium [253]. The complex permittivity of the cell was determined using the spherical shell model:

$$\varepsilon_p^* = \varepsilon_s^* \left[\frac{\left(\frac{r}{r-d}\right)^3 + 2\left(\frac{\varepsilon_{int}^* - \varepsilon_s^*}{\varepsilon_{int}^* + 2\varepsilon_s^*}\right)}{\left(\frac{r}{r-d}\right)^3 - \left(\frac{\varepsilon_{int}^* - \varepsilon_s^*}{\varepsilon_{int}^* + 2\varepsilon_s^*}\right)} \right]$$

where ε_s^* and ε_{int}^* are the complex permittivities of the cell shell (membrane) and cell interior, respectively, and d is the width of the cell membrane. As derived in [270], this equation simplifies to:

$$\varepsilon_p^* = r\left[C_{spec} - \frac{jG_{spec}}{\omega}\right]$$

where C_{spec} and G_{spec} indicate the specific membrane capacitance and the specific membrane conductance, respectively. The dielectric properties of mammalian cells, specifically HL-60 cells, have been published in the literature [262, 271]. In our model, specific membrane capacitance and specific membrane conductance were set to 0.016 F/m^2 and 2200 S/m^2, respectively [272]. Cell culture medium conductivity (σ_m) and permittivity (ε_m) were defined as 1.5 S/m and 80, respectively, based on our measurements and the literature [273]. The cell conductivity and permittivity were defined as 0.75 S/m and 75 [274]. Cell radius was set as 10 µm.

2.2.2. Device design and fabrication

The quadrupole DEP device was manufactured using standard microfabrication techniques. Square glass substrates (2” x 2”) were selected for the device base to allow for cell observation using an inverted microscope. The device photomask was designed in AutoCAD and printed at high resolution onto a transparent film (JD Photo-Tools). A 4” x 4” chrome plate pre-coated with negative SU-8 photo resist (Telic) was exposed to ultraviolet light through the transparency mask, baked, and developed to produce the patterned chrome mask. The chrome mask was then used to create the electrodes by sequential deposition of titanium and gold, where titanium was used to enhance gold adhesion to glass [253, 274]. Futurrex NR9-1000PY (Futurrex) was chosen as the photoresist since it can withstand the high temperatures required for metal deposition. Titanium and gold were then sequentially deposited by physical vapor deposition in a thermal evaporator (Thermionics VE 90) at 20 nm and 200 nm thickness, respectively. Photoresist and excess metal were removed using RDG developer.

Electrical leads were created by soldering copper wire strands onto electrode connector pads. The soldered pads were strengthened and sealed from the cell medium by curing a thin layer of polydimethlysiloxane (PDMS, Sylgard, Dow Corning) over the connector pads. Electrode thickness was then increased by gold electroplating. The device was submerged in non-cyanide gold electroplating solution (Technigold 25E RTU, Technic) maintained between 60-70°C with constant stirring. Gold was deposited by pulse plating (500 mVpp) with a 10% duty cycle using a function generator (BK Precision 4010) at a deposition rate of approximately 0.013 μm/minute. Final electrode thickness following electroplating was confirmed by optical profilometry (Zygo NewView 6000).

2.2.3. Polyacrylamide gel micropatterning

PDMS stamps for microcontact printing were fabricated using standard soft photolithography methods. Transparency film photomasks with a 25 μm diameter circle array were printed (JD Photo-Tools). SU-8 2025 (Microchem) was spin-coated on a glass substrate, soft baked, exposed for 3 minutes using a UV lamp (NuArc 26-1K Mercury Exposure System), post-exposure baked, developed in SU-8 developer and then hard baked. To ease PDMS release, the SU-8 mold was coated with (tridecafluoro-1,1,2,2-tetrahydro octyl)-1-trichlorosilane (UCT) by vapor deposition. PDMS was mixed using a 10:1 ratio of base to curing agent, degassed, poured onto the mold and cured at 70°C for at least three hours.

Micropatterned polyacrylamide (PA) gels were made by indirect microcontact printing [275]. A top coverslip was patterned with fibronectin using a PDMS stamp. Stamps were incubated with a mixture of biotinylated tetramethylrhodamine-BSA (5 μg/mL, Invitrogen) for pattern visualization and biotinylated human plasma fibronectin (50 μg/mL, Gibco) for 40 minutes. The protein solution was then removed from the stamps, which were dried and immediately placed onto plasma-cleaned glass coverslips (5 mm for DEP device samples or 12 mm for AFM samples) for 5 minutes. A streptavidin polyacrylamide (PA) gel solution was created by adding 0.1 mg/mL streptavidin-acrylamide (Invitrogen) to a PA solution of 10% acrylamide (BioRad), 0.3% bis-acrylamide (BioRad), 1% ammonium persulfate (BioRad), and 0.3% TEMED (BioRad). A bottom coverslip was activated by sequential incubation in 0.1 M NaOH (Sigma Aldrich), (3-aminopropyl)trimethoxysilane (Sigma Aldrich), and 0.5% glutaradehyde (Polysciences) for 30 minutes. The streptavidin-PA solution was added to the bottom coverslip, after which the micropatterned top coverslip was quickly inverted over the polymerizing gel. Polymerization was completed in a 37°C, 5% CO_2 incubator for 15 minutes, after which the top coverslip was removed. The micropatterned PA gel was then rinsed thoroughly and stored in PBS at 4°C for a maximum of 2 days prior to use.

2.2.4. Cell culture

Primary porcine aortic endothelial cells (PAEC) were isolated by the collagenase dispersion method and cultured in low glucose Dulbecco's Modified Eagle's medium (DMEM, Corning) supplemented with 5% fetal bovine serum (Hyclone), 1% glutamine, and 1% penicillin-streptomycin (Invitrogen). Cells were used up to passage 8. Mammary epithelial cells (MCF-10A) and transformed mammary epithelial cells (MCF-10A NeuT) were a gift from Dr. Adrian Shieh. Cells were maintained in DMEM/F12 (Corning) supplemented with 5% horse serum (Atlanta Biologicals), 20 ng/mL epidermal growth factor (Peprotech), 500 ng/mL hydrocortisone (Sigma), 10 ng/mL cholera toxin (Enzo Lifesciences), 10 μg/mL insulin (Sigma), and 1% penicillin-streptomycin (Invitrogen). Cells were released from tissue culture dishes with trypsin, seeded onto micropatterned PA gels, and allowed to attach for 30 minutes. Unattached cells were then removed by replacing the medium. Cells were then incubated on the micropatterned PA gels for 16-24 hours prior to mechanics testing. For both AFM and DEP device testing, cells were transferred into serum-free CO_2-independent medium (Invitrogen). In some samples, the actin cytoskeleton was disrupted with 200 nM cytochalasin D (Sigma Aldrich) for 15 minutes at room temperature in serum-free CO_2-independent medium.

2.2.5. Immunofluorescence

Endothelial cells attached to a micropatterned PA gel were fixed using 4% paraformaldehyde (Sigma Aldrich), permeabilized using 0.1% TritonX-100 (EMD Millipore) and rinsed using PBS. To prevent non-specific binding, samples were blocked with 1% BSA in PBS. Cells were labeled for vinculin using a primary mouse antivinculin antibody (1:100, Sigma), followed by an AlexaFluor 488 anti-mouse secondary antibody (1:100, Invitrogen). Actin and nuclei were labeled using rhodamine phalloidin (16.5 nM, Invitrogen) and bisbenzimide (0.2 μg/mL, Invitrogen), respectively. Images were taken using an Olympus Fluoview 1000 confocal microscope.

2.2.6. Atomic force microscopy

Atomic force microscopy (AFM, Veeco Bioscope) was used to validate DEP device cell stiffness measurements (elastic modulus). A silicon nitride cantilever with 1 μm spherical tip (196 μm long, 23 μm wide, 600 nm thick, spring constant 0.06 N/m, Novascan) was used to indent each measured cell at three distinct locations. Relative stiffness was estimated by fitting the first 200 nm of the indentation curves to the Hertz model as previously described [276]. Three measurements per cell were averaged and defined as the cell stiffness.

2.2.7. Sequential application of DEP "pushing" and "centering" forces

First, a micropatterned single cell array on a PA gel was mounted on an inverted Olympus IX81 fluorescent microscope. The extruded quadrupole DEP device was attached to a micromanipulator (Eppendorf), and the electrodes were lowered over a single cell. The cell was positioned in the device center with the electrodes approximately 10 μm above the cell.

A directed DEP "pushing" force, created by applying unequal voltages to two opposing electrodes, was used to deform the cell in a specified direction. Electrical potential was applied using a function generator (BK Precision 3011B) set to 21 Vpp, 1

MHz; the other two electrodes were grounded. The function generator positive lead was diverted into two separate lines, each going to a resistance decade box before connecting to diagonally opposing device electrodes. With no extra resistance applied, opposing electrodes received the same voltage. As resistance between the function generator and one of the electrodes was increased using the resistance decade box, unequal volt ages were applied to opposing electrodes which created the directed DEP pushing force. Thus, increasing resistance to one electrode controlled pushing force magnitude and direction. A DEP "centering" force, created by applying equal voltage to two opposing electrodes, was used to return the cell to its original position in the device center.

The directed DEP pushing force was applied to a cell for 15 seconds. The decade box resistance was then returned to zero for the next 15 seconds to apply the DEP centering force. For each test sequence, 15 seconds of directed pushing force was followed by 15 seconds of centering force.

2.2.8. Image processing

During pushing sequences, brightfield images were taken every 0.5 seconds. Image processing was completed using Matlab's Image Processing Toolbox (Mathworks). Image sequences were cropped to include the area immediately surrounding the cell. Each cropped frame in the image sequence was then binarized to isolate the cell body as a single connected component. The threshold for binarization was determined by Otsu's method using the "greythresh" function [277]. If needed, a multiplier was used to adjust the threshold for a sequence to prevent any debris in the vicinity from being counted as part of the cell. The two-dimensional cell centroid was determined for each frame using Matlab's "regionprops" function. Cell centroid displacement was quantified by measuring the distance between the cell centroid and the lower left corner of the cropped image. The lower left corner of the cropped image was chosen because directed DEP pushing force was consistently applied towards the upper right corner of the image; thus, when the cell deformed, the distance between the cell centroid and the lower left corner of the image increased. All measurements were then normalized relative to the initial cell position at the beginning of the pushing sequence.

2.2.9. Statistical Analysis

Statistical analyses were conducted using Matlab's statistics toolbox. Data are shown as mean ± standard deviation. Experiments were performed in duplicate, and the number of cells per experiment is indicated in the figure caption. For data shown in Figure 5c and 6c, Student's t-test was used to compare two groups. Comparison of multiple groups in Figures 5b and 6b was completed using two-way ANOVA with a Tukey-Kramer post-test. Statistical significance is indicated by #$p<0.05$, *$p<0.01$, or **$p<0.001$.

2.3. Results

2.3.1. DEP device modeling

The extruded quadrupole DEP device was modelled in three dimensions in COMSOL to simulate DEP forces (Figure 2.1a). The set of voltages given in Table 2.1 was evaluated, corresponding to the increasing resistance applied between the power source and Electrode 2. The simulation predicted that a cell in the device center would experience negative DEP, toward the lower voltage Electrode 2, as is expected for cells in highly conductive media [278]. As an example, the simulation results for 2000 Ω are given in Figure 2.1. The electric field strength was highest near the higher voltage Electrode 1 (Figure 2.1b). Figure 2.1c indicates the predicted DEP force in the x-direction that would be experienced by a cell centered at each location within the device. DEP force in the x-direction is toward the right near Electrode 1 and toward the left near Electrode 2 (Figure 2.1c). For a cell positioned in the device center (indicated by the asterisk), DEP force is directed toward Electrode 2 because the higher voltage at Electrode 1 moves the location of zero force towards Electrode 2.We refer to this force at the device center with unequal applied voltages as the directed DEP "pushing" force.

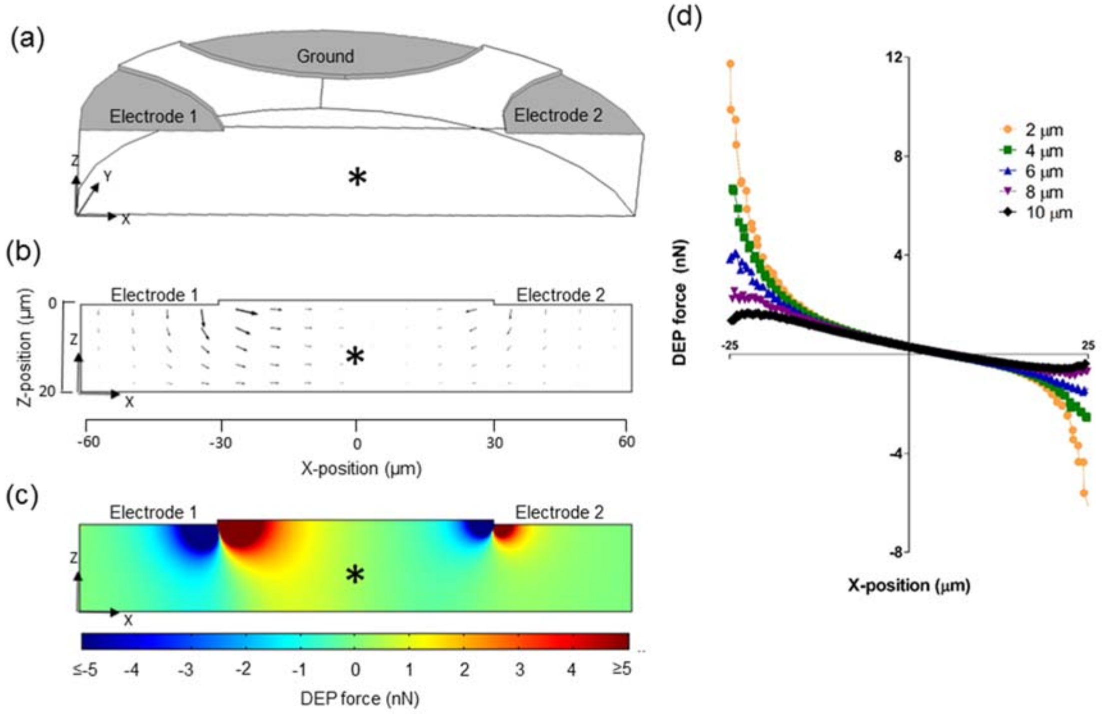

Figure 2.1. COMSOL simulation results predicted negative DEP pushing force in the center of an inverted quadrupole device (a) Half of an inverted quadrupole DEP device was modelled, taking advantage of the device symmetry. Voltage at Electrode 1 was held constant while voltage at Electrode 2 was varied. The asterisk (*) indicates the approximate cell position in relation to the electrodes, 10 µm beneath the inverted device. (b) Predicted electric field strength. Arrows

indicate the relative magnitude and direction of the electric field in the center xz-plane between Electrodes 1 and 2. (c) Predicted DEP force. The DEP force magnitude in the x-direction predicted for a cell centered at each location in the device in the xz-plane at the device center. Positive values indicate net force toward the right, while negative values indicate net force toward the left at each location. Cell radius was 10 μm. (d) DEP force in the x-direction at the device center in the xz-plane was evaluated at increasing intervals below the device. DEP force was consistent at x=0 at distances between 2 and 10 μm away from the device.

Directed DEP pushing force was plotted as a function of position along the x axis connecting Electrodes 1 and 2 at increasing distances from the device surface. Figure 2.1d shows the predicted DEP forces for 2000 Ω, when 21 Vpp (7.42 Vrms) was applied to Electrode 1 and 13.6 Vpp (4.81 Vrms) was applied to Electrode 2. As expected, the directed DEP pushing force magnitude was greatest near the high voltage Electrode 1 and closest to the device surface (2 μm). However at the device center where the cell is positioned (x=0), directed DEP pushing force remained approximately 0.35 nN in the x-direction from 2-10 μm below the device surface, at this applied voltage. The model therefore predicts that small deviations in the electrode z position would have little effect on the DEP force experienced by the cell.

Table 2.1. Applied DEP force for varied voltages across opposing electrodes. The voltage at Electrode 2 was lowered by applying increasing levels of resistance (shown in the first column) between the power source and the electrode.

Resistance (Ω)	Voltage at Electrode 1 (V_{pp})	Voltage at Electrode 2 (V_{pp})	Predicted DEP force (nN)
100	21	20.7	0.02
200	21	20.5	0.03
300	21	20.3	0.04
400	21	19.8	0.07
1000	21	17.8	0.17
2000	21	13.6	0.35
3000	21	10.7	0.44
4000	21	8.3	0.51

Table 2.1 summarizes the predicted DEP pushing forces experienced by the cell in the device center, 10 μm below the device surface. Predicted directed DEP pushing forces ranged from 0.02 to 0.51 nN. These forces are similar to those generated in other single cell mechanics devices. For example, single suspended fibroblast deformation was achieved using approximately 0.2 to 0.5 nN in an optical stretching device [279]. Red blood cells were stretched with optical tweezers by applying forces of up to 0.056 nN to opposite sides of each cell [226]. Micropipette aspiration applies between 10 pN and 1 nN depending on the cell type [280]. Magnetic tweezers can also apply forces within the same range, from 10 pN to more than 1 nN [281]. Atomic force microscopy using large 25 μm spherical tips has also been used to evaluate whole cell stiffness by applying nN-magnitude forces [282].

2.3.2. DEP device microfabrication and experimental set-up

The fabricated DEP device consisted of a quadrupole electrode configuration on a single glass microscope slide (Figure 2.2a). The electrodes increased in width as they extended outward from the quadrupole at a 45° angle, finally attaching to a 2 mm square electrode pad for connecting wires to function generators. Magnified images of a single quadrupole electrode show well-defined rounded electrode tips (Figure 2.2b, c). The final electroplated device thickness was 1.1 μm, as measured by optical prolifometry (Figure 2.2d). The DEP device was connected to a function generator using 2 resistance decade boxes so that voltage could be modulated across opposing electrodes while maintaining the electrodes in phase (Figure 2.2e). The device was then attached to a micromanipulator arm, which was assembled on a microscope stage. The micromanipulator was used to center and lower the DEP device over a polystyrene bead or single micropatterned cell, using the microscope for manual optical guidance (Figure 2.2f).

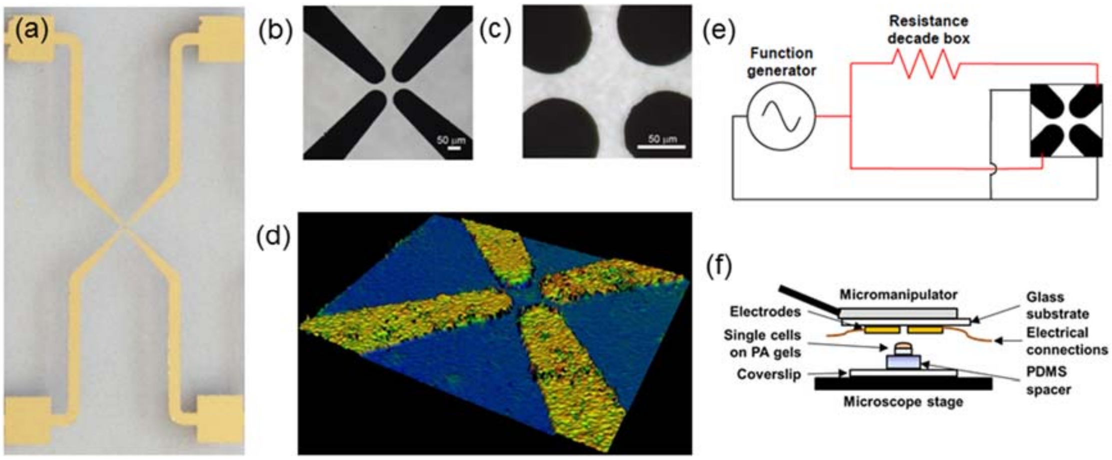

Figure 2.2. Microfabricated DEP device and experimental set-up. (a) Microfabricated DEP device showing one set of quadrupole electrodes with wire connection pads, (b) and (c) magnified images of a quadrupole device showing four electrodes and center space, and (d) optical profilometer image of the ~1.1 μm extruded gold electrodes. (e) Electrical connections diagram. Opposing electrodes were connected to a single function generator using two resistance decade boxes to modulate applied voltage without altering phase. (f) Device schematic, with gold electrodes on glass substrate inverted over single cell array on PA gel.

Operation of the inverted device was tested in preliminary studies by placing the electrodes over a single 10 μm polystyrene bead in suspension (Figure 2.3a). When 10 V_{pp} was applied to both electrodes, the bead was trapped in the device center where DEP force was zeo (Figure 2.3b). When the resistance to the upper right electrode was increased (4, 40 or 400 kΩ), the voltage to that electrode was effectively decreased (4, 1.4, and 1.2 V_{pp}, respectively). Initially, the bead was pushed out of the device center by the directed DEP pushing force. The bead then became trapped in the zero DEP force location (Figure 2.3c). Brightfield image frames taken every 0.5 seconds were processed to measure bead movement following application of DEP force. The bead moved faster and further with increasing electric field gradient strength (Figure 2.3d).

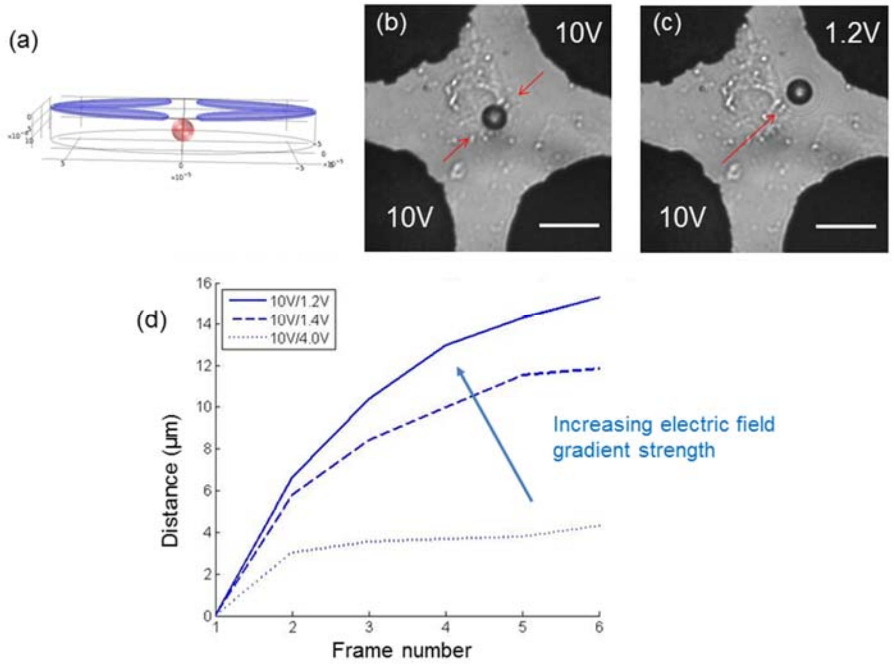

Figure 2.3. A polystyrene bead (10 μm in diameter) was manipulated using inverted electrodes. (a) Schematic illustrating the center of the electrodes as the device is lowered over a single polystyrene bead. A single bead was first trapped (b) then pushed (c), scale bar is 25 μm. Red arrows indicate the direction of the forces applied to the bead based on the voltages applied to the electrodes (either 1.2Vpp or 10 Vpp). A video of bead manipulation was captured and deconstructed into individual frames. (d) Analysis of bead movement between frames showed increasing velocity and distance with increasing electric field gradient.

To prepare cell samples for testing with the inverted DEP device, single cells of defined spread area were created using micropatterned PA gels. An indirect micropatterning technique produced an array of 25 μm diameter fibronectin circles, with TMR-BSA added to the fibronectin to enable fluorescent imaging (Figure 2.4a). The average spot diameter on a typical patterned PA gel was 24.9 ± 3.1 μm. Cells were seeded on the micropatterned PA gels and incubated overnight, resulting in single cell arrays (Figure 2.4b). Cell adhesion quality was confirmed by labeling cells for vinculin and actin and imaging samples by confocal microscopy at the cell base. Punctate vinculin colocalized with peripheral actin fibers suggested that single cells on micropatterned PA gels formed focal adhesions by 16 hours (Figure 2.4c).

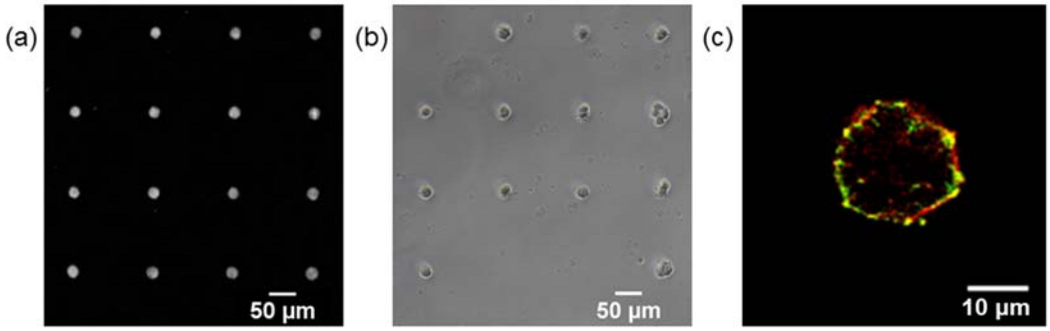

Figure 2.4. Porcine aortic endothelial cells were micropatterned onto 25 µm fibronectin circles to control spread area while allowing cell attachment. (a) Fibronectin (with TMR-BSA to enable fluorescent imaging) circles were patterned onto a PA gel by an indirect micropatterning technique. (b) Cells adhered and spread on fibronectin circles following overnight incubation. Only circles with a single attached cell were used for analysis. (c) A single cell attached to the micropatterned PA gel exhibited punctate focal adhesions (vinculin antibody, green) colocalized with peripheral actin fibers (rhodamine phalloidin, red).

2.3.3. DEP device validation

A single adhered porcine aortic endothelial cell was sequentially deformed using increasing DEP forces (increasing ΔV across opposing electrodes). The extent of cell centroid displacement was quantified by image analysis. Figure 2.5a and 2.5b show representative pre-processed cell images before and during the pushing force, respectively. The corresponding binarized images, which were used to find the cell centroid displacement at each time frame, are shown in Figure 2.5c and 2.5d.

When voltage to Electrode 2 was lowered, the cell centroid moved toward the low voltage electrode (in the predicted DEP force direction). When the same voltage was restored to both electrodes, the cell centroid recovered towards its original position. As the voltage was lowered further on Electrode 2, and therefore the applied DEP force increased, cell centroid movement also increased. For 0.3 ΔV (predicted force 0.02 nN), the cell centroid moved 0.64 µm, whereas at 12.7 ΔV (predicted force 0.51 nN), the cell centroid moved 1.5 µm (Figure 2.5e). Cell centroid movement plateaued at 7.4 ΔV (predicted force 0.35 nN). From these data, 0.5, 1.2, and 7.4 ΔV (predicted forces 0.03, 0.07, and 0.35 nN) were selected for future experiments since they were within the linear deformation range (Figure 2.5e).

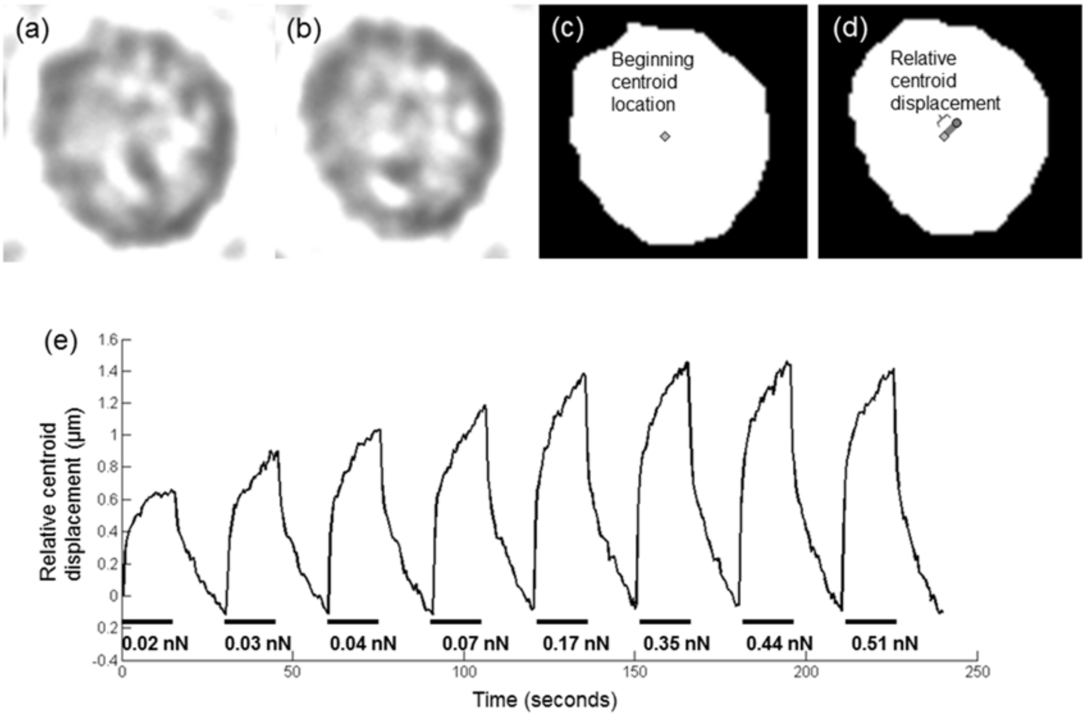

Figure 2.5. Cell deformation increased with applied directed DEP pushing force, up to a maximum deformation level. Increasing directed DEP forces (different voltage on opposing electrodes) were applied to deform a single cell for 15 seconds each, with 15 seconds of restoring “centering force” (same voltage on opposing electrodes) applied between each deformation.

Brightfield images were taken every 0.5 seconds. Representative brightfield images are shown before (a) and during (b) the pushing force application. Images were converted to binary in Matlab (c and d). The cell centroid was defined in each image, represented by a diamond in (c) and a circle in (d). Cell deformation was quantified as the change in distance between the cell centroid and a defined point outside the cell. (e) Directed DEP pushing forces of increasing magnitude were sequentially applied to a single micropatterned porcine aortic endothelial cell.

Porcine aortic endothelial cells were treated with cytochalasin D to determine if the DEP device could measure stiffness changes among cells. Cytochalasin D inhibits actin polymerization and is known to decrease cell stiffness [266]. Untreated endothelial cells showed average centroid displacements of 0.47, 0.62, and 0.88 μm with predicted DEP forces of 0.03, 0.07 and 0.35 nN (Figure 2.6b). Centroid movement increased 58 - 64% in cytochalasin treated cells. Interestingly, cell centroid restoration to the center position was slower in cytochalasin treated cells (Figure 2.6a). This observation supports the role of the actin cytoskeleton in cell elasticity, while the cytosol exhibits viscous properties [283]. In fact, treatment of adherent endothelial cells with 0.1 μg/mL (~2 μM) cytochalasin D has been shown to decrease stiffness while having little effect on cell viscosity by magnetic twisting cytometry [284]. AFM confirmed that cytochalasin treatment decreased stiffness of micropatterned cells. The calculated cell elastic modulus in cytochalasin treated cells was 6-fold lower than untreated cells (0.3 vs. 1.8 kPa, Figure 2.6c).

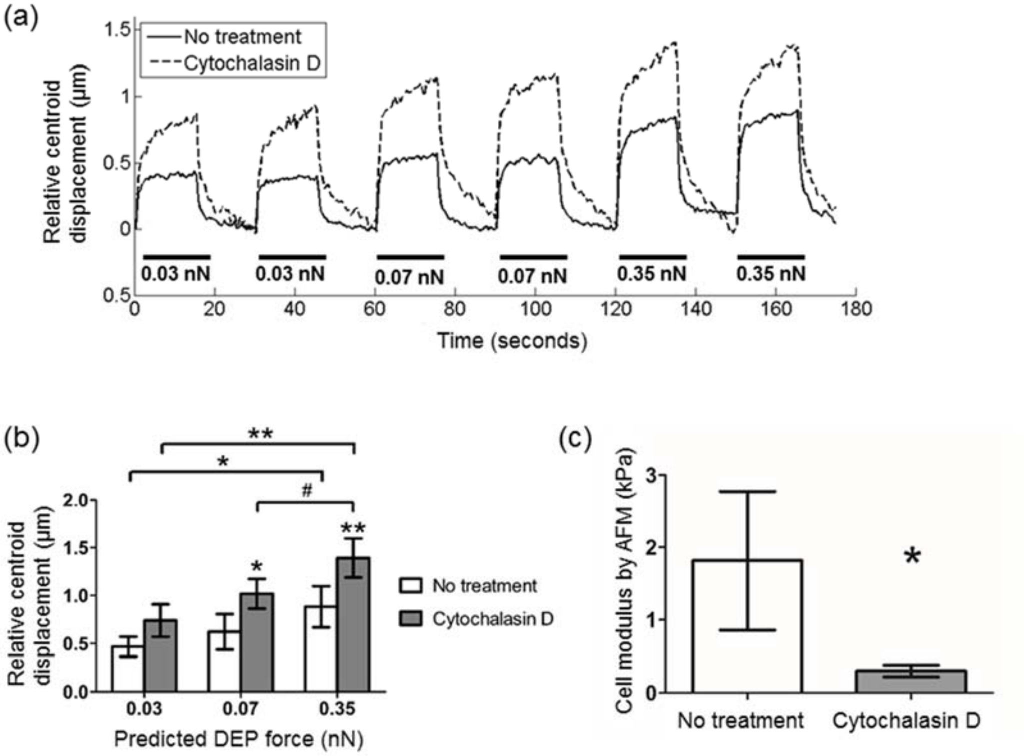

Figure 2.6. When the actin cytoskeleton was disrupted with cytochalasin D, cell centroid displacement in response to applied DEP force increased as compared to untreated cells. (a) Porcine aortic endothelial cells were incubated on micropatterned PA gels overnight, and then treated with 200 nM cytochalasin D for 15 minutes at room temperature. Single untreated and treated cells were subjected to six sequential pushing forces (three DEP force magnitudes, two pushes per force magnitude) for 15 seconds each. Representative data for one untreated and one treated cell. (b) Cell centroid displacement was quantified at each predicted DEP force. Data are mean ± standard deviation ($n = 3$ cells per condition, 2 deformations per cell at each force level). #$p < 0.05$, *$p < 0.01$, **$p < 0.001$ compared to untreated values at each force level, unless brackets indicate otherwise (Tukey's test). (c) Identically treated cells were indented by AFM using a silicon nitride cantilever with 1 μm spherical tip to measure cell elastic modulus. Cell modulus was estimated by fitting the first 200 nm of the indentation curve to the Hertz model (*$p < 0.01$, $n = 6$ cells per condition).

Finally, the DEP device was used to measured changes in cell stiffness among normal (MCF10A) and cancerous (MCF10A-NeuT) breast epithelial cell phenotypes.

MCF10A-NeuT cell centroid displacement was 61-84% higher than MCF10A cells, with larger differences at higher applied DEP forces (Figure 2.7a, b). Similarly by AFM, the modulus of MCF10A cells was 56% higher than the modulus of MCF10A-NeuT cells (Figure 2.7c). These data confirm that the DEP device can detect cell stiffness differences among different cell types.

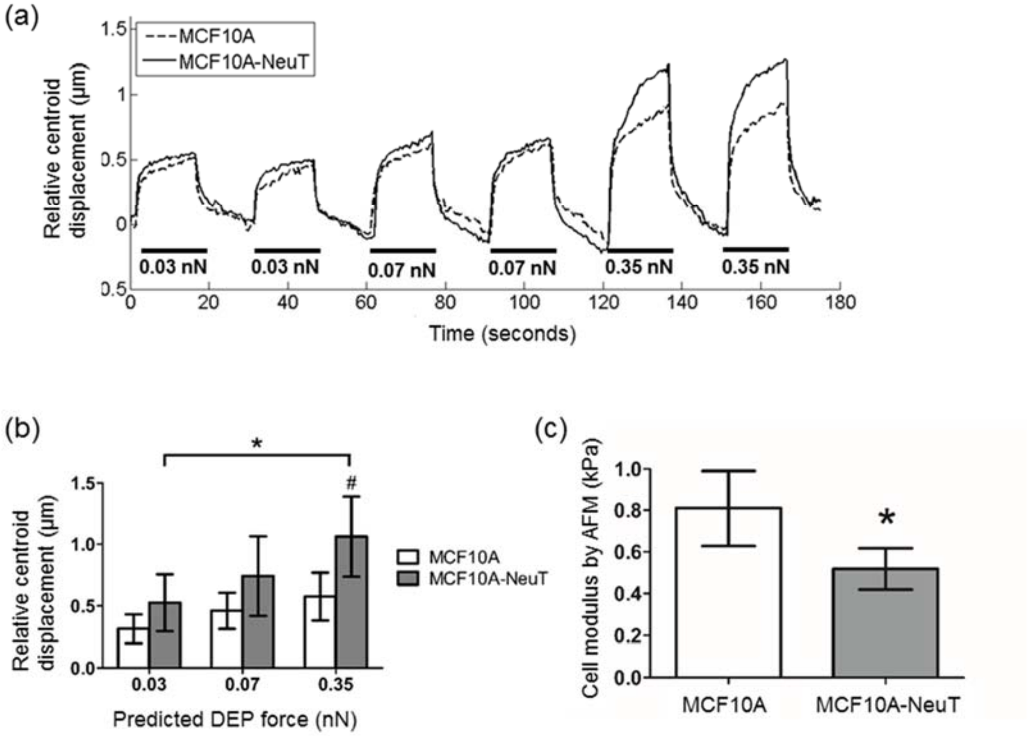

Figure 2.7. MCF10A-NeuT cells showed greater cell centroid displacement than MCF10A cells by DEP, as well as lower cell modulus by AFM. (a) Micropatterned MCF10A and MCF10A-NeuT cells were incubated on micropatterned PA gels overnight. Single cells of each type were subjected to six sequential pushing forces (three DEP force magnitudes, two pushes per force magnitude) for 15 seconds each. Representative data for one MCF10A and MCF10A-NeuT cell. (b) Cell centroid displacement was quantified at each predicted DEP force. Data are mean ± standard deviation (n = 3 cells per condition, 2 deformations per cell at each force level). #$p < 0.05$, *$p < 0.01$, comparing cell types at each force level, unless brackets indicate otherwise (Tukey's test). (c) A second set of cells were indented by AFM using a silicon nitride cantilever

with 1 µm spherical tip to measure cell elastic modulus. Cell modulus was estimated by fitting the first 200 nm of the indentation curve to the Hertz model (* $p < 0.01$, $n = 7$ cells per cell type).

2.4. Discussion

2.4.1. Advantages and applications

These data demonstrate for the first time how an inverted DEP device can measure the stiffness of a material placed underneath the device, in our case a single attached cell. The inverted device configuration is an innovative feature that significantly increases device capabilities. First, it enables analysis of attached cells while not necessitating that the cells be attached to the device surface. Thus, within a single experiment the same DEP device can analyze multiple cells in series simply by changing the device position using the micromanipulator arm. In addition, the DEP device can analyze cells attached to different substrates; the user can easily vary substrate parameters, such as stiffness or ECM coating, using PA gels. The DEP device could even be lowered over a cell attached to a tissue, for example an extravasating monocyte, to measure its stiffness. By inverting the DEP device, we can take advantage of the forces induced beneath inverted DEP electrodes and thus create even greater functionality and flexibility of lab-on-a-chip microdevices.

Beyond pushing single attached cells to analyze relative cell stiffness, an inverted quadrupole DEP device could be used to trap and pattern cells or other particles in suspension. Recently dielectophoretic tweezers or single electrodes attached to micromanipulators have been used to capture and release cells in suspension [285, 286]. This inverted DEP device could be used in a similar matter to trap, move, and release cells at desired locations through device movement using a micromanipulator. Furthermore, by varying the voltages applied to opposing electrodes, a suspended, trapped cell could be shifted out of the device center (e.g., towards the lower voltage electrode) to increase device resolution. As has been suggested for DEP tweezers, this inverted quadrupole DEP device could enhance the establishment of stably transfected cell lines through quickly and selectively isolating individual fluorescent protein expressing cells [287]. In addition, such cell manipulation capability could be useful in sorting cells into microwell arrays, ensuring single cell occupancy and enabling single cell assays [288].

2.4.2. Limitations and potential improvements

Despite the inverted device advantages, the current configuration has limited through-put. The inverted DEP device can only measure one cell at a time due to the limiting step of detecting and quantifying cell deformation by microscopy and image analysis, respectively. A non-optical detection system would enable a microarray of inverted quadrupole electrodes. Recently, impedance sensors have been integrated into DEP cell trapping device to replace optical determination of trapping efficiency [289]. Ideally, single attached cell centroid displacement could be quantified through a similar completely electrical detection system. Thus an array of inverted DEP electrodes with a non-optical detection system has potential to increase the throughput of attached cell stiffness measurements.

3. Effect of substrate and arterial stiffness on endothelial adherens junctions in response to inflammatory permeability agonists

3.1. Introduction

A key function of the endothelium is the ability to act as an effective barrier between the blood and the blood vessel wall. Loss of endothelial barrier function has been implicated in atherosclerosis, cancer metastasis, and pulmonary disease [290, 291]. In atherosclerosis, endothelial permeability contributes to atherosclerotic plaque development by allowing lipoprotein diffusion and immune cell extravasation into the sub-endothelium, both of which contribute to plaque growth [24, 26, 292]. Thus better understanding of the mechanisms underlying endothelial barrier loss has potential to prevent the initiation and halt the progression of atherosclerosis.

The roles of both inflammation and arterial stiffening in atherosclerosis have been studied separately, but their compounded effects on endothelial barrier function have not been extensively investigated. Atherosclerosis is well-accepted as an inflammatory disease [293]. Tumor necrosis factor alpha (TNF-α) is one of many inflammatory cytokines known to increase endothelial permeability *in vitro* and *in vivo* [185, 294]. In middle-aged men, TNF-α blood levels correlated with intima-media thickness (an indicator of atherosclerosis), and atherosclerosis was more prevalent in elderly individuals with elevated plasma TNF-α levels [295, 296]. In addition, individuals with rheumatoid arthritis exhibited decreased intima-media thickness following one year of anti-TNF-α therapy [297].

Arterial stiffening has long been viewed as a consequence of pathological vascular remodeling; however, recent studies revealed that early arterial stiffening is also a predictor of future hypertension and atherosclerosis [298, 299]. Based on data from the

Framingham Heart Study, a large ongoing longitudinal cardiovascular study that began in 1948, increased pulse wave velocity (PWV, a non-invasive clinical measurement of arterial stiffness) was found to be an independent indicator of future cardiovascular events [7]. In another study on the general population, aortic PWV was found to be a significant predictor of cardiovascular mortality and development of coronary heart disease, which is characterized by atherosclerotic plaque development in the coronary artery [9, 300, 301]. These clinical results suggest arterial stiffening may contribute to endothelial barrier loss in atherosclerosis pathogenesis.

Both TNF-α and sub-endothelial stiffening induce increased actinomyosin cell contractility *in vitro,* leading to increased monolayer permeability [134, 184]. TNF-α induces cell contractility via Rho/ROCK, which increases permeability in some endothelial cell sub-types [184, 188, 302-304]. Substrate stiffness induces cell contractility via Rho/ROCK, which increases untreated endothelial monolayer permeability [134, 146]. While both TNF-α and substrate stiffness increase permeability via Rho/ROCK, the combined effect is poorly understood. There have been published reports that thrombin-induced endothelial contractility signaling and cell-cell junction loss increases with substrate stiffness [146, 147]. Thus, thrombin was used as a positive control in this study.

Based on published *in vitro* data suggesting that both substrate stiffness and inflammation increase cell contractility, **we hypothesized that increased sub-endothelial stiffness enhances TNF-α and thrombin-induced cell-cell junction tension and monolayer permeability.** This hypothesis was investigated using both *in vitro* and *ex vivo* systems. *In vitro* we explored the effect of substrate stiffness on intracellular tension induced by TNF-α and thrombin by examining endothelial monolayers on PA gel substrates (6-50 kPa) through immunofluorscent labeling, Western blot, and an *in vitro* monolayer permeability assay. *Ex vivo*, sub-endothelial stiffness of aortae from wild type and elastin haploinsufficient (ELN+/-) mice was measured by atomic force microscopy. *En face* confocal microscopy was also used to characterize the vessel endothelium [178]. In this chapter we show that vinculin recruitment to cell-cell junctions in response to TNF-α and thrombin *in vitro* is greater on stiffer substrates, suggesting translation of tension from cell-matrix adhesions to cell-cell junctions.

3.2. Methods

3.2.1. Polyacrylamide (PA) gel sample preparation

Polyacrylamide gels with elastic moduli of 6, 14, 29, or 50 kPa were prepared following well-established protocols [56]. Briefly, a bottom coverslip was made hydrophilic by consecutive incubations with 0.1 M NaOH, 3-aminopropyltrimethoxysiliane, and 0.5% glutaraldehyde. A top coverslip was made hydrophobic by applying Surfasil Siliconizing Fluid (1,7-dichloro-octamethyltetrasiloxane). A solution containing varying amounts of acrylamide and bis-acrylamide was prepared based on the desired gel stiffness (Table 3.1). Ammonium persulfate and tetramethylethylenediamine were added to the acrylamide/bis-acrylamide solution to achieve final concentrations of 0.1% w/v and 0.3% v/v, respectively, initiating gel polymerization. A drop of polymerizing gel solution was added to the bottom coverslip, and the top coverslip was quickly inverted onto the polymerizing gel to create a flat surface. After gel formation, the top coverslip was removed. To make the surface adhesive to cells, the gel was UV-activated using sulfo-SANPAH in DMSO and 50 mM

HEPES buffer, then incubated with 100 μg/mL type I collagen at 37°C for at least 3 hours at room temperature or at 4°C overnight. The collagen-coated gel was rinsed well in sterile PBS and UV-sterilized prior to cell seeding.

Table 3.1. Composition of acrylamide and bis-acrylamide in polyacrylamide gel preparations

PA gel elastic modulus	% acrylamide	% bisacrylamide
6 kPa	7.5%	0.05%
14 kPa	10%	0.1%
29 kPa	10%	0.3%
50 kPa	10%	0.6%

The top and bottom coverslip size and the gel solution volume varied depending on the type of sample being prepared. For immunofluorescent labeling, both the top and bottom coverslips were 12 mm diameter circular coverslips, and 50 μL gel solution was used. For Western blot experiments, the top and bottom coverslips were 22x22 mm square coverslips, and 200 μL gel solution was used. For the *in vitro* permeability assay, the bottom coverslip was a 22x22 mm square coverslip and the top coverslip was a 12 mm diameter circular coverslip; 5 μL gel solution was used to produce a very thin gel. In addition, 10 μM fluorescently labeled 40 kDa dextran (FITC-dextran) was added to the gel solution for the permeability assay samples to fluorescently detect the upper gel boundary.

PAECs were seeded and allowed to attach and proliferate over two to three days to achieve a cell monolayer. The cells were then incubated overnight in medium containing 1% FBS. For Western blot, cells were seeded in 5% FBS DMEM without phenol red and serum-starved in 1% FBS DMEM without phenol red. The following day, cells were left untreated or treated with 10 ng/mL TNF-α for varying durations.

3.2.2. Immunofluorescence

Cell samples were rinsed once with ice-cold PBS and fixed using ice-cold 4% paraformaldehyde (Sigma Aldrich), permeabilized using 0.2% TritonX-100 (EMD Millipore) in PBS for 15 minutes at room temperature and rinsed once using PBS. Samples were blocked with 1% BSA, 0.3% TritonX-100 in PBS for 1 hour at room temperature and then rinsed twice with PBS. Cells were labeled with the primary antibody (1:200 in 1% BSA) overnight at 4°C, then rinsed twice with PBS. Actin and nuclei were labeled using rhodamine phalloidin (16.5 nM, Invitrogen) and bisbenzimide (0.2 μg/mL, Invitrogen), respectively. Thrombin, which elicits increased cell contractility and drastic cell-cell junction loss, was used as a positive control in these studies (10 U/mL, 30 minutes) [305, 306]. Figure 3.1 depicts the junction loss following thrombin treatment of cells on glass; β-catenin labeling shows wide junctions with honeycomb-like morphology in untreated cells (Figure 3.1a, selection magnified in Figure 3.1b). This particular junction morphology indicates intact junctions and is referred to as “reticular junctions” [186]. Disrupted punctate junctions are observed in thrombin-treated cells, along with noticeable holes in the endothelial monolayer (Figure 3.1c, selection magnified in Figure 3.1d).

For most figures, images were taken using an Olympus Fluoview 1000 confocal microscope. Unless otherwise noted, images are compressed z-stack images with 0.25 μm in between focal planes. For Figure 3.1, figures were taken with an inverted epifluorescent microscope at 60X magnification (oil immersion).

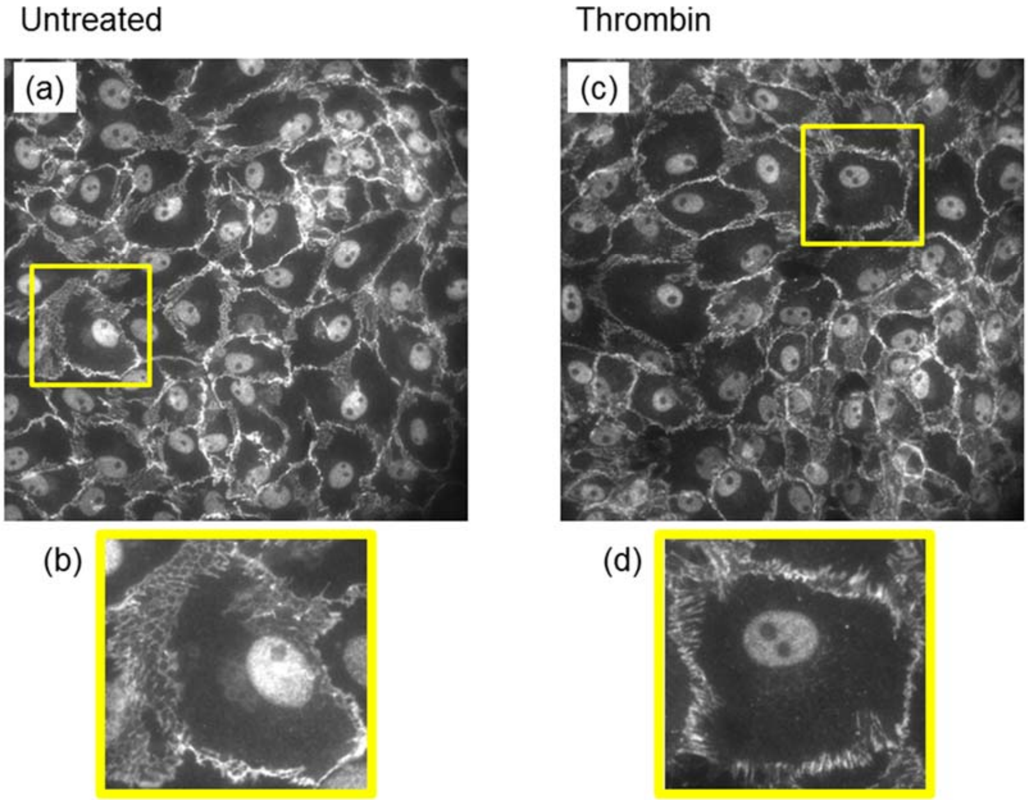

Figure 3.1. Thrombin disrupted reticular adherens junctions among adjacent endothelial cells. Cell monolayers on glass coverslips were untreated (a) or treated with 10 U/mL thrombin for 30 minutes (c) prior to fixation and immunofluorescent labeling of β-catenin. Selected cells from A and C are magnified in B and D, respectively, to emphasize the difference in morphology between "honeycomb-like" intact reticular junctions (b) and thrombin-disrupted junctions (d).

3.2.3. Matlab image analysis

Images were processed and analyzed using custom Matlab code to quantify levels of phosphorylated MLC. Confocal z-stacks were compressed to produce a single image. Background intensity was determined by taking the average of a 50 by 50 pixel region; this intensity was multiplied by a user-determine modifier (0.6), which was held constant for all images within an experiment to decrease the background subtracted from the image. These steps were repeated to complete the background subtraction process. A threshold for image binarization was calculated using Otsu's method; the calculated threshold was multiplied by a modifier, which was held constant for all images (0.7). To remove noise, any components smaller than 30 pixels were removed from the binarized image. The amount of phosphorylated MLC was quantified by finding the sum of all remaining pixels in the image above the binarization threshold.

3.2.4. *In vitro* permeability assay

Tetramethylrhodamine-labeled fluorescent dextran (TMR-dextran) diffusion through a confluent endothelial monolayer into the gel substrate was used to quantify endothelial cell permeability. Confluent endothelial monolayers were serum-starved in 1% FBS DMEM overnight, then administered treatment—either 10 ng/mL TNF-α for 3 hours or 10 U/mL thrombin for 30 minutes. Following treatment, 10 μM 10 kDa TMR-dextran in CO_2-independent medium was added on top of the sample for 5 minutes to allow for dextran diffusion through the endothelial cell monolayer and into the gel substrate. Approximately 60-80 z-stack images were acquired for each sample at 20X magnification using an Olympus Fluoview 1000 confocal microscope, with 1 μm steps between focal planes.

Z-stack images were quantified in Image J. Each z-stack was cropped to a size of 199.96 x 199.96 square pixel area to minimize any gel surface unevenness. Using the 'reslice' function in Image J, the z-stacks were converted to produce an image of the z-stack viewed from the side (converting from an xy view to an xz view).

3.2.5. Western blot

PAEC were cultured on 22x22 mm square collagen-coated PA gels of varying stiffness for three days in 5% FBS phenol red free medium and serum-starved overnight in 1% FBS phenol red free medium. Cells were rinsed once with ice-cold PBS. Cells on PA gel samples were removed from PBS, and the side of the gel was gently dabbed on a Kimwipe to remove excess PBS. Gels were inverted into a well of a clean 6-well plate containing 50 µL ice-cold lysis buffer (20 mM Tris, 150 mM NaCl, 1% Triton X-100, 0.15 SDS, 2 mM EDTA, 2 mM $NaVO_4$, 2 mM PMSF, 50 mM NaF, 10% glycerol, complete protease inhibitor, pH 7.4). Samples were incubated for 10 minutes at 4°C to allow for cell lysis. Gel samples were gently scraped to remove any remaining cell lysate, and lysates were collected into pre-chilled Eppendorf tubes. The lysates from at least two 22x22 mm gels were pooled to collect enough protein content for each sample. Cell lysates were normalized for protein content using the bicinchoninic acid (BCA) assay and reduced at 70°C for 10 minutes prior to separation by SDS-PAGE on a 4-12% Bis-Tris gel and transfer to a nitrocellulose membrane. For detection of vinculin, VE-cadherin, or GAPDH, membranes were blocked for 1 hour at room temperature with 10% bovine serum albumin (BSA) in PBS-T (0.05% Tween 20 in PBS), and probed overnight at 4°C with the primary antibody (1:1000 in 5% BSA in PBS-T). Following rinsing with PBS-T, membranes were probed with species-specific secondary horseradish peroxidase-conjugated antibody (1:2000 dilution in 5% BSA) for 2 hours at room temperature and detected with an enhanced chemiluminescence kit. Membranes were imaged with a Fluorochem digital imager. AlphaEase FC software was used for quantification of band intensity.

3.2.6. *En face* imaging of mouse aorta

The entire aorta was dissected and transferred to ice-cold HEPES buffer (140 mM NaCl, 5 mM KCl, 1 mM $CaCl_2$, 1.2 mM $MgSO_4$, 1.2 mM Na_2HPO_4, 10 mM HEPES, 10 mM sodium acetate, 5 mM glucose, pH 7.4). Excess tissue was cleaned from the outside of the vessel, and the vessel was cut open longitudinally to expose the endothelium. Insect pins were used to pin the vessel flat onto a flat layer of cured polydimethylsiloxane (PDMS) in the bottom of a plastic dish. While pinned open, the tissue was fixed with ice-cold 4% paraformaldehyde on ice for 30 minutes. The vessel was then rinsed with PBS and simultaneously blocked and permeabilized with 1% BSA/0.3% Triton X-100 for 60 minutes at room temperature. The tissue was labeled with primary antibody in 1% BSA in PBS overnight at 4°C. After several rinses with PBS, the vessel was incubated with secondary antibody, rhodamine phalloidin, and/or Hoechst for 1 hour at room temperature, protected from light. The vessel was rinsed twice with PBS, mounted between two coverslips in 1:1 glycerol:PBS, and imaged using an Olympus Fluoview 1000 confocal microscope at 60X magnification. Images were taken every 0.5 μm, and z-stack images were compressed to visualize the endothelium.

3.2.7. Atomic force microscopy

Relative changes in cell stiffness were determined by atomic force microscopy (AFM, Veeco Bioscope). PAEC were allowed to grow to confluence over three days in 5% FBS DMEM, then serum-starved overnight in 1% FBS DMEM. Cells were left untreated or treated with 10 ng/mL porcine TNF-α for increasing times between 3 and 24 hours, then immersed in CO_2-independent medium. Three AFM indentations were made per cell using a 0.06 N/m cantilever with a 1 μm spherical tip. Force-indentation curves were fit using the Hertz model down to 200 nm indentation, and the stiffnesses measured at each of three locations were averaged to calculate cell stiffness. Ten cells were analyzed per sample. Fold change in cell stiffness was calculated as the average cell stiffness for TNF-α-treated samples divided by the average cell stiffness for untreated samples for each PA gel substrate stiffness.

AFM was similarly used to quantify aortic stiffness in wild type and ELN+/- mouse aortae. The aorta was dissected, cleaned, and cut open longitudinally to expose the endothelium as described for *en face* imaging. Each aorta was cut into four segments—two thoracic segments and two abdominal segments—producing four samples per aorta. Samples were carefully mounted, endothelium facing up, on a coverslip using Loctite 401 medical grade adhesive and submersed in PBS. The endothelium was removed by gently scraping with a cotton-tip applicator, based on a published protocol [307]. Sub-endothelial stiffness was determined by AFM using pre-calibrated cantilevers with spring constants between 0.10 and 0.17 N/m with 10 μm spherical tips. Between three and nine indentations were made at different locations along each sample. The force-indentation curve for each indentation was fit to the Hertz model down to 200 nm indentation using custom Matlab code to produce a stiffness value. Sub-endothelial stiffness was calculated as the average of the individual stiffness values of each sample.

3.2.8. Statistical analysis

All statistical analyses were conducted using Matlab's statistical toolbox. Graphs represent mean value ± standard deviation. Multiple groups were compared using either two-way or n-way ANOVA, and two groups were compared by Student's t-test. For Western blot assessment of VE-cadherin and vinculin protein levels, conditions were tested in duplicate. For other *in vitro* experiments, conditions were tested in triplicate. All experiments were run at least two times, excluding data supporting AFM method development (Figures 3.2 and 3.3).

3.3. Results

3.3.1. *Ex vivo* analysis of sub-endothelial stiffness in WT and ELN+/- mice

Macroscale arterial stiffness, measured by pulse wave velocity, is increased in mice genetically engineered to produce less elastin (elastin haploinsufficient, ELN+/) [308]. However, the sub-endothelial stiffness has not been characterized in this mouse model. We removed the endothelium from longitudinally dissected aortic sections (Figure 3.2) prior to measuring sub-endothelium stiffness by atomic force microscopy (AFM). In the unscraped segment, nuclei aligned perpendicular to the blood flow direction (from smooth muscle cells) were observed wrapping around the vessel circumferentially, as well as nuclei aligned parallel to the blood flow direction (from the endothelium) (Figure 3.2a). VE-cadherin labeling of the unscraped vessel reveals VE-cadherin in the adherens junctions of the intact endothelium (Figure 3.2b). In the scraped segment, the endothelial nuclei (parallel to the blood flow direction) were removed and the smooth muscle cell nuclei (perpendicular to the blood flow direction) remained

(Figure 3.2c). VE-cadherin labeling of the scraped vessel showed some remaining debris but no endothelial adherens junction (Figure 3.2d). These results indicated that the scraping method removed the endothelium from the aortic section and exposed the sub-endothelium for AFM measurements.

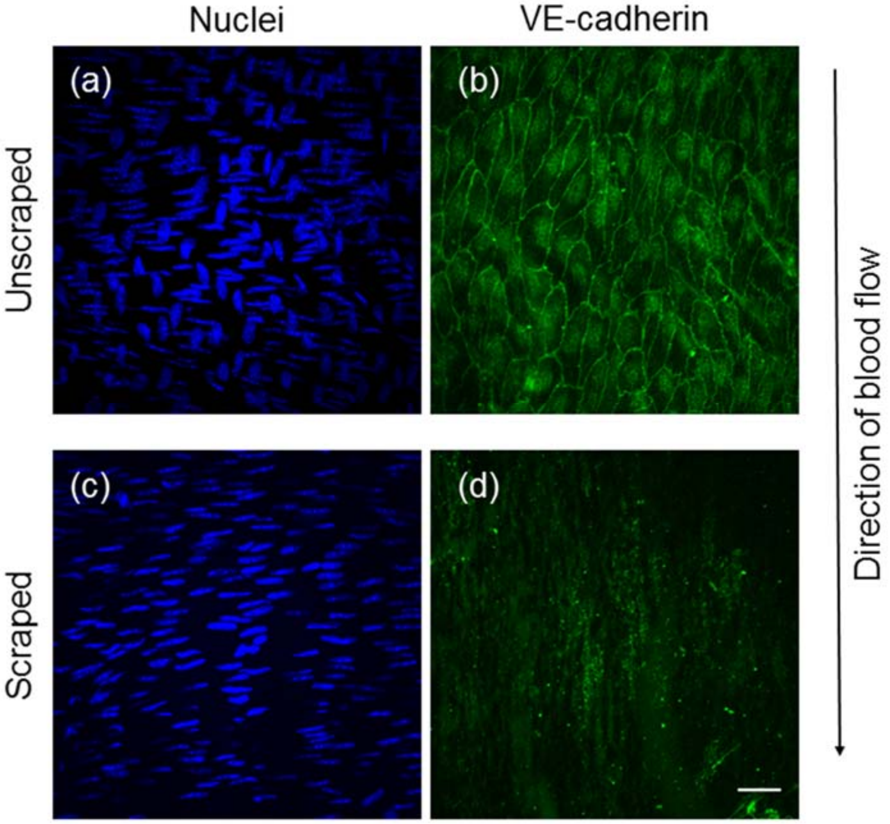

Figure 3.2. Gentle scraping removed the mouse aortic endothelium while leaving the underlying smooth muscle cell layers intact (a) An unscraped vessel segment with Hoechst labeling of the nuclei in both the endothelium and the smooth muscle cell layer underneath (b) VE-cadherin labeling of endothelial adherens junctions in an unscraped vessel (c) Smooth muscle cell nuclei remained after endothelial scraping (d) VE-cadherin labeling of the scraped vessel segment. Scale bar is 25 μm.

Aortic sections were then co-labeled for the adherens junction protein β-catenin, actin, nuclei, and the basement membrane protein collagen IV to confirm that the endothelial scraping method did not also remove the basement membrane (Figure 3.3).

In the unscraped aortic section (Figure 3.3a and b), all four components were visible, indicating an intact endothelium, basement membrane, and smooth muscle cell layer. In the scraped aortic section (Figure 3.3c and d), endothelial β-catenin was almost entirely removed. Some β-catenin debris was visible in the crevices between tissue folds (Figure 3.3c), which would not have been accessible to the AFM cantilever tip during testing. Collagen IV in the scraped vessel was clearly seen as a distinct layer on top of the actin-rich smooth muscle cell layer (in particular by viewing the confocal image z-stack from the side) and looked similar to collagen IV in the unscraped vessel. These results indicated that the scraping method did not remove collagen IV, a major component of the sub-endothelial basement membrane, prior to AFM measurements.

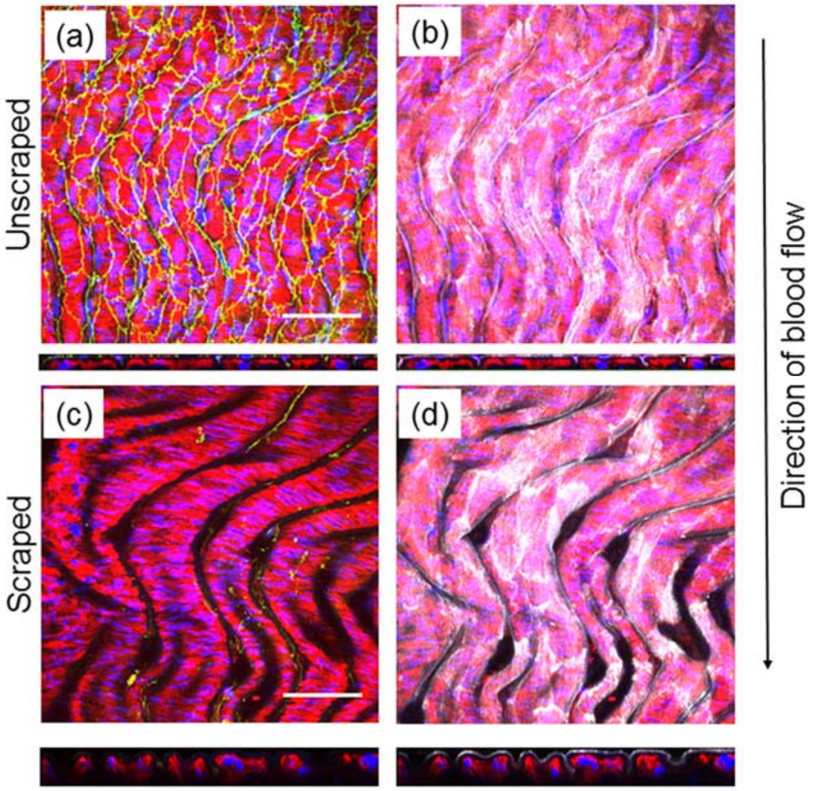

Figure 3.3. Endothelial scraping maintained sub-endothelial basement membrane proteins. For each condition the vessel segment is shown from the top and the side of a compressed confocal z-stack (a) β-catenin (green), actin (red) and nuclei (blue) in an unscraped aortic segment. (b)

Collagen IV (white) in the sub-endothelial basement membrane in the unscraped aortic segment above actin (red) in the smooth muscle cell layer (c) β-catenin, actin and nuclei in a scraped aortic segment. (d) Collagen IV in the scraped aortic segment looked similar to the unscraped segment, suggesting an undisturbed basement membrane. Scale bar is 50 μm.

Next, aortic sub-endothelium samples were indented by AFM to detect any differences in sub-endothelial stiffness between the wild type and ELN+/- genotypes. As shown in Figure 3.4a, each aorta was cut open longitudinally, mounted and scraped by the same method used to prepare the aortic segments in Figures 3.2 and 3.3. The ELN+/- thoracic aortic sub-endothelium was 1.79-fold stiffer as compared to wild type (Figure 3.4b). In addition, the abdominal aortic sub-endothelium from ELN+/- mice was 1.76-fold stiffer as compared to wild type.

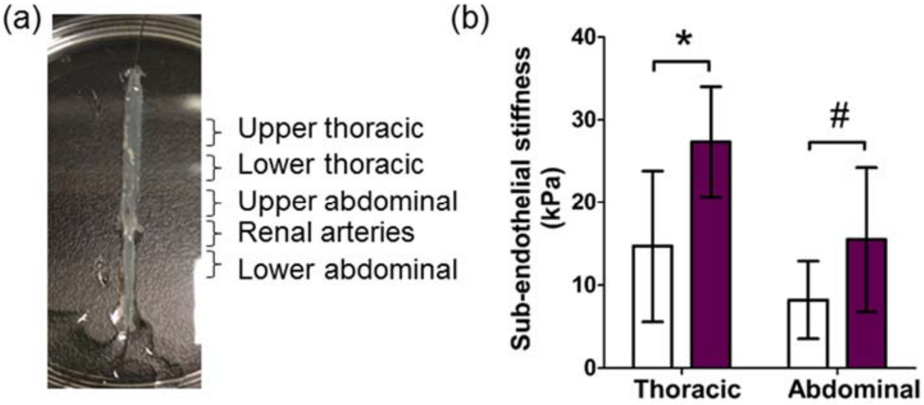

Figure 3.4. Sub-endothelial stiffness increased in the thoracic and abdominal aorta of ELN+/- mice. Vessels were cut open longitudinally and pinned to a silicone-lined dish (A). Each aorta was cut into four segments (upper and lower thoracic and abdominal aorta). The renal arteries were not analyzed, but used as a reference to determine the relative location of the segments along the vessel (B) The endothelium of the vessel segments was removed by gentle scraping and sub-endothelial stiffness was determined by AFM indentation using a 10 μm spherical tip on a pre-calibrated cantilever. The aortae from five mice per genotype were analyzed and compared by Student's t-test (*p<0.05, *p<0.01). Data are shown as average stiffness ± standard deviation.

3.3.2. Immunofluorescent characterization of wild type and ELN+/- aortic endothelium

To determine if decreased elastin content in ELN+/- mice affected endothelial cell-cell junction composition, wild type and ELN+/- aortic sections were fixed, labeled and imaged *en face* by confocal microscopy (Figure 3.5). Immunofluorescent labeling for VE-cadherin and vinculin showed vinculin co-localization with VE-cadherin at adherens junctions in the thoracic aortic section of both wild type and ELN+/- mice (Figure 3.5a). Vinculin localization differences between the two genotypes were observed in the abdominal aorta. In the ELN+/- mice, vinculin also co-localized with VE-cadherin at adherens junction in the abdominal aortic section. In contrast, in the abdominal aorta of WT mice (the section with the softest sub-endothelium by AFM) vinculin localized mainly to punctate structures at the endothelial basal surface thought to be focal adhesions. Following image quantification (Figure 3.5b), VE-cadherin localized with vinculin in thoracic aortic sections did not change between WT and ELN+/- mice; however, percent co-localization was nearly 20% lower in abdominal aortic sections from WT mice compared to ELN+/- mice (38% vs. 46% co-localization, respectively).

As shown in Figure 3.5c, aortic segments were also labeled for focal adhesion kinase (FAK), a signaling molecule known to associate with both focal adhesions and adherens junctions. In WT thoracic and abdominal sections, pFAK was not detected at the cell periphery; however, in ELN+/- thoracic and abdominal sections, pFAK was localized near adherens junctions. Image quantification (Figure 3.5d) showed a significant two-fold increase in vinculin co-localized with pFAK in the combined ELN+/- thoracic and abdominal aortic sections compared to WT aortic sections. In summary, both vinculin and pFAK labeling revealed differences in endothelial cell-cell junction composition between WT and ELN+/- aortic sections. Since vinculin localization to cell-cell junctions is dependent on increased tension on the junction protein α-catenin, we hypothesized that endothelial cells in areas of increased sub-endothelial stiffness experienced higher tension at their cell-cell junctions.

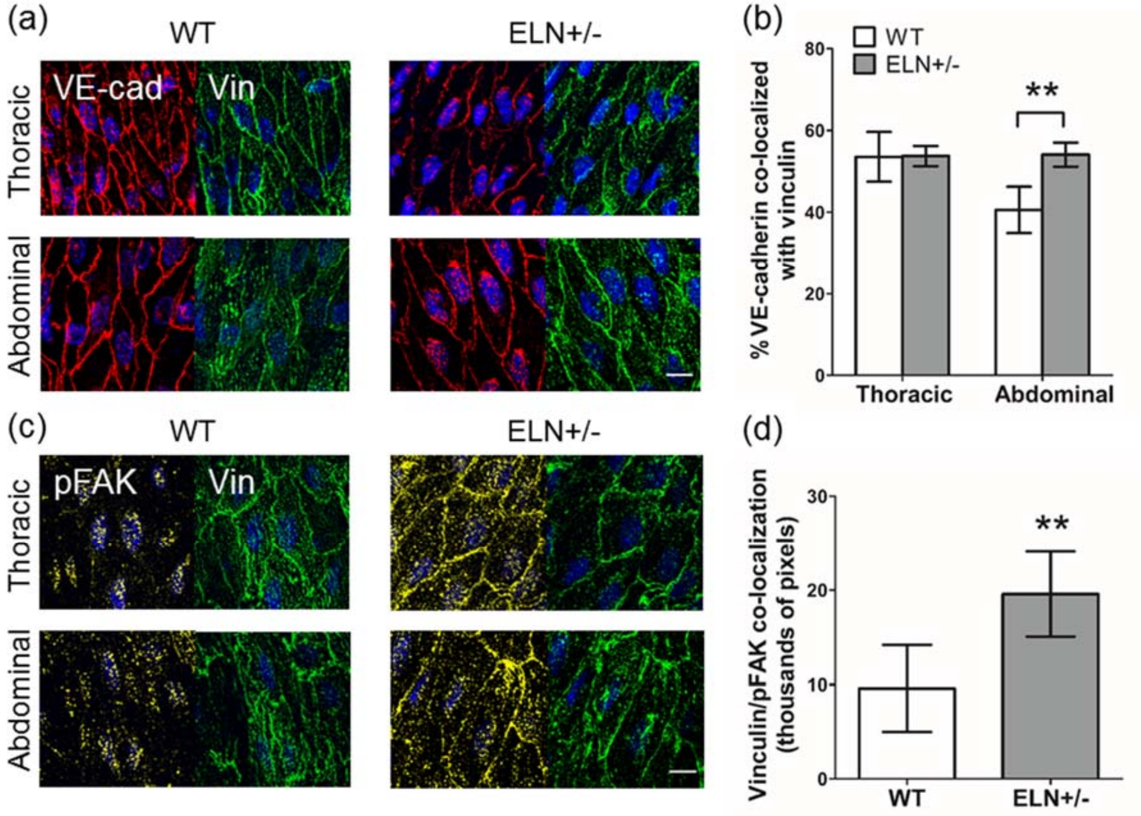

Figure 3.5. Vinculin and pFAK showed more co-localization with cell-cell junctions in the aortic endothelium of ELN+/- mice. (a) Immunofluorescent labeling of VE-cadherin (red), vinculin (green), and nuclei (blue) in thoracic and abdominal sections of mouse aortae imaged en face by confocal microscopy. Z-stacks of confocal images were compressed to show labeling through the entire endothelium. (b) Images were processed and quantified using custom Matlab code to determine the percent VE-cadherin co-localized with vinculin. (c) Immunofluorescent labeling of pFAK (yellow), vinculin (green), and nuclei (blue). (d) Image quantification of percent vinculin co-localized with pFAK. Scale bar is 25 μm. Data are shown as average ± standard deviation.

3.3.3. Substrate-dependent changes in adherens junction composition, actin cytoskeleton, cell contractility, and focal adhesion activation in response to TNF-α and thrombin *in vitro*

In vitro experiments were conducted to further investigate the role of sub-endothelial stiffness on cell contractility and cell-cell junction structure. Porcine aortic endothelial cells were seeded on collagen-coated PA gels with elastic moduli between 6 and 50 kPa (to simulate increasing vessel stiffness) and treated with TNF-α or thrombin to induce cell contractility. Immunofluorescent labeling of endothelial monolayers attached to PA gels was used to observe cell-cell junction morphological changes in response to stiffness, TNF-α, and thrombin.

Figure 3.6 shows co-labeling of VE-cadherin and vinculin in the apical plane of representative cells within untreated, TNF-α -treated, or thrombin-treated confluent endothelial monolayers. In untreated cells, vinculin was minimally detected at adherens junctions in cells on the 29 kPa gel and distinctly absent from cell-cell junctions on the 6 kPa gel. With TNF-α treatment, no changes in junction morphology or vinculin localization were observed in cells on the 6 and 14 kPa gels. On the 29 kPa gels, apical adherens junctions were linear with small disruptions; in addition, vinculin co-localized with VE-cadherin. In thrombin-treated cells, both VE-cadherin labeled junction linearization and vinculin with VE-cadherin co-localization increased with substrate stiffness. Since vinculin localization to cell-cell junctions occurs following tension-dependent conformational changes of α-catenin, these results suggest that tension at cell-cell junctions following exposure to TNF-α or thrombin is higher on stiffer substrates.

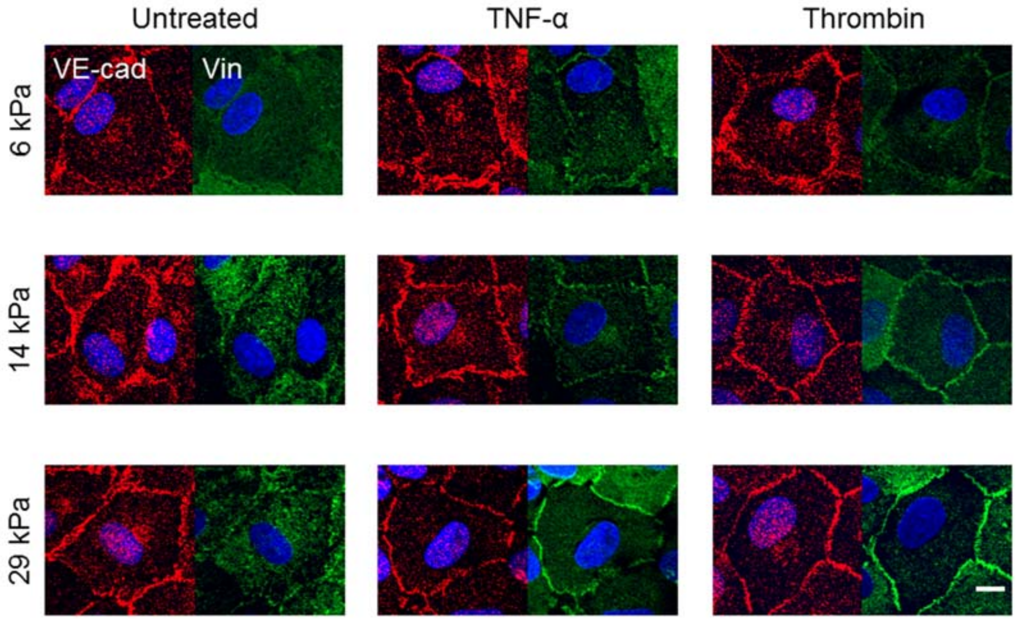

Figure 3.6. Stiff substrates enhanced vinculin co-localization with VE-cadherin at apical adherens junctions in response to TNF-α and thrombin. Cell monolayers on 6, 14, and 29 kPa substrates were treated with 10 ng/mL TNF-α for 3 hours or 10 U/mL thrombin for 30 minutes, fixed, and labeled for VE-cadherin (red), vinculin (green), and nuclei (blue). Confocal z-stacks were acquired at 60X magnification, and the uppermost plane was selected as the apical cell surface. Representative cells from within confluent monolayers are shown to highlight differences in vinculin localization. Scale bar is 10 μm.

Total vinculin content was examined by Western blot to determine if the changes cell-cell junction vinculin in cells on stiff substrates was due to increased translocation or vinculin protein production (Figure 3.7a). Total vinculin levels, normalized to GAPDH, were not significantly different among all conditions tested, suggesting vinculin translocation to junctions instead of increased vinculin production (Figure 3.7b). Interestingly, total VE-cadherin decreased with increased substrate stiffness (Figure 3.7c). There was no significant effect of TNF-α or thrombin treatment on total VE-cadherin levels.

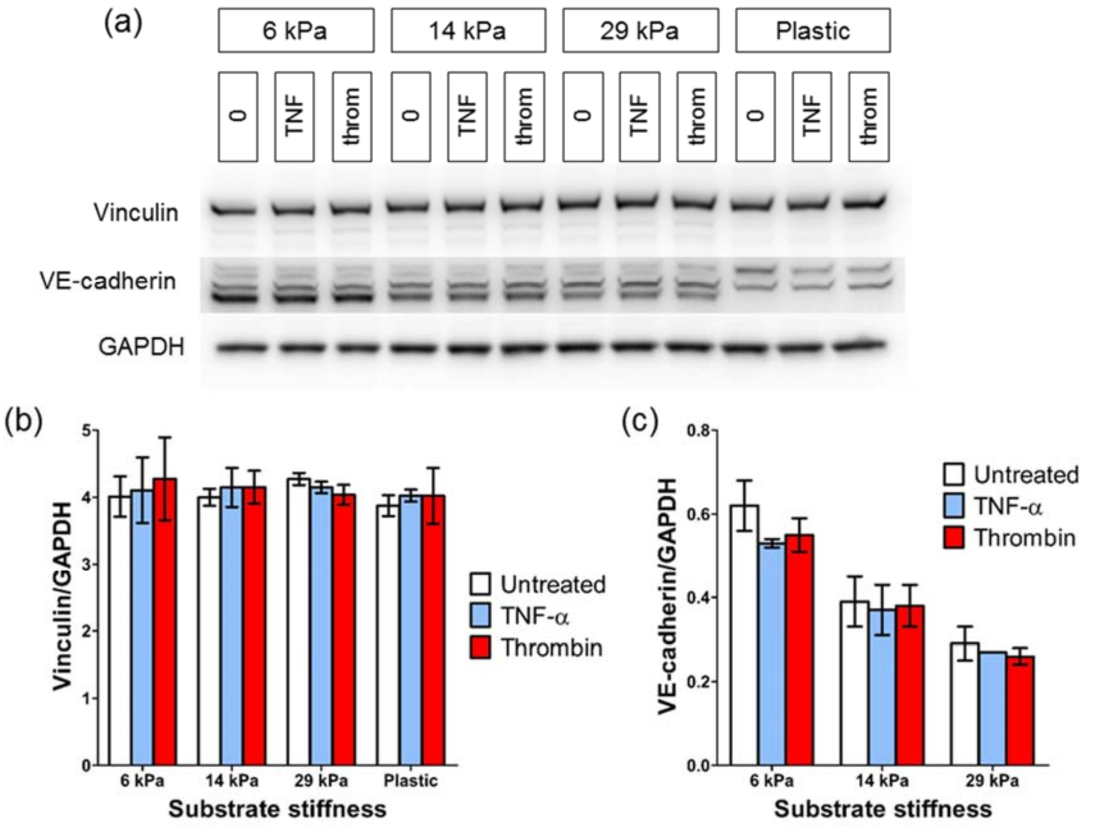

Figure 3.7. Total vinculin did not change with substrate stiffness, TNF-α, or thrombin treatment; total VE-cadherin decreased with substrate stiffness, but not TNF-α or thrombin treatment. (a) Total vinculin, VE-cadherin, and GAPDH protein levels in cells that were untreated, TNF-α – treated (10 ng/mL, 3 hours), or thrombin-treated (10 U/mL, 30 minutes) on 6, 14, and 29 kPa substrates or tissue culture plastic were analyzed by Western blot. Vinculin and VE-cadherin levels were normalized to GAPDH and analyzed by n-way ANOVA. There was no significant effect of stiffness or treatment in total normalized vinculin. For total normalized VE-cadherin, the effect of stiffness was significant ($p<0.001$) while the effect of treatment was insignificant. Data are shown as average ± standard deviation.

Next we examined cell-cell junction structure in endothelial monolayers on substrates of different stiffness following TNF-α or thrombin treatment, to determine if increased tension at the junctions corresponded with morphological changes. Confocal images of the junction protein β-catenin in cells on 6, 14, and 29 kPa substrates are shown in Figure 3.8. Untreated, TNF-α-treated and thrombin-treated confluent monolayers imaged at 60X magnification are shown in Figure 3.8a, with representative individual junctions magnified in Figure 3.8b. In untreated cells, junction size qualitatively diminished with increasing substrate stiffness. Thick junctions with "honeycomb-like" structure, as seen between untreated cells on 6 kPa gels, represent areas where adjacent cells overlap, called "reticular adherens junctions". With TNF-α treatment, cell-cell junction thinning was minimal on 6 kPa gels and increased with substrate stiffness. Junction thinning corresponded with the loss of the "honeycomb" morphology. With thrombin treatment, cell-cell junctions thinned to a greater extent when compared to TNF-α treatment. Junctions between cells on 6 kPa gels exposed to thrombin still maintained some junction thickness. On 29 kPa thrombin-treated samples, junctions lost the "reticular" morphology and more closely resemble focal adherens junctions, with diminished, punctate contact between adjacent cells [309]. The transition from thick "reticular adherens junctions" to punctate "focal adherens junctions" occurs as cells separate from each other; thus, these results indicate that endothelial cell-cell junction loss following exposure to TNF-α or thrombin is enhanced by stiff substrates.

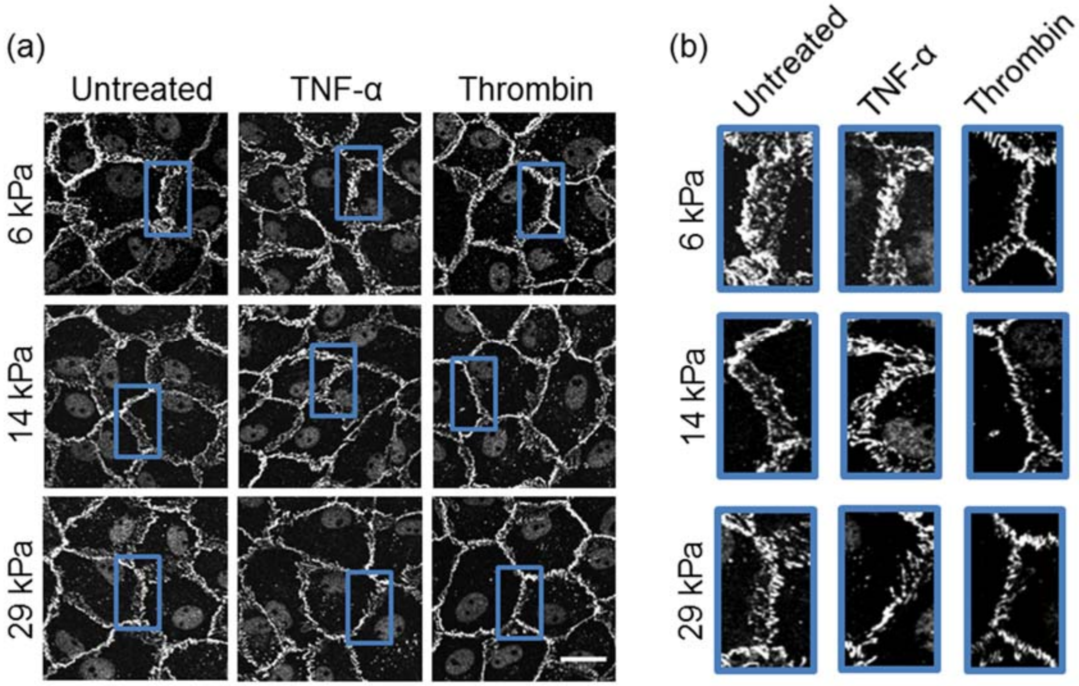

Figure 3.8. Substrate stiffening exacerbated reticular adherens junction thinning in response to TNF-α and thrombin. Cells on 6, 14, and 29 kPa polyacrylamide gels were untreated, treated with 10 ng/mL TNF-α for 3 hours, or treated with 10 U/mL thrombin for 30 minutes prior to fixation. (a) Images show β-catenin labeling in confluent monolayers. Areas highlighted by rectangular regions are magnified in (b) to highlight differences in junction morphology. Scale bar is 25 μm.

Next, we hypothesized that increased junction tension and cell-cell junction loss on stiff substrates depended on increased actinomyosin contractility. To see if substrate stiffness increased actin fiber formation in confluent endothelial monolayers in response to TNF-α or thrombin, endothelial cells on 6, 14, and 29 kPa PA gels were labeled for actin. Figure 3.9 shows compressed confocal z-stacks, which captured actin cytoskeletal morphology throughout the cell layer. In untreated cells, peripheral actin bundles were present in cells on all substrates but were particularly distinct in cells on 6 kPa gels. Following 3 hours of 10 ng/mL TNF-α treatment, peripheral actin was maintained in cells on 6 kPa gels but diminished in cells on 14 and 29 kPa gels. Following 30 minutes of 10 U/mL thrombin treatment, peripheral actin was diminished in cells on all substrates and actin stress fibers were increased in cells on 29 kPa gels. These results indicate that actin fiber stress formation was enhanced on stiff substrates.

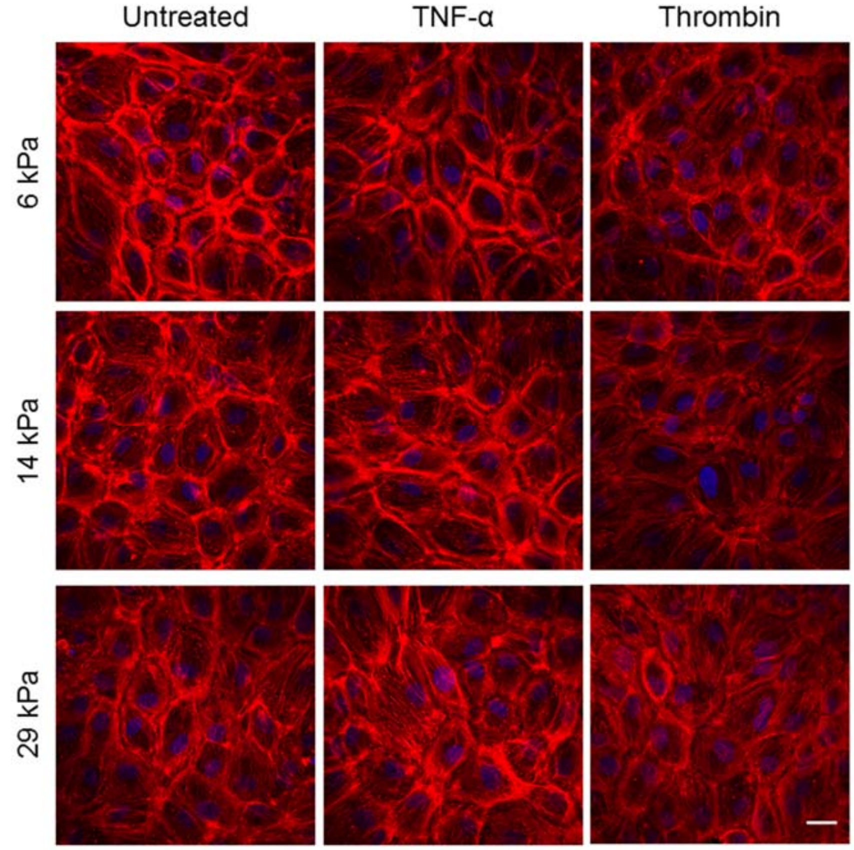

Figure 3.9. Actin stress fiber formation in response to TNF-α and thrombin was greater on stiff substrates as compared to soft substrates. Cells on 6, 14, and 29 kPa collagen-coated PA gels were untreated (left), treated with 10 ng/mL TNF-α for 3 hours (middle) or treated with 10 U/mL thrombin for 30 minutes (right) prior to fixation and labeling with rhodamine phalloidin (red, actin) and Hoechst (blue, nuclei). Images are compressed confocal z-stacks at 60X magnification. Scale bar is 25 µm.

To assess if increased actin stress fiber formation corresponded with increased endothelial monolayer contractility on stiff substrates, immunofluorescent labeling of phosphorylated myosin light chain (pMLC) was conducted following TNF-α or thrombin treatment (Figure 3.10a). pMLC localized to punctate peripheral structures at cell-cell junctions in untreated cells. Punctate pMLC labeling was lost with TNF-α and thrombin treatment; instead pMLC co-localized with actin fibers, and this effect increased with substrate stiffness. In Figure 3.10b, pMLC image quantification revealed an increase in total pMLC with both TNF-α and thrombin treatment ($p<0.0001$ by two-way ANOVA for both cases). Substrate stiffness showed significant interaction with both TNF-α ($p<0.05$) and thrombin ($p<0.01$). These results indicate that increasing substrate stiffness enhanced the increase in TNF-α and thrombin-induced total pMLC. Interestingly, differences in pMLC localization between TNF-α and thrombin were observed. In TNF-α -treated cells, pMLC mostly localized to stress fibers in the cell periphery on all substrates. In contrast, some pMLC localized to peripheral actin in thrombin-treated cells on the 6 kPa gels but was distinctly present along longitudinal stress fibers in cells on the 29 kPa gels.

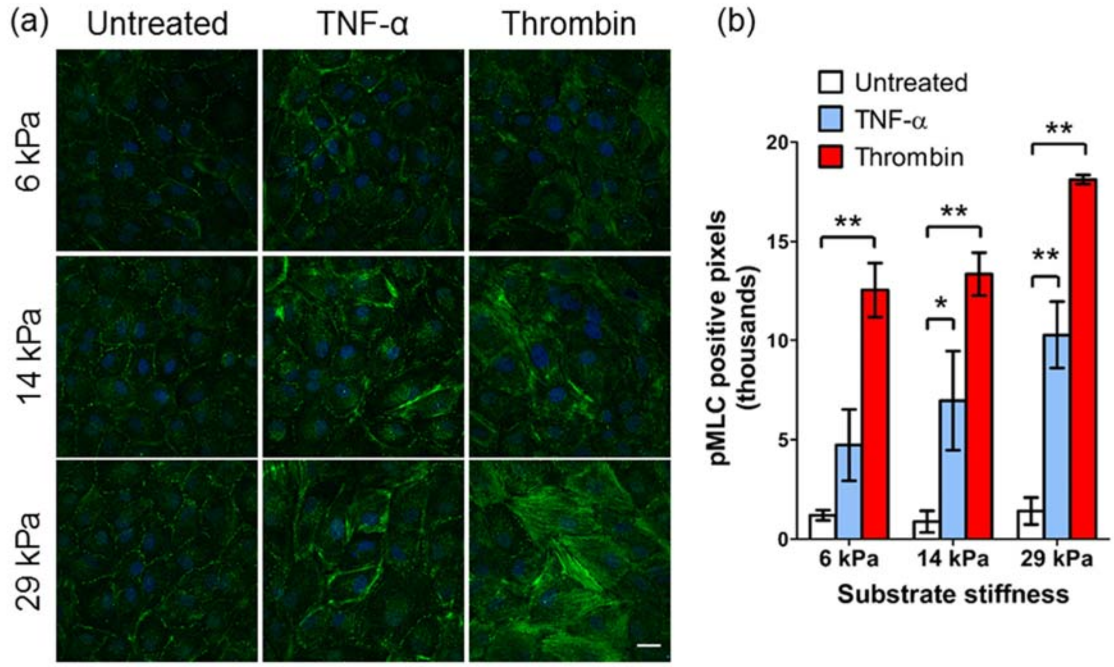

Figure 3.10. Total pMLC was greater on stiff substrates in response to TNF-α and thrombin. pMLC localized to peripheral actin with TNF-α treatment and longitudinal actin with thrombin treatment on the stiffer substrates. (a) Cells on gels of varying stiffness were treated with 10 ng/mL TNF- α for 3 hours or 10 U/mL thrombin for 30 minutes, fixed, and labeled for pMLC (green). Linear pMLC represents myosin localization along actin fibers. (b) Images were processed and quantified to assess total pMLC. By two-way ANOVA, TNF-α and thrombin significantly increased pMLC labeling ($p<0.01$). The interactions between substrate stiffness/TNF and substrate stiffness/thrombin were significant ($p<0.05$ and $p <0.01$, respectively). *$p<0.01$, **$p<0.001$ (Tukey-Kramer post-hoc test). Data are shown as average ± standard deviation.

Next, we investigated changes in activated focal adhesions, the structures responsible for substrate stiffness sensing, following substrate-dependent cell contractility due to TNF-α and thrombin exposure. Immunofluorescent pFAK labeling was used to visualize focal adhesion activation in cells on substrates of increasing stiffness (Figure 3.11). In untreated cells on all substrate stiffnesses, punctate pFAK labeling revealed generally small, evenly distributed focal adhesions. With TNF-α treatment (middle column), pFAK labeling did not change in cells on 6 and 14 kPa substrates. On 29 kPa substrates, some larger focal adhesions were observed around the cell peripheries. With thrombin treatment, pFAK labeling did not change in cells on the 6 kPa substrate. To a lesser extent on 14 kPa substrates and a greater extent on 29 kPa substrates, larger pFAK-containing focal adhesions were observed at cell peripheries. pFAK was mainly co-localized with vinculin in focal adhesions at the basal membrane; little pFAK was observed at cell-cell junctions under the conditions tested. These results implicate focal adhesions in substrate-dependent responses to TNF-α and thrombin.

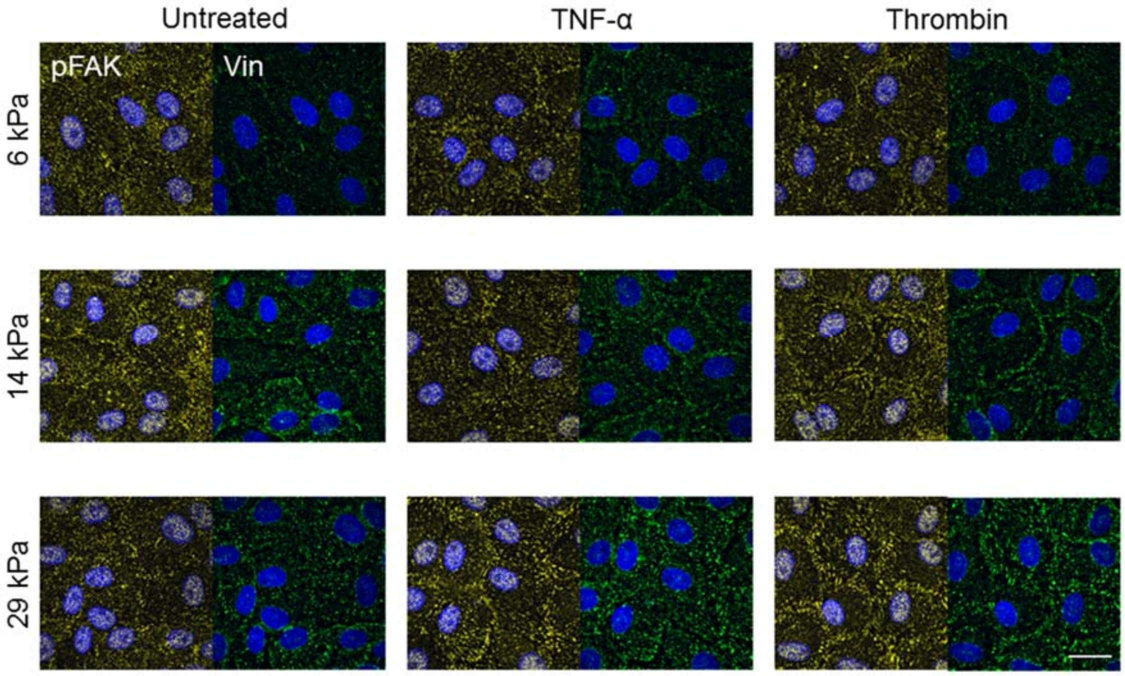

Figure 3.11. Larger, activated focal adhesions formed at the cell periphery in response to TNF-α and thrombin on stiffer substrates. Cells were treated with 10 ng/mL TNF-α for 3 hours or 10 U/mL thrombin for 30 minutes, fixed, and labeled for pFAK (yellow), vinculin (green) and nuclei (blue). Confocal z-stacks were acquired at 60X magnification with optical zoom of 2 and compressed. Scale bar is 25 µm.

3.3.4. Role of ROCK signaling in actin reorganization, vinculin translocation, and adherens junction morphology on substrates of difference stiffness in response to TNF-α and thrombin

The ROCK inhibitor Y-27632 was used to investigate the role of cell contractility in substrate-dependent vinculin recruitment to adherens junctions following TNF-α and thrombin treatment (Figure 3.12). While punctate pMLC was still present at the cell periphery after ROCK inhibition, pMLC localization to actin fibers after TNF-α and thrombin treatment was abolished by Y-27632. Actin fibers appeared disorganized with Y-27632 treatment alone; however, peripheral actin bands still formed in cells on 6 and 14 kPa with Y-27632 and TNF-α treatment. This observation suggests that peripheral actin fiber formation is controlled by a ROCK-independent pathway or upstream of ROCK signaling. Some actin stress fibers were still observed in the center of cells on 29 kPa gels following Y-27632 and thrombin treatment.

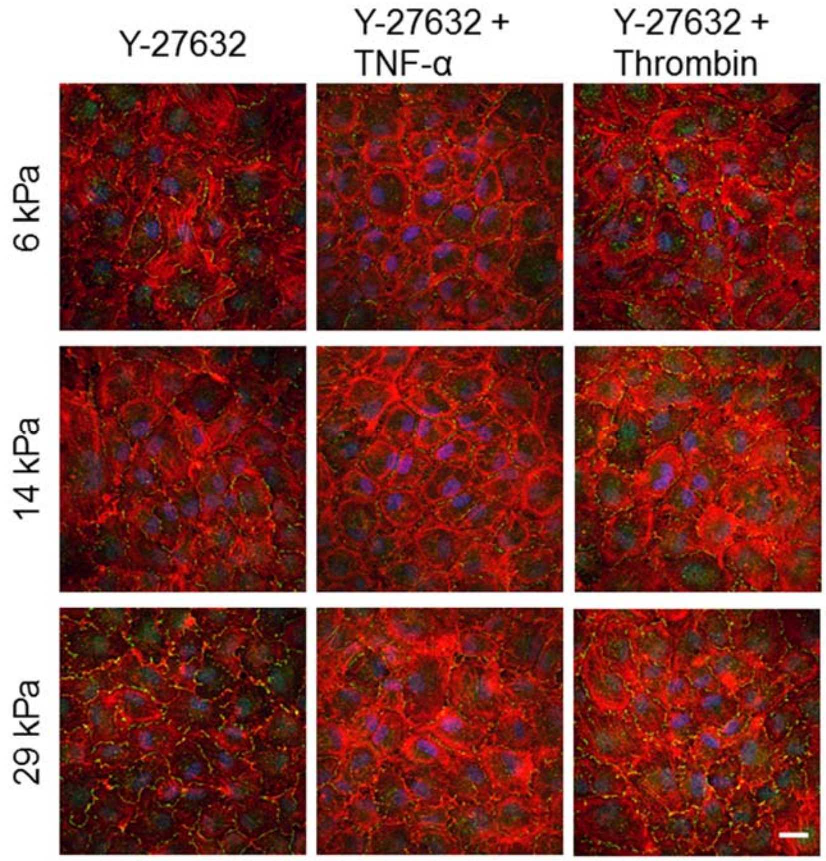

Figure 3.12. ROCK inhibition with Y-27632 abolished pMLC localization to actin fibers with TNF-α and thrombin treatment on all substrate stiffnesses. Cell monolayers on 6, 14, and 29 kPa substrates were pre-treated with 5 μM Y-27632 for 30 minutes prior to the addition of 10 ng/mL TNF (3 hours) or 10 U/mL thrombin (30 minutes). Samples were fixed and labeled for pMLC (green), actin (red), and nuclei (blue). Confocal z-stacks were acquired at 60X and compressed. Scale bar is 25 μm.

As shown in Figure 3.13, Y-27632 also abolished vinculin recruitment to adherens junctions in cells on 29 kPa gels following TNF-α and thrombin treatment. This result confirms the hypothesis that vinculin localization at cell-cell junctions was dependent on cell contractility. However, Y-27632 also adversely affected adherens junction morphology alone or concurrent with TNF-α or thrombin (Figure 3.14). Cell-cell junctions in all Y-27632-treated cells appeared invaginated, although no holes between cells were observed. This observation suggests that a basal level of cell contractility is necessary for normal junction structure. Taken together, these findings indicate that substrate-dependent cell contractility was responsible for vinculin localization to junctions in response to TNF-α and thrombin, but is also necessary for maintenance of normal reticular adherens junction morphology.

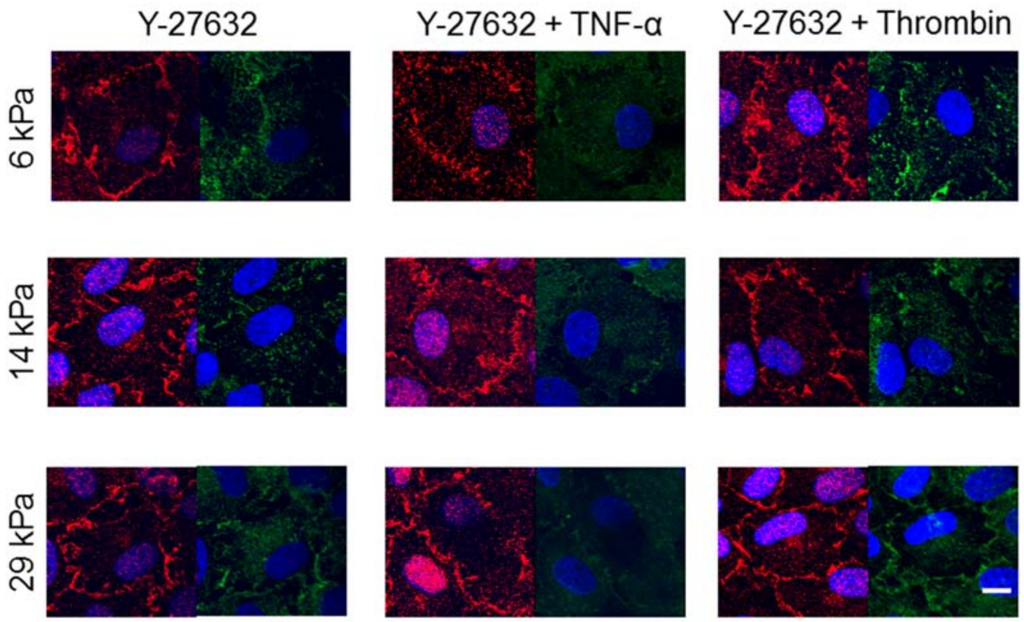

Figure 3.13. ROCK inhibition prevented vinculin localization to apical adherens junctions following TNF-α or thrombin treatment on all substrate stiffnesses. Cell monolayers on 6, 14, and 29 kPa substrates were pre-treated with 5 μM Y-27632 for 30 minutes prior to the addition of 10 ng/mL TNF (3 hours) or 10 U/mL thrombin (30 minutes). Samples were fixed and labeled for VE-cadherin (red), vinculin (green) and nuclei (blue). Images are the apical plane of representative cells from confluent monolayers. Scale bar is 10 μm.

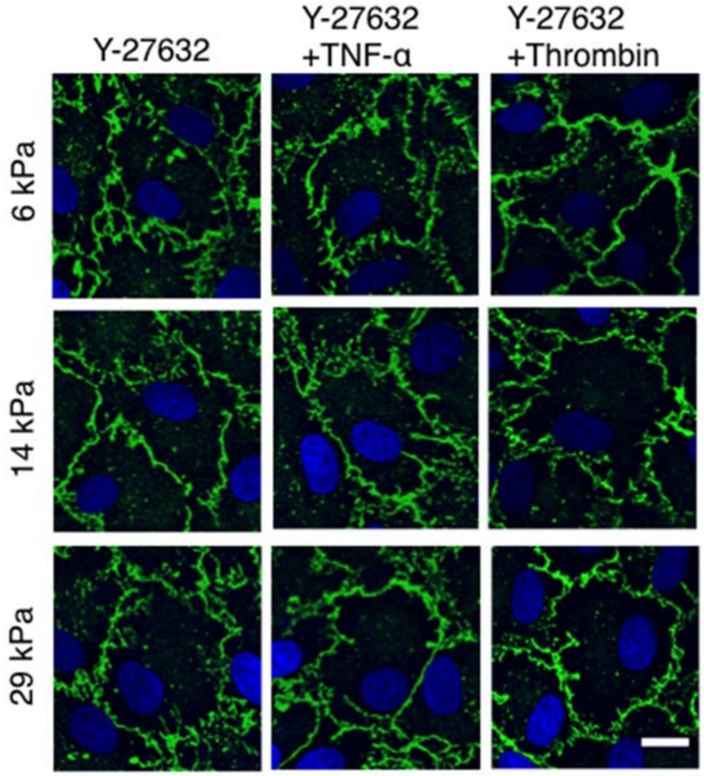

Figure 3.14. ROCK inhibition induced an invaginated cell-cell junction morphology that was unchanged by TNF or thrombin treatment. Cells were pre-treated with 5 μM Y-27632 for 30 minutes prior to the addition of 10 ng/mL TNF (3 hours) or 10 U/mL thrombin (30 minutes). Samples were fixed and labeled for β-catenin (green) and nuclei (blue). Confocal z-stacks were acquired at 60X magnification and compressed. Images show representative cells within confluent monolayers. Scale bar is 10 μm.

3.3.5. Functional ramifications of substrate stiffening: monolayer permeability and cell stiffness

We used an *in vitro* dextran diffusion permeability assay to see if morphological differences in adherens junctions with substrate stiffness and TNF-α and thrombin treatment corresponded to functional endothelial barrier disruption. Representative side-views of analyzed samples are shown in Figure 3.15a. The bright band at the top represents the fluorescent-dextran above the endothelial cell monolayer; the endothelial monolayer is approximately between the two dashed lines; and the area beneath the dashed lines represents the gel. To verify assay functionality, monolayers were treated with barrier enhancing BW245C or barrier degrading thrombin as negative and positive controls, respectively [134]. On 6 kPa gels, endothelial monolayer permeability increased by 28% with thrombin treatment and decreased by 16% with BW245C treatment (Figure 3.15b).

This assay was then used to determine endothelial monolayer permeability on 6, 14, 29, and 50 kPa gels under three treatment conditions: untreated, TNF-α-treated (10 ng/mL, 3 hours), or thrombin-treated (10 U/mL, 30 minutes) (Figure 3.15c). Monolayer permeability increased with substrate stiffness by n-way ANOVA ($p<0.001$). There was no significant interaction between substrate stiffness and TNF-α treatment. However, the interaction between substrate stiffness and thrombin treatment was significant ($p<0.05$). The fold increase in permeability between untreated and TNF-α or thrombin treated samples ranged between 1.23 and 1.75. These results indicate that substrate stiffness did not enhance TNF-α-induced endothelial monolayer permeability at the time point tested in this study on 6-50 kPa gel substrates. Substrate stiffness did enhance thrombin-induced monolayer permeability.

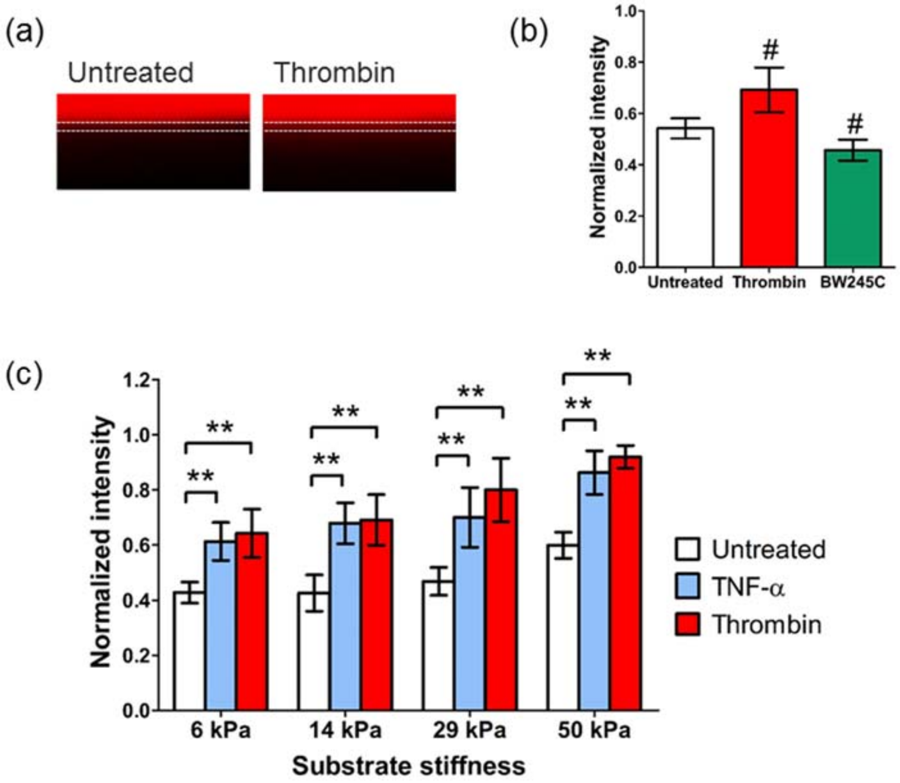

Figure 3.15. *In vitro* endothelial monolayer permeability increased with substrate stiffness and TNF-α and thrombin treatment. (a) Representative xz-images images of *in vitro* permeability samples with and without thrombin treatment. Dotted lines indicate the approximate location of the cell monolayer; the gel substrate is beneath the dotted lines. Monolayer permeability was quantified by measuring fluorescence intensity in the gel. Fluorescence values for each cell sample were normalized to the fluorescence in gels without cell monolayers; this output is referred to as normalized intensity, which increases with monolayer permeability (b) Normalized fluorescent intensity for cells treated with 10 U/mL thrombin or 1 μM BW245C for 30 minutes as positive and negative controls, respectively, for assay validation. (c) Monolayer permeability was measured in samples that were untreated, treated with 10 ng/mL TNF-α for 3 hours or treated with 10 U/mL thrombin for 30 minutes. The effect of stiffness ($p<0.001$) and treatment ($p<0.01$) were by significant by n-way ANOVA with a Tukey-Kramer post-hoc test (**$p<0.001$). The interaction between stiffness and thrombin was significant ($p<0.05$); however, there was no significant interaction between stiffness and either TNF-α.

In addition to endothelial barrier function, the ability of the endothelium to produce the vasodilator nitric oxide is key to healthy vascular function. Since nitric oxide production decreases with increasing endothelial cell stiffness, we studied changes in cell stiffness in response to TNF-α on substrates of different stiffness. The effect of substrate stiffness on changes in individual endothelial cell stiffness within a confluent monolayer in response to TNF-α was evaluated by AFM. The results are shown in Figure 3.16 as fold change in cell stiffness compared to untreated cells on the same stiffness substrate; fold change in stiffness >1 indicates cell stiffening while fold change <1 indicates cell softening. Cells on stiff 50 kPa PA gels were 1.37-fold stiffer than untreated cells after three hours of TNF-α treatment. Cell stiffness then decreased over 24 hours of TNF-α treatment. Cells on PA gel substrates of medium 14 kPa stiffness originally softened by 3 hours of TNF-α treatment and remained softer than untreated cells up through 24 hours of treatment. TNF-α -treated cells on soft 6 kPa gels also softened, reaching the greatest level of softening following 6 hours of treatment (0.65-fold) and remained soft. Interestingly, sub-confluent endothelial cells attached to glass initially stiffen and then soften over 24 hours of exposure to TNF-α [220]. These results demonstrate that substrate-dependent response to TNF-α extends beyond endothelial barrier loss to other key endothelial functions, possibly affecting nitric oxide production through changes in cell stiffness.

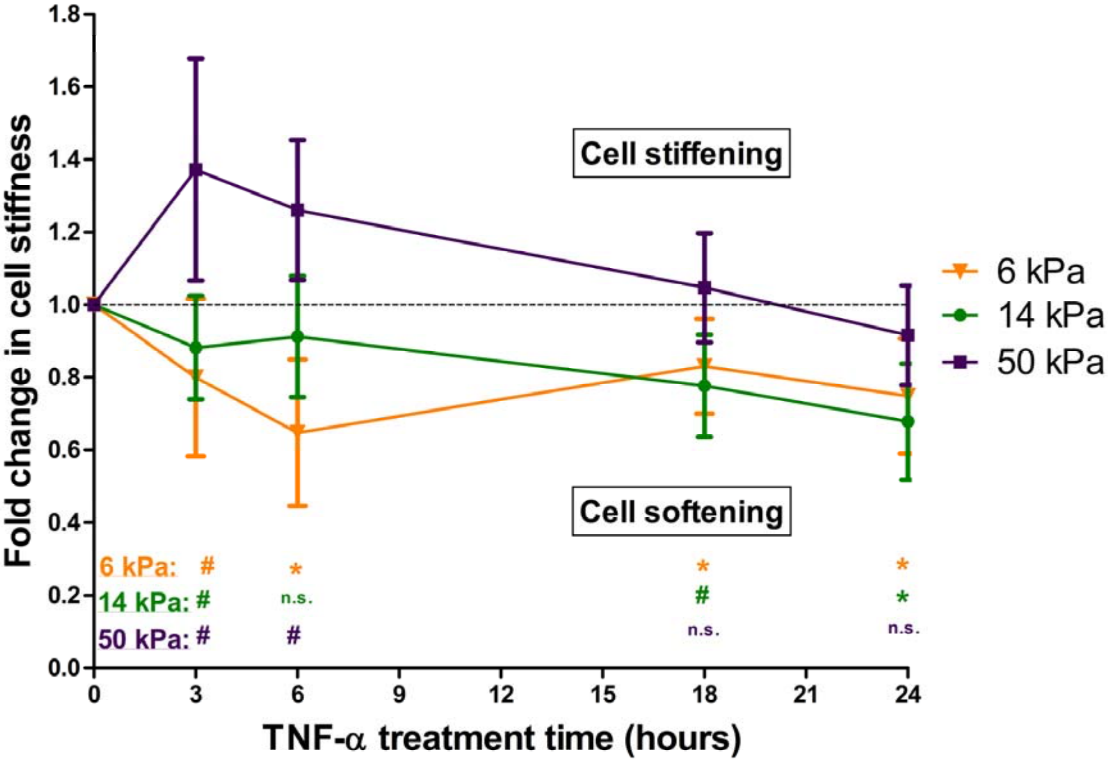

Figure 3.16. TNF-α treatment caused cells on stiff substrates to stiffen and then soften, while cells on soft substrates softened and remained soft. Cells were seeded on 6, 14, or 55 kPa PA gels and grown to confluency. Cells were treated with or without 10 ng/mL TNF-α, and cell stiffness was measured by AFM over 24 hours. Fold change in average cell stiffness was calculated relative to untreated cells on PA gel of the b same stiffness (# $p < 0.05$, * $p < 0.01$, n = 10 cells per sample). Data are shown as average ± standard deviation.

3.4. Discussion

While arterial stiffness is a major risk factor for cardiovascular disease and systemic inflammation is key to cardiovascular pathogenesis, it is not understood how these stimuli interact to induce endothelial barrier loss that is critical to atherosclerotic plaque development. In this study, we determined that sub-endothelial stiffness increased in elastin haploinsufficient (ELN+/-) mice. Vinculin recruitment to endothelial adherens junctions in the abdominal aorta, which requires cell-cell junction tension, was increased in ELN+/- mice *in situ*. *In vitro* experiments using PA gels of varying stiffness were conducted to further investigate the link between sub-endothelial stiffness, induced cell contractility, and cell-cell junction loss. We demonstrated for the first time that substrate stiffness enhanced vinculin recruitment to adherens junctions *in vitro* and increased cell-cell junction loss induced by TNF-α and thrombin. Substrate stiffness also enhanced ROCK-dependent cell contractility, and ROCK inhibition eliminated vinculin recruitment to junctions following exposure to TNF-α and thrombin. In an *in vitro* functional permeability assay, substrate stiffness exacerbated thrombin-induced, but not TNF-α-induced, barrier loss. In addition, cells on stiff substrates stiffened and cells on soft substrates softened in response to TNF-α; this result is significant because nitric oxide production inversely correlates with cell stiffness. Collectively, these studies support the hypothesis that increased substrate stiffness enhances ROCK-dependent cell-cell junction tension in response to inflammatory stimuli, translating to increased monolayer permeability in response to thrombin.

3.4.1. The protective role of vinculin against junction opening and therapeutic considerations

The recognized importance of vinculin, which is highly conserved among species, in the regulation of cardiovascular homeostasis is growing [310]. Vinculin localizes to endothelial adherens junctions under tension caused by treatment with VEGF, thrombin, or TNF-α. Vinculin at adherens junctions prevents force-induced junction loss in endothelial monolayers [178]. Observations supporting the idea that vinculin bolsters cell-cell junctions have also been made in epithelial cells; the expression of an α-catenin mutant incapable of binding vinculin decreased cell-cell attachment strength measured by a dual pipette assay [311]. Interestingly, the vinculin localization we see at adherens junctions in cells on stiff substrates indicates increased ROCK-dependent junctional tension, but also suggests a mechanism to compensate for increased tension and prevent junction loss on stiff substrates. Our results suggest that the vinculin/α-catenin complex plays a crucial role in endothelial barrier maintenance in response to cell contractility. In fact, it has been suggested that therapies to enhance the interaction between α-catenin and vinculin could combat endothelial barrier dysfunction [312].

More broadly, vinculin's beneficial role was recently demonstrated in cardiac muscle. Total cardiac output was increased in aged (24 months) compared to young (6 months) rats while cardiac output normalized to body weight was unchanged with age, suggesting a mechanism for age-related cardiac protective remodeling. Cardiac vinculin expression increased with age between 6 and 24 months, which coincided with increased vinculin localization at intercalated disks. In the same study, overexpression of cardiac vinculin enhanced the contractility of drosophila hearts and significantly increased fruit fly life span [313]. Taken together, these data support the notion that vinculin localization to cell-cell junctions is crucial to protective cardiovascular force-adaptation.

Endothelial cell contractility, specifically through the Rho/ROCK pathway, is also being considered as a possible therapeutic target for the treatment of pathological endothelial barrier loss. *In vitro* ROCK knockdown lessened the increase in endothelial permeability due to increasing substrate stiffness; *in vivo* treatment with the ROCK inhibitor Y-27632 improved endothelial barrier function in aged (20-25 months) mice to a level comparable to that of young (10-11 weeks) mice. The authors of this study suggested that the Rho/ROCK pathway may be a viable therapeutic target for the prevention of atherosclerotic plaques, citing both the ROCK inhibitor Fasudil and statins [134]. Fasudil has also been shown to prevent plaque formation and progression in a mouse model of atherosclerosis (ApoE knock-out), in addition to several other beneficial effects demonstrated in other animal studies [314, 315]. Recently, Rho/ROCK pathway inhibition has been suggested as a possible therapeutic strategy to curtail inflammation-induced vascular leakage in response to the Ebola virus [316]. In fact, the promise of Rho/ROCK as a therapeutic target for cardiovascular diseases is evident in a number of human studies; as of 2013, at least thirteen human studies involving Fasudil had been completed or were on-going [315]. While the results reported in this chapter support the therapeutic value of decreasing endothelial cell contractility, it is important to consider that some basal contractility level may be needed to maintain normal endothelium barrier function.

3.4.2. Proposed mechanism

We now present a potential mechanism for the substrate-dependent responses to TNF-α and thrombin. Endothelial monolayer focal adhesion activation is low on soft substrates (Figure 3.17a, b) and increased on stiff substrates (Figure 3.17c, d, e). Focal adhesions maintains a basal level of Rho/ROCK activation through focal adhesion kinase phosphorylation (pFAK). On soft substrates, TNF-α or thrombin-induced activation of the Rho/ROCK pathway is maintained at a low level due to low integrin activation (Figure 3.17b). On stiff substrates, the combination of substrate stiffness and either TNF-α or thrombin treatment increases Rho/ROCK signaling and cell contractility through phosphorylation of MLC. In the case of TNF-α (Figure 3.17d), cell contractility is sufficient to induce tension-dependent recruitment of vinculin to adherens junctions, which plays a protective role against junction opening. Despite increased contractility in response to TNF-α on stiff substrates, vinculin reinforcement prevents the exacerbation of junction loss by increased substrate stiffness. On stiff substrates, Rho/ROCK signaling is higher in response to thrombin (Figure 3.17e) than TNF-α, which translated to substrate-enhanced monolayer permeability.

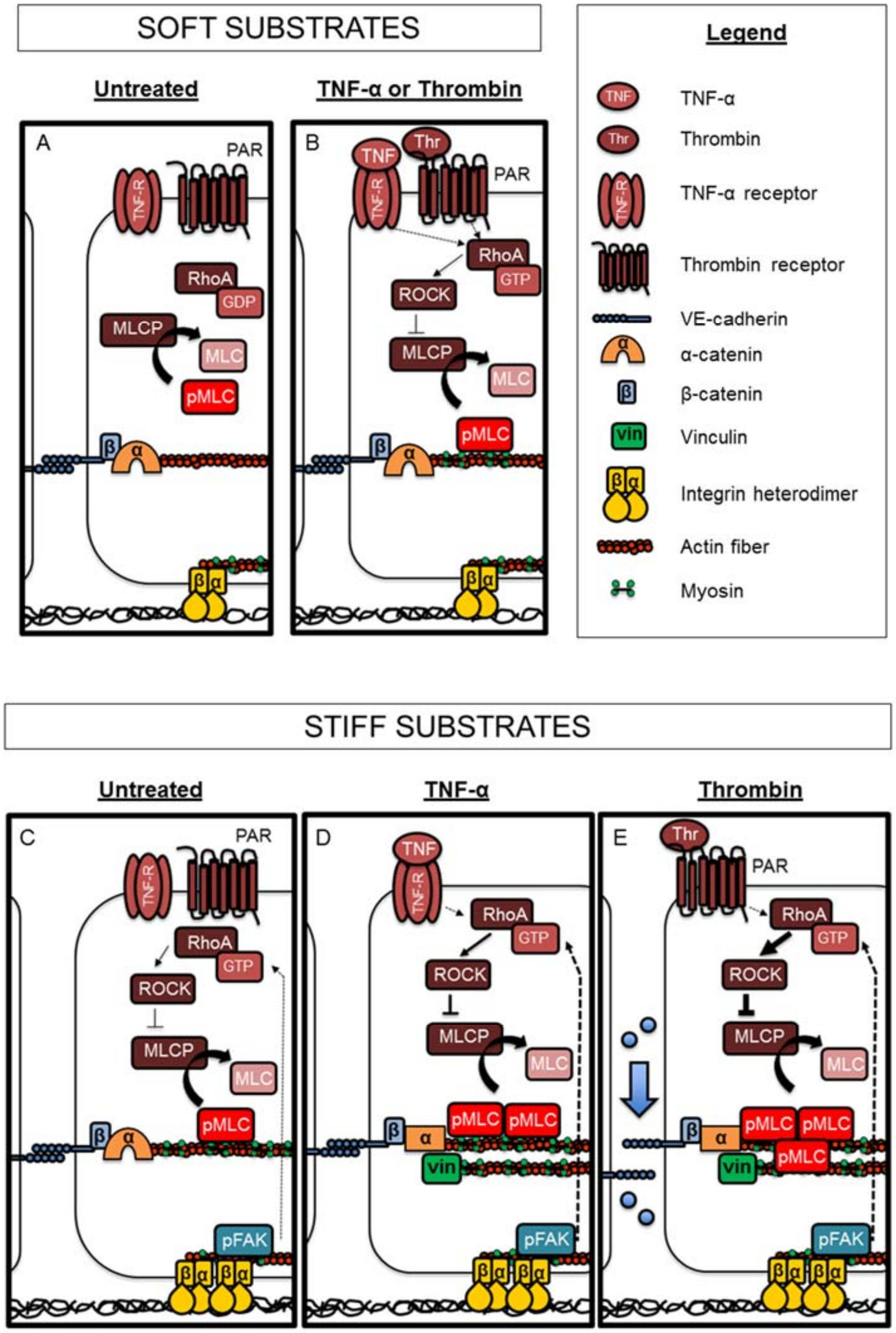

Figure 3.17. Proposed mechanism for substrate-dependent endothelial adherens junction loss in response to TNF-α and thrombin. (a) On soft substrates in untreated samples, TNF-α and thrombin receptor are present but not activated. (b) Both TNF-α and thrombin elicit low levels of Rho/ROCK signaling on soft substrates. (c) On stiff substrates there is a low level of basal Rho/ROCK activity. (d) TNF-α treatment on stiff substrates induces Rho/ROCK contractility and recruits vinculin to junctions, which provides a protective effect against junction opening. (e) Thrombin treatment induces a large increase in Rho/ROCK contractility that also recruits vinculin to junctions, but overwhelms to protective effect of vinculin.

3.4.3. Alternative signaling pathways

While these data support the role of cell contractility endothelial adherens junction integrity, loss of junction integrity is not purely mechanical. In fact several biochemical signaling pathways are involved in junction loss, including cell-cell junction protein phosphorylation [317, 318]. For example, in human lung microvascular and pulmonary artery endothelial cells *in vitro*, TNF-α induced VE-cadherin, β-catenin, γ-catenin, and p120 catenin phosphorylation. Increased monolayer permeability following TNF-α treatment was completely eliminated by pre-treatment with the protein tyrosine kinase inhibitors genistein, herbimycin A, and geldanamycin [319]. In addition, TNF-α induces reactive oxygen species (ROS) production in the endothelium, which can contribute to adherens junction loss [184]. This alternative pathway is further investigated in the next chapter. Successful therapies to treat or prevent endothelial permeability may need to address both contractility-dependent and contractility-independent barrier loss.

3.4.4. Similarities and differences between the endothelium *in vivo* and cultured endothelial cells *in vitro*

This study highlights important differences between endothelial cells *in vivo* and *in vitro*. One clear difference is in adherens junction morphology. While PAECs displayed large adherens junctions *in vitro*, endothelial cells in the mouse aorta displayed small, less pronounced junctions between adjacent cells that appear similar to the "reticular" junctions. However, the study of reticular adherens junction in cultured endothelial cells is still informative to the behavior of the endothelium *in vivo*, as reticular junctions in intact vessels contain the same junction proteins as reticular junctions *in vitro* [186]. This difference in adherens junction morphology may be due to the fact that the cells in culture are not exposed to shear strain or cyclic stretch; the static culture environment may enable more stable junction formation. In a published study, HUVECs exposed to physiological shear stress for 48 hours exhibited small reticular junctions similar to those seen *in vivo* [320].

There were also striking differences in focal adhesion size between endothelial cells *in vitro* and *in vivo*. Cultured cells (particularly on stiff substrates, as shown in Figure 3.11) form large focal adhesions containing both vinculin and the signaling molecule pFAK, even in the absence of biochemical stimuli. Strikingly, focal adhesions are considerably smaller in the intact mouse endothelium and generally do not contain pFAK under resting conditions. pFAK was observed at focal adhesions in areas where the endothelium had been damaged prior to fixation of the vessel (data not shown). This difference in focal adhesion size between *in vitro* and *in vivo* endothelial cells may explain the differences observed in actin cytoskeletal structure, as basal actin fibers originate from focal adhesions. *In vivo*, where focal adhesions are generally small, few basal actin fibers are observed; conversely, endothelial cells *in vitro* have both large focal adhesions and significant amounts of basal stress fibers. These observations have implications for the transition between *in vitro* and *in vivo* testing; treatments that normally elicit major actin-dependent morphological changes *in vitro* may produce less dramatic effects *in vivo*.

In addition, under the conditions that we tested, there was very little to no pFAK at cell-cell junctions in PAECs on the PA gel substrates used in this study. pFAK was observed at cell-cell junctions in the ELN+/- aortic endothelium (Figure 3.5C). The function of pFAK at endothelial cell-cell junctions is still under investigation. In cultured human pulmonary artery endothelial cells (HPAECs), treatment with sphingosine 1-phosphate, which promotes barrier integrity, induced pFAK translocation to cell-cell junctions [321]. Conversely, in response to VEGF, FAK co-localized with VE-cadherin *in vitro* and *in vivo* and played a role in increasing vascular permeability [322]. FAK activity at cell-cell junctions may also play a key role in the control of the endothelial barrier in the context of cancer; VEGF-dependent tumor metastasis into the lungs was decreased through FAK knock-down in mice [323]. In this work, increased pFAK labeling at ELN+/- aortic endothelial cell-cell junctions suggests decreased endothelial barrier function or increased junction turnover.

In both *in vitro* and *ex vivo* immunofluorescent labeling, pFAK was detected in the endothelial nuclei. While the role of pFAK in the nucleus is not completely clear, some studies have suggested that FAK may modulate gene expression through interacting with transcription factors [324, 325]. In neonatal rat ventricular myocytes, FAK localized to the nucleus following the application of 10% static strain for 30 minutes, suggesting FAK translocation to the nucleus is mechanosensitive [326]. Recent published studies have suggested that pharmacological FAK inhibition may prevent TNF-α-induced inflammatory vascular cell adhesion molecule-1 (VCAM-1) expression through FAK's role as a nuclear scaffold protein [327]. As nuclear localization of pFAK was observed in both cultured endothelial cells and the intact mouse aortic endothelium, this represents an area of possible further investigation. Since early results indicate that FAK translocation to the nucleus is mechanosensitive and occurs in response to inflammation, FAK's ability to act as a nuclear scaffold protein may represent another mechanism for biomechanical and biochemical cross-talk in the endothelium.

3.5. Study limitations

While our research demonstrates important interactions between substrate stiffnes and inflammation, it is not without limitations. First, the *in vitro* model chosen to study the effects of vessel stiffness, polyacrylamide gels, does not accurately replicate vessel mechanical properties. While this *in vitro* system has been widely used to investigate the effects of substrate stiffness on cultured cells, the mechanical properties of PA gels differ from those of tissues. Namely, PA gels are linearly elastic while most tissues are viscoelastic [56, 328]. A recently published study demonstrated that degree of viscoelasticity affected cell spread area, proliferation, and nuclear translocation of the transcriptional co-activator Yes-associated protein (YAP). In particular, fibroblasts were unable to spread on elastic substrates with initial modulus of 1.4 kPa; yet cells spread, formed actin stress fibers and large focal adhesions on stress-relaxing substrates with the same initial modulus [329]. Whether or not stress-relaxing materials will reveal additional substrate-dependent effects on contractility-dependent barrier loss of endothelial monolayers has yet to be investigated.

Our *in vitro* model is also limited by the lack of shear stress, which in constantly present in blood vessels *in vivo*. Systems capable of applying shear stress to endothelial cells on substrates of varying stiffness have been published within the last year [330, 331]. Following 5 hours of flow adaptation, cells on 30 kPa substrates were more sensitive to TNF-α than cells on 3 kPa substrates, as determined by translocation of the transcription factor NF-κB to the nucleus; however, TNF-α sensitivity was normalized between cells on 3 and 30 kPa substrates following 24 hours of flow adaptation [331]. In another system, shear stress-induced RhoA activation was lower in cells on 2.5 kPa substrates compared to cells on 10 kPa substrates and glass. Cell-cell junction width was higher in cells on 10 kPa substrates compared to cells on 2.5 kPa substrates in both static and shear stress samples. Shear stress decreased cell-cell junction width in cells on 2.5 and 10 kPa substrates [330]. These published studies demonstrate that shear stress can modulate cell response to substrate stiffness *in vitro*; thus, the addition of shear stress to our model would more closely simulate conditions *in vivo* and improve our understanding of how vessel stiffness affects endothelial cell response to inflammatory conditions.

The results presented in this chapter demonstrated that ROCK-dependent cell contractility was necessary for vinculin translocation to cell-cell junctions in response to TNF-α and thrombin on stiff substrates. ROCK increases the availability of activated myosin by direct phosphorylation of myosin light chain (MLC) and preventing de-phosphorylation of MLC through inhibiting myosin phosphatase [126]. However, the contractility pathway is composed of multiple signaling molecules, beyond those illustrated in Figure 3.17. The enzyme myosin light-chain kinase (MLCK) also phosphorylates myosin light chain, yet the role of MLCK in substrate-dependent contractility was not specifically presented in this chapter [144]. In our preliminary studies on MLCK inhibition, treatment with the MLCK inhibitor ML-7 resulted in diminished peripheral actin and loss of junctions between cells on glass (data not shown). This observation might be explained by published reports on the differential roles of MLCK and ROCK in cell contractility. In single fibroblasts, ML-7 treatment eliminated peripheral actin fibers, while ROCK inhibition by Y-27632 eliminated longitudinal actin fibers but maintained peripheral actin fibers [139]. The fact that ML-7 treatment resulted in cell-cell junction loss suggests that basal peripheral actinomyosin contractility is necessary for junction maintenance in our cells. In addition, ROCK has been implicated in increased permeability of untreated endothelial cell monolayers with substrate stiffening. Thus, while Y-27632 only inhibits part of the contractility pathway, ROCK was the most relevant component based on our own observations and those in published literature.

4. Effect of substrate stiffness on ROS production and non-contractile endothelial adherens junction loss

4.1. Introduction

Endothelial adherens junction loss can occur due to increased actinomyosin cell contractility, as discussed in the previous chapter, or through alternative mechanisms. Specifically, TNF-α activates the Rho GTPase Rac, which is involved in the production of reactive oxygen species (ROS) through NADPH oxidase and src-dependent phosphorylation and internalization of adherens junction proteins [184]. ROS are a family of highly reactive oxygen-containing molecules, as detailed in Chapter 1, which plays an important role in a variety of signaling pathways, such as cell proliferation and survival, metabolism, and iron homeostasis [332]. This chapter focuses on the role of ROS in substrate stiffness-dependent endothelial adherens junction loss.

While physiological ROS production is important to healthy cellular function, ROS over-production is pathological and referred to as "oxidative stress". Oxidative stress has been implicated in the pathogenesis of both hypertension and atherosclerosis; yet it is still unclear whether ROS production is an early causative factor or a consequence of these cardiovascular diseases [333]. In an ApoE-/- mouse model of atherosclerosis, increased NADPH oxidase (NOX2) expression in the endothelium preceded plaque development, and NOX knock-down decreased lesion size, which suggests a causative role [334]. In humans, women with hereditary NOX2 deficiency exhibited lower intima-media thickness, an indicator of atherosclerotic burden, compared to age-matched controls [335]. While superoxide is likely produced in many stages of atherosclerosis, these findings suggest superoxide may play an early role in endothelial barrier dysfunction prior to atherosclerotic plaque initiation.

Since a variety of pathways are activated in endothelial cells following TNF-α exposure, it is difficult to isolate the effect of any one pathway (in this case, the ROS pathway). Therefore, to isolate the effect of substrate stiffness on endothelial cell ROS production, we chose an activator of protein kinase C (PKC) widely used as a positive control for ROS production—phorbol 12-myristate 13-acetate (PMA). In published studies, PMA treatment increased endothelial monolayer permeability but did not increase markers of actinomyosin contractility, such as silicon substrate wrinkling, myosin light chain (MLC) phosphorylation or myosin light chain kinase (MLCK) activation [144, 207]. Other studies have suggested that phorbol esters may induce barrier loss through intermediate filament reorganization (vimentin or caldesmon effects) or actin cytoskeleton reorganization [209, 211, 336]. Thus, PMA represents a permeability-inducing stimulus dependent on ROS production instead of actinomyosin contractility.

The role of vessel or substrate stiffness in modulating ROS production in endothelial cells has been largely unstudied, although endothelial superoxide production is mechanosensitive, specifically in response to shear stress [337]. Cultured bovine aortic endothelial cells produced three times more superoxide under oscillatory shear stress compared to laminar flow [338]. Shear stress activates Rac, which is downstream of integrin activation and contributes to ROS production [339, 340]. In endothelial cells, the effect of substrate stiffness-dependent integrin activation has not been reported. In epithelial cells, MMP-3-stimulated ROS production was approximately 3.5-fold higher on 4.02 kPa substrates compared to 0.13 kPa substrates; β1 integrin sub-unit knock-down eliminated ROS production in response to MMP-3 [215]. These findings support earlier studies in fibroblasts showing that integrin activation regulates Rac1 localization [217]. Thus, **we hypothesized that substrate stiffening increases endothelial ROS production, resulting in increased non-contractile actin fiber formation and cell-cell junction loss**.

This chapter presents both *in vitro* and *ex vivo* data on the effect of substrate and vessel stiffness, respectively. Using the polyacrylamide gel substrate system introduced in Chapter 3, we studied PMA-induced junction loss and actin fiber reorganization through immunofluorescent labeling. A live cell ROS assay was used to assess ROS production on substrates of varying stiffness. Abdominal aortae were dissected from wild type and elastin haploinsufficient mice (shown to have varying sub-endothelial stiffness in Chapter 3) and treated with PMA *ex vivo* prior to actin cytoskeleton visualization by *en face* confocal imaging. In this chapter we present data showing, for the first time, that substrate stiffness enhances ROS production in endothelial monolayers *in vitro*.

4.2. Methods

4.2.1. Cell culture and polyacrylamide (PA) gel sample preparation

Porcine aortic endothelial cells (PAEC) were cultured as described previously and used up to Passage 9. When used in the ROS and PKC kinase activity assays, cells were seeded on PA gel substrates in phenol-red free DMEM containing 5% FBS, 1% PSG and serum-starved overnight in phenol-red free DMEM containing 1% FBS, 1% PBS. PA gel substrates were prepared as described previously; the size and volume of gel solution used to prepare samples for each type of assay are provided below.

4.2.2. Immunofluorescence (*in vitro* and *ex vivo* samples)

In vitro samples on glass coverslips and PA gel substrates were fixed, permeabilized, and labeled for immunofluorescence as described previously. For cell imaging on gels, 12 mm circular PA gel substrates were prepared using 50 μL gel solution. Cells on 12 mm circular glass coverslips were mounted using 1:1 glycerol:PBS solution prior to imaging. Mouse aortae were fixed with ice-cold 4% paraformaldehyde solution, blocked and permeabilized simultaneously in PBS containing 1% BSA and 0.3% TritonX-100. Actin and nuclei were labeled using 16.5 nM rhodamine phalloidin and 0.2 μg/mL bisbenzimide, respectively, prior to mounting in 1:1 glycerol:PBS. Confocal image z-stacks were acquired for all samples with either a 0.25 or 0.5 μm step size (for *in vitro* and *ex vivo* samples, respectively) using an Olympus Fluoview 1000 confocal microscope.

4.2.3. Matlab image analysis

Custom Matlab code was created to extract quantifiable data from confocal images of cells on polyacrylamide gel substrates. For all experiments in this chapter, confocal z-stacks were acquired to capture immunofluorescence through the entire endothelial layer, then images in the z-stack were compressed to produce to one image per z-stack. For samples labeled for phosphorylated myosin light chain (pMLC), background was subtracted using a 50x50 pixel area. Images were then binarized. The threshold for binarization was determined using Otsu's method, which calculates a threshold for each image based on the distribution of pixel intensities within that image

[277]. Noise was removed from binarized images by excluding any objects (also referred to as “connected components”) smaller than 30 pixels. The number of remaining pixels with intensities above the threshold (pMLC “positive” pixels) was counted for each image. Three images per sample were quantified using this method and averaged to calculate the MLC activation in each sample.

For the ROS assay, image processing and quantification were conducted using a similar process. Background was subtracted using a 50x50 pixel region, images were binarized by Otsu’s method, and connected components smaller than 9 pixels were discarded to remove noise. Remaining “positive” pixels were counted. The mean pixel counts for three images were calculated to produce the final quantification of ROS production per sample.

4.2.4. PKC kinase activity assay

PAECs were seeded in 6-well dishes or on 22x22 mm PA gels in 6-well dishes and allowed to reach confluence over three days. Cells were serum-starved in 1% FBS-containing medium overnight prior to use in the assay. Cells were treated with 1 µM PMA for the times indicated in individual figures, then rinsed quickly with ice-cold PBS. For cells on tissue culture plastic, 50 µL of lysis buffer (20 mM MOPS, 50 mM β-glycerolphosphate, 50 mM sodium fluoride, 1 mM sodium orthovanadate, 5 mM EGTA, 2 mM EDTA, 1% NP40, 1 mM dithiothreitol, 1 mM benzamidine, 1 mM phenylmethanesulphonylfluoride, 10 µg/mL leupeptin, 10 µg/mL aprotinin) was added to each well. For cells on gel substrates, gels were removed from the 6-well plate in which they were seeded and excess liquid was removed by gently dabbing the side of each gel on a Kimwipe. Gels were then inverted into a new 6-well plate containing 50 µL lysis buffer, and cells were lysed for 10 minutes at 4°C. Lysed cells were scraped from the plastic or gel substrates, and lysate was collected into pre-chilled Eppendorf tubes. For gel samples, the lysates from at least two samples were combined to obtain enough lysate material. Lysates were centrifuged at 4°C for 15 minutes at 13,000 rpm, and supernatants were transferred to new pre-chilled tubes. Protein concentration was determined by BCA assay. For each sample, 30 µL clarified lysate was used in the ELISA-based PKC kinase assay (Enzo) following manufacturer's instructions. Briefly, control or sample lysates were incubated with ATP for 90 minutes at 30°C in a 96-well microtiter plate pre-coated with a PKC substrate, which is phosphorylated by active PKC. The 96-well plate was manually shaken every 20 minutes. The reaction was stopped by removing the contents of the plate. A phosphospecific substrate antibody was added to each well and incubated for 60 minutes at room temperature with gentle manual shaking every 20 minutes. The plate was washed and then incubated with anti-rabbit IgG:HRP conjugate for 30 minutes at room temperature with gentle manual shaking every 10 minutes. The plate was washed and then incubated with the tetramethylbenzidine substrate for 30 minutes, during which time color developed in the plate proportional to PKC phosphotransferase activity. Plate development was stopped by adding acid stop solution, and absorbance at 450 nm was measured on a microplate reader (Thermo Labsystems, Multiskan Spectrum). Relative kinase activity was calculated using the equation:

$$Relative\ kinase\ activity = \frac{(Average\ absorbance_{sample} - Average\ absorbance_{blank})}{Quantity\ of\ crude\ protein\ used\ per\ assay}$$

4.2.5. ROS assay

Thin circular PA gels were prepared using 5 µL PA gel solution between a 22x22 mm square hydrophilic bottom coverslip and 12 mm diameter circular hydrophobic top coverslip. Gels were coated with collagen as described previously. Gels or collagen-coated 35 mm glass-bottom dishes were seeded with cells in phenol red-free DMEM containing 5% FBS, 1% PSG as previously described and allowed to reach confluence. Cells were serum-starved in phenol red-free DMEM containing 1% FBS, 1% PSG overnight prior to the assay. Samples were treated with 1 µM PMA for the durations specified in each figure. For a positive control, cells in glass-bottom dishes were treated with 100 µM tert-butyl hydroperoxide (tBHP) for 60 minutes. The general oxidative stress dye 5-(and 6)-chloromethyl-2',7'-dichlorodihydrofluorescein diacetate (CM-H2DCFDA) was reconstituted in dimethyl sulfoxide (DMSO) and then diluted into warmed phenol red-free medium at a final concentration of 25 µM. The treatment (either PMA or tBHP) was removed from the cells, followed by one rinse with warmed HBSS buffer (0.137 M NaCl, 5.4 mM KCl, 0.25 mM Na_2HPO_4, 5.6 mM glucose,0.44 mM KH_2PO_4, 1.3 mM $CaCl_2$, 1.0 mM $MgSO_4$, 4.2 mM $NaHCO_3$). CM-H2DCFDA was added to each sample (400 µL), and incubated for 25 minutes in a 37°C incubator, protected from light. To label nuclei, bisbenzimide was added to each sample for a final concentration of 0.2 µg/mL. The samples were returned to the dark incubator for an additional 5 minutes, then rinse twice with warmed HBSS buffer. Samples were immersed in warmed phenol red-free media and transferred to the Olympus Fluoview 1000 microscope. Samples were imaged by acquiring z-stack images with a 1 µm step size.

4.2.6. *Ex vivo* vessel treatment

The abdominal aorta was dissected from wild type (WT, C57BL/6) or elastin haploinsufficient (ELN+/-) mice and immersed in cold HEPES buffer (140 mM NaCl, 5 mM KCl, 1 mM $CaCl_2$, 1.2 mM $MgSO_4$, 1.2 mM Na_2HPO_4, 10 mM HEPES, 10 mM sodium acetate, 5 mM glucose, pH 7.4) while excess adipose tissue was removed from the outside of the vessel. Untreated segments were fixed immediately following dissection. Treated aortic segments were cannulated (Figure 4.1), submerged in a bath of HEPES buffer maintained at 37°C, pressurized to 80 mmHg, and allowed to equilibrate for 30 minutes. DMEM containing 5 μM PMA was administered intraluminally through the cannulation set-up, and the vessel was re-pressurized to 80 mmHg for the duration of the 30-minute treatment time. Ice-cold 4% paraformaldehyde was then simultaneously administered intraluminally and added to the bath. The vessel was fixed for 30 minutes, then cut open longitudinally and pinned flat with insect pins for the immunofluorescent labeling process (described above).

4.2.7. Statistical analysis

All statistical analyses were conducted using Matlab's statistical toolbox. Graphs represent mean ± standard deviation. Multiple groups were compared using either two-way or n-way ANOVA with post-hoc Tukey-Kramer test, and two groups were compared by Student's t-test. Within each PKC assay, conditions were tested in duplicate. For measurement of ROS production, conditions were tested in triplicate. All experiments were run at least two times, excluding ex *vivo* immunofluorescent labeling.

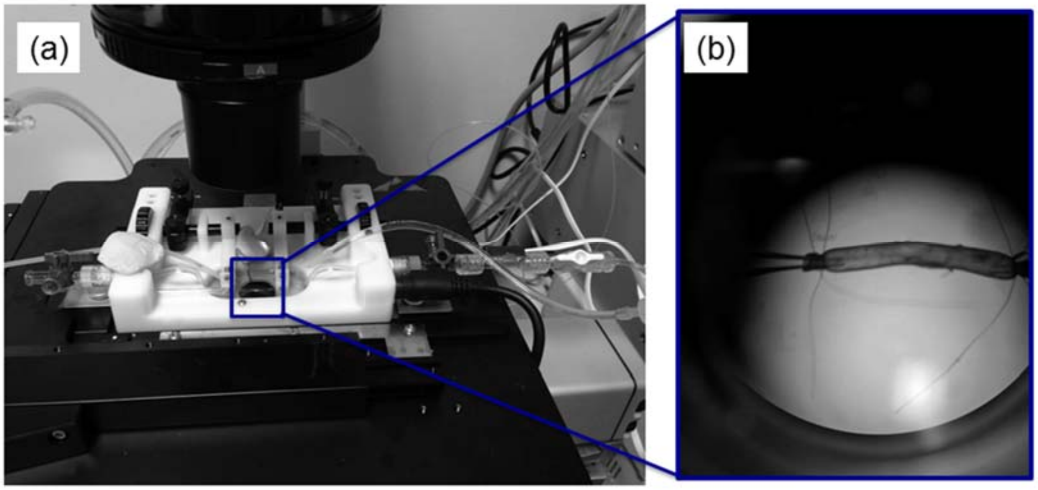

Figure 4.1. Vessel pipette cannulation set-up. (a) Cannulation apparatus (white) was placed on a microscope stage. Treatments were administered to the vessel intraluminally through tubing connecting to glass pipettes. A temperature-controlled bath held the cannulated vessel, as viewed through the microscope in (b). Aortic segments were affixed to glass pipettes using black string.

4.3. Results

4.3.1. Timing and magnitude of ROS production in cultured endothelial cells on substrates of different stiffness

To assess the timing of when PMA induced endothelial cell ROS production, ROS levels were measured in PAEC on glass following PMA treatment for 5 to 30 minutes (Figure 4.2). Nuclear labeling (left, Hoechst) confirmed the presence of cells in the field of view. ROS production (right, CM-H2DCFDA) was not detected in the untreated sample, but was elevated in the positive control (tBHP). ROS production peaked with 10 minutes (2.5-fold) of PMA treatment and diminished nearly to control levels with 30 minutes of PMA treatment. Based on this time course, cells on 6, 14, and 29 kPa gels were treated with PMA for 10 minutes.

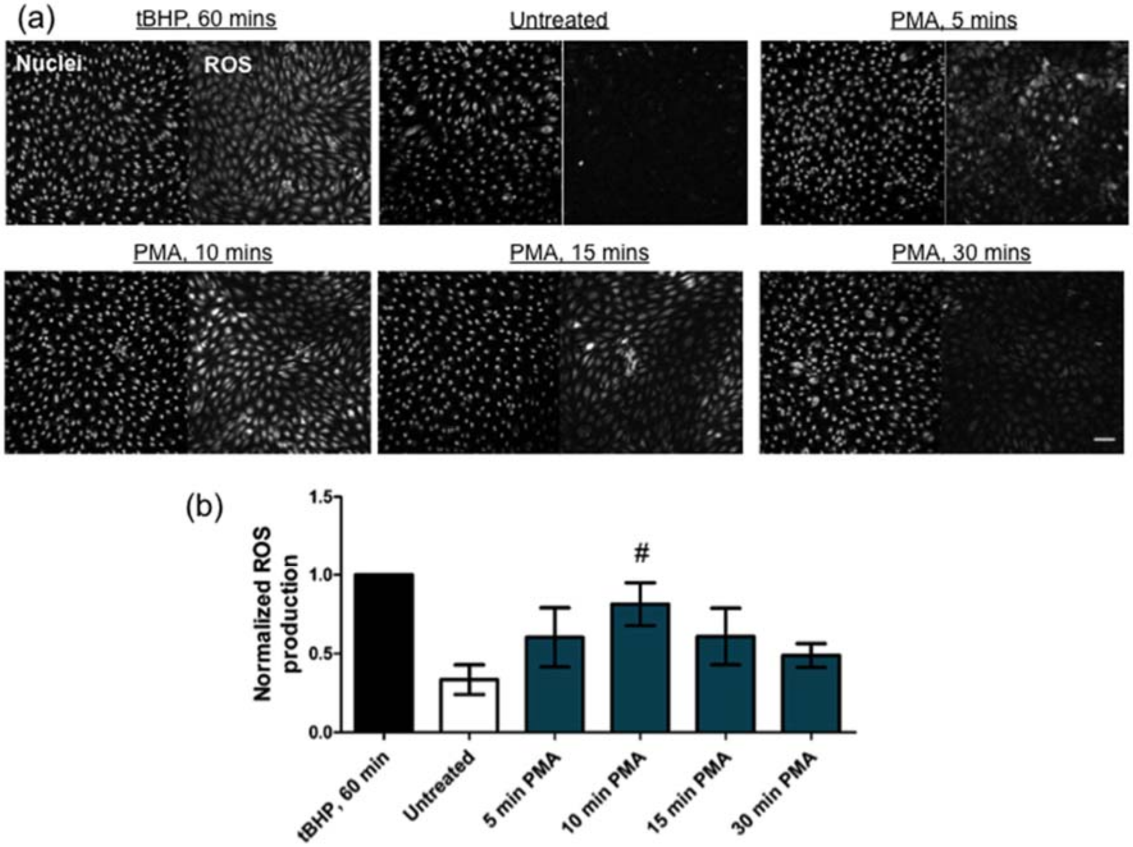

Figure 4.2. ROS production peaked with 10 minutes of PMA treatment for endothelial cells on glass. (a) PAEC monolayers were treated with 1 μM PMA for 0, 5, 10, 15, or 30 minutes to determine ROS production timing. Cell nuclei were labeled with Hoechst (left), and ROS was fluorescently detected using CM-H2DCFDA (right). Samples were imaged by confocal microscopy at 20X magnification and confocal z-stacks were compressed. Scale bar is 25 μm. (b) ROS production was quantified using custom Matlab code. PMA-treated samples were normalized to the positive control (100 μM tBHP, 60 minutes). #$p<0.05$ compared to untreated samples by Student's t-test.

To test the hypothesis that ROS production increases with substrate stiffness, cells on 6, 14, and 29 kPa gels were treated with 1 μM PMA for 10 minutes prior to ROS detection by CM-H2DCFDA. ROS in untreated samples was minimal on all substrate stiffnesses (Figure 4.3). On 6 kPa substrates, there was no significant difference in detected ROS between untreated and PMA-treated cells; on 29 kPa substrates, the increase in detected ROS following PMA exposure was approximately 1.5 fold over untreated cells. By one-way ANOVA, fold change in ROS increased with substrate stiffness (p<0.01). These results demonstrate that substrate stiffening increases ROS in response to PMA in cultured aortic endothelial cells.

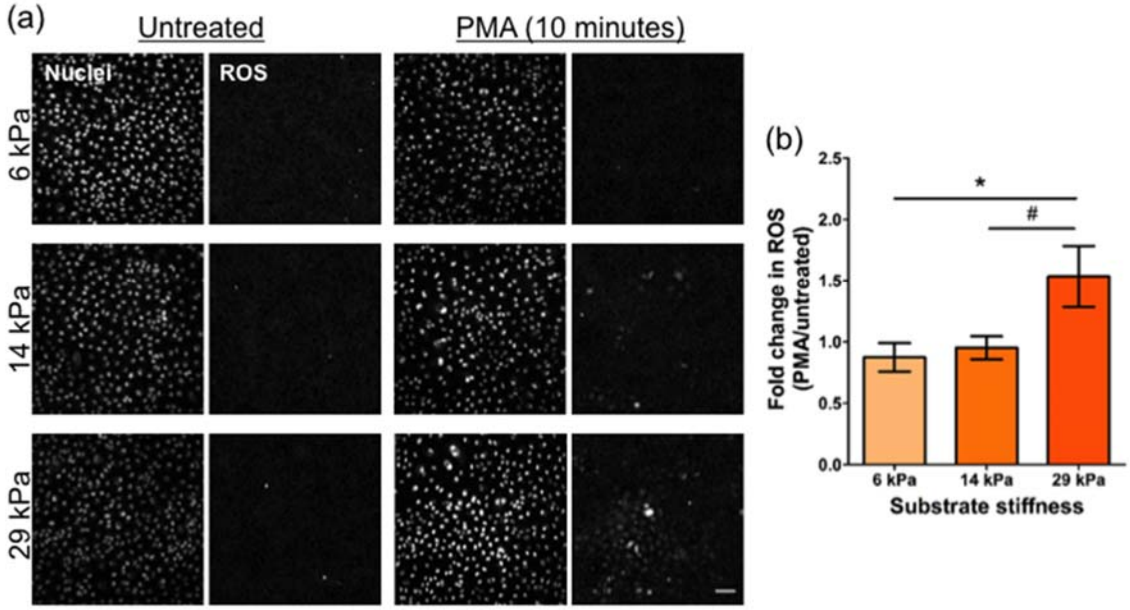

Figure 4.3. ROS increased with substrate stiffness following PMA treatment. (a) PAEC monolayers on 6, 14, and 29 kPa gels were treated with 1 μM PMA for 10 minutes. Cell nuclei were labeled with Hoechst (left), and ROS was fluorescently detected using CM-H2DCFDA (right). Samples were imaged by confocal microscopy at 20X magnification and confocal z-stacks were compressed. Scale bar is 25 μm. (b) ROS production was quantified using custom Matlab code. PMA-treated samples were normalized to untreated samples on the same substrate stiffness. The effect of substrate stiffness was significant by one-way ANOVA (p<0.01). #p<0.05, *p<0.01 by post-hoc Tukey-Kramer test.

4.3.2. Role of PKC activation, actin reorganization, and actinomyosin contractility in endothelial cell response to PMA on substrates of different stiffness

Since PMA is known to induce ROS production through PKC signaling, a PKC kinase activity assay was used to determine if PKC activation increased on stiffer substrates. To determine the duration of PMA stimulation needed to elicit PKC activation, PAECs on tissue culture plastic were treated with PMA for 5 or 10 minutes.

PKC activity in cells on tissue culture plastic increased 3.7-fold following 5 minutes of 1 μM PMA treatment, and this activation level was sustained following 10 minutes of treatment (Figure 4.4a). Based on this time course, cells on 6, 14, or 29 kPa gel substrates were exposed to PMA for 5 minutes prior to measuring PKC kinase activity. PMA increased PKC activity 2.6=2.9 fold for cells on substrates of varying stiffness (Figure 4.4b). By two-way ANOVA, the PMA effect was significant ($p<0.001$), while the stiffness effect was not significant. Therefore, substrate-dependent differences in PKC activation did not account for increased ROS production on stiffer substrates in response to PMA.

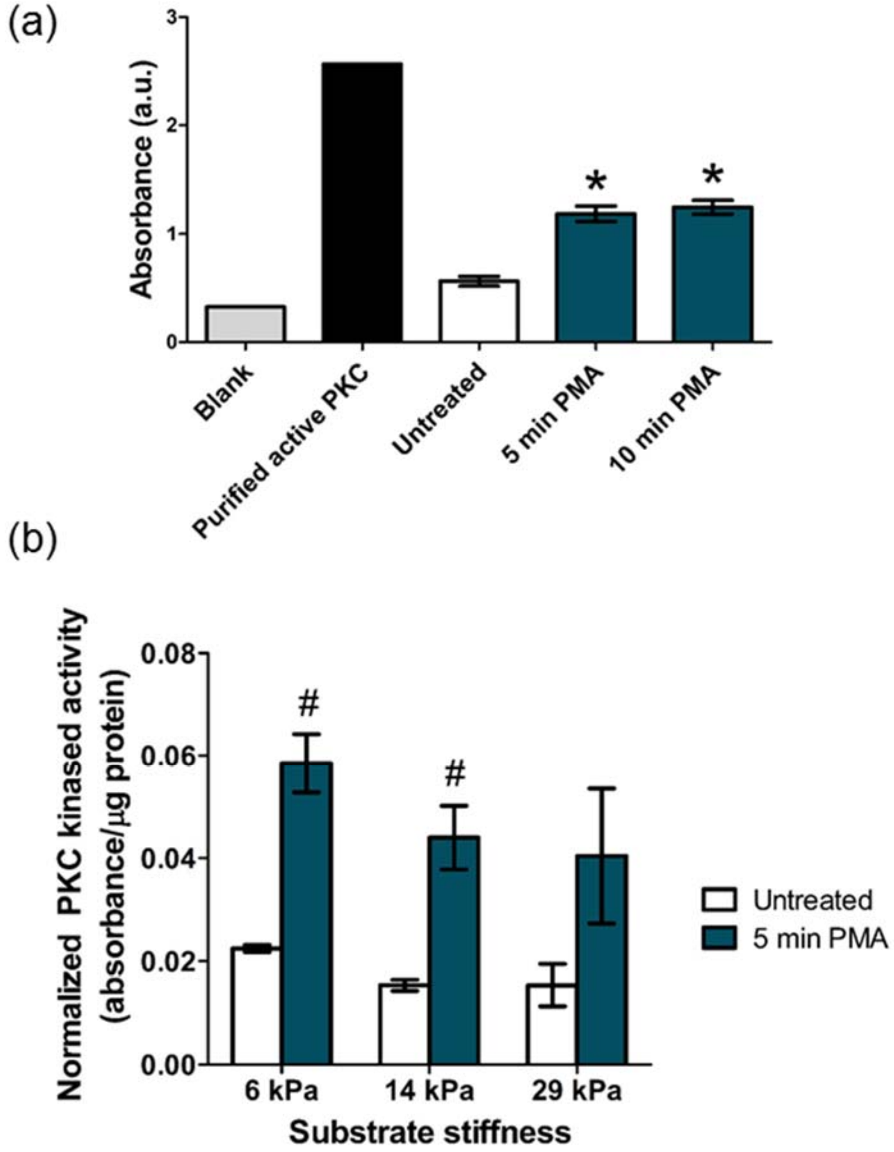

Figure 4.4. PKC kinase activity increased by 5 minutes following PMA exposure in endothelial cells on PA gels independent of substrate stiffness. (a) PKC kinase activity was measured following 1 μM PMA treatment in cells on tissue culture polystyrene. Purified active PKC was the positive control. $*p<0.01$ compared to untreated by Student's t-test (b) Endothelial cell monolayers on 6, 14, and 29 kPa substrates were treated with 1 μM PMA for 5 minutes. PMA treatment effect was significant by two-way ANOVA ($p<0.001$), but substrate stiffness effect was not significant. $\#p<0.05$ by post-hoc Tukey-Kramer test compared to untreated.

ROS production is known to induce actin fiber formation in endothelial cells [199]. To see if substrate-dependent ROS production increased actin fiber formation, PMA-stimulated cells on substrates of increasing stiffness were labeled for actin. In untreated samples, peripheral actin fibers were observed in cells on all substrates, but were particularly pronounced in cells on the softest 6 kPa gels (Figure 4.5). Following 15 minutes of PMA treatment, no noticeable changes in actin structure were observed. Following 30 minutes of PMA treatment, peripheral actin was still observed with some longitudinal stress fiber formation. On 14 kPa gels, stress fiber formation was more prominent, and on 29 kPa the cells displayed pronounced stress fibers with minimal peripheral actin. In summary, PMA induced greater longitudinal actin fiber formation and peripheral actin loss in cells on stiff substrates.

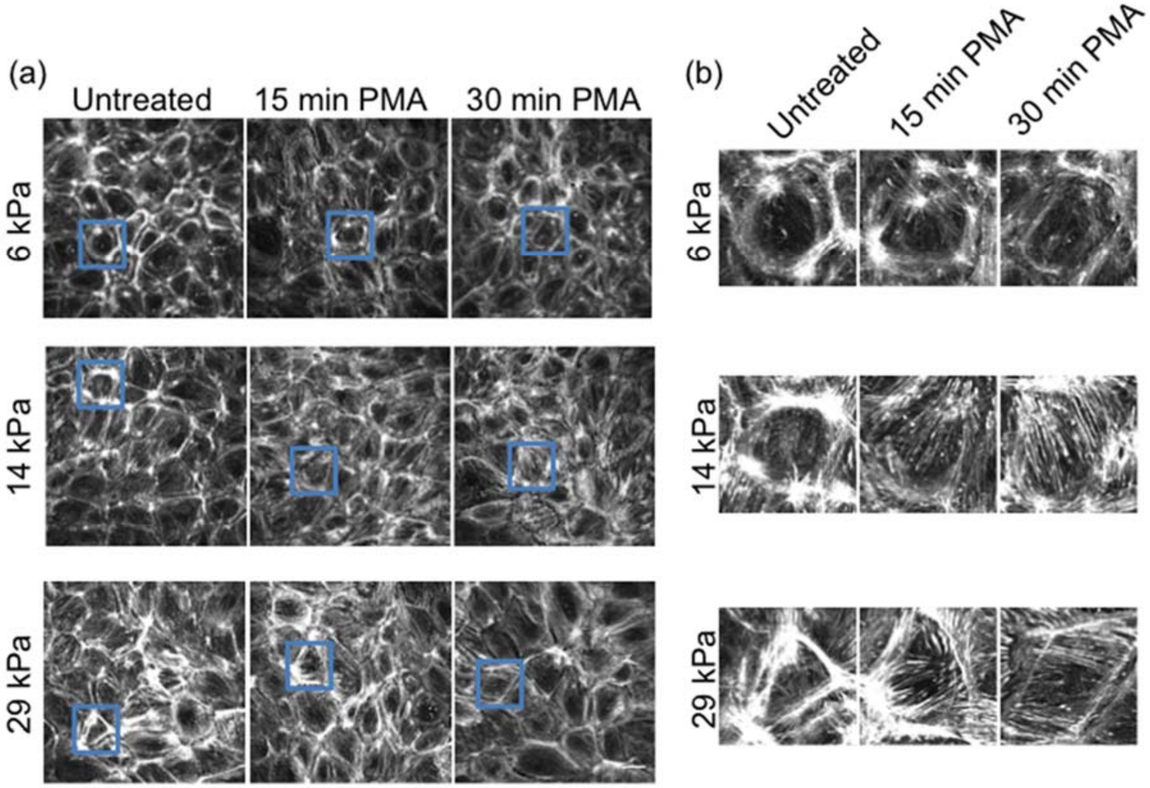

Figure 4.5. Actin stress fiber formation was greater on 29 kPa substrates following PMA treatment. (a) PAEC monolayers on 6, 14, or 29 kPa gels were untreated or treated with 1 μM PMA for 15 or 30 minutes prior to fixation and immunofluorescent labeling of actin using rhodamine phalloidin. Areas highlighted by rectangular regions are magnified in (b) to highlight differences in morphology. Images are compressed confocal z-stacks of endothelial monolayers imaged at 60X. Scale bar is 25 μm.

To determine whether ROS-induced actin stress fiber formation was associated with increased actinomyosin contraction in our cells, PAECs were labeled for phosphorylated myosin light chain (pMLC), followed by image quantification. For the positive control (10 U/mL thrombin for 30 minutes), cells on 29 kPa substrates localized pMLC along actin fibers (Figure 4.6a) and increased overall pMLC approximately 14-fold (Figure 4.6b). 1 µM PMA treatment for 15 or 30 minutes did not induce pMLC translocation to actin fibers or increase overall pMLC labeling. These results indicated that the changes in actin fiber organization did not coincide with increased substrate-dependent actinomyosin contractility at the time points tested. Therefore, any cell-cell junction loss observed was related to ROS-induced signaling.

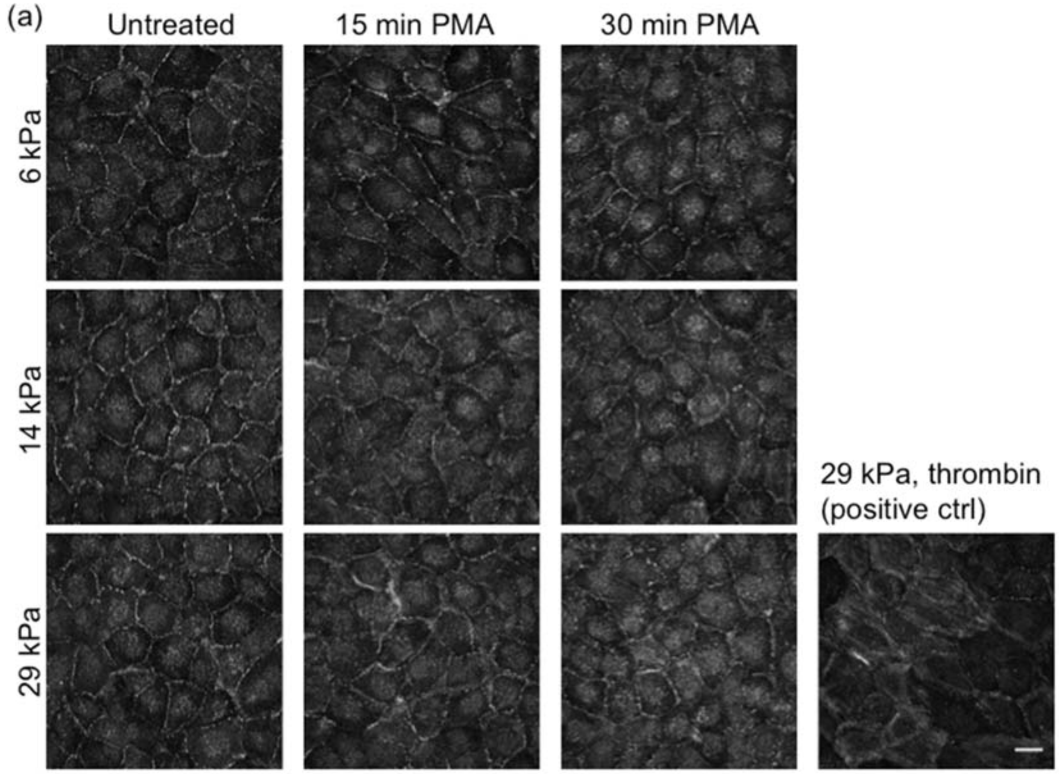

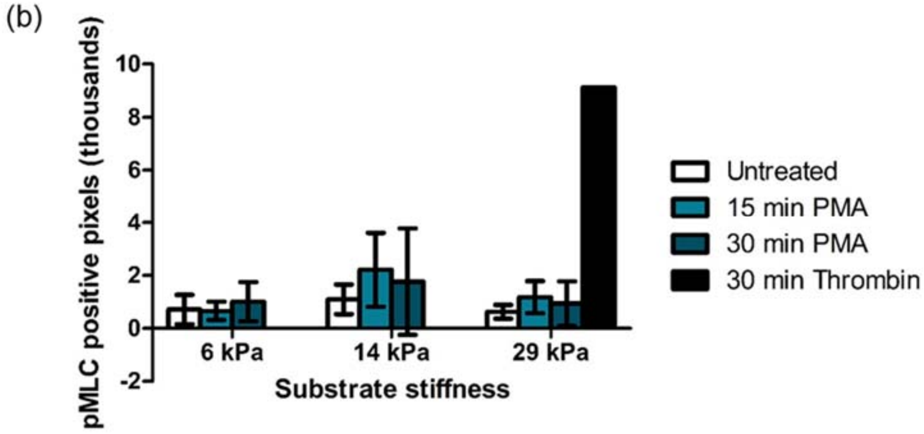

Figure 4.6. PMA treatment did not increase pMLC in endothelial monolayers on substrates of varying stiffness. (a) PAEC monolayers on 6, 14, or 29 kPa gels were untreated or treated with 1 µM PMA for 15 or 30 minutes, prior to fixation and immunofluorescent labeling of phosphorylated myosin light chain (pMLC). For the positive control, cells on a 29 kPa gel were treated with 10 U/mL thrombin for 30 minutes. Images are compressed confocal z-stacks of endothelial monolayers imaged at 60X. Scale bar is 25 µm. (b) Number of pixels positive for pMLC was quantified using custom Matlab image processing code. The effects of stiffness and PMA treatment were not significant when assessed by n-way ANOVA.

4.3.3. ROS-mediated substrate-dependent changes in adherens junction morphology in response to PMA

Increased ROS induces cell-cell junction loss, which has been attributed in part to cell-cell junction protein phosphorylation and internalization [206, 341, 342]. We next tested the hypothesis that substrate stiffening worsens ROS-mediated adherens junction loss in response to PMA. In untreated cells on all substrates, areas of wide reticular adherens junctions were visible between adjacent cells (Figure 4.7). After 15 minutes of PMA treatment, reticular junctions were mostly maintained in cells on the 6 kPa substrate whereas some reticular junction structure loss was observed in cells on the 29 kPa substrate. Following PMA exposure for 30 minutes, wide reticular junctions were maintained in cells on the 6 kPa substrate (indicating little junction loss) and to a lesser extent in cells on the 14 kPa substrate. On the stiffest 29 kPa substrate, nearly all junctions lost their reticular structures with some junctions appearing wavy or disrupted. These results demonstrate that endothelial reticular junction structure loss is exacerbated by stiffer substrates in response to the ROS stimulant PMA.

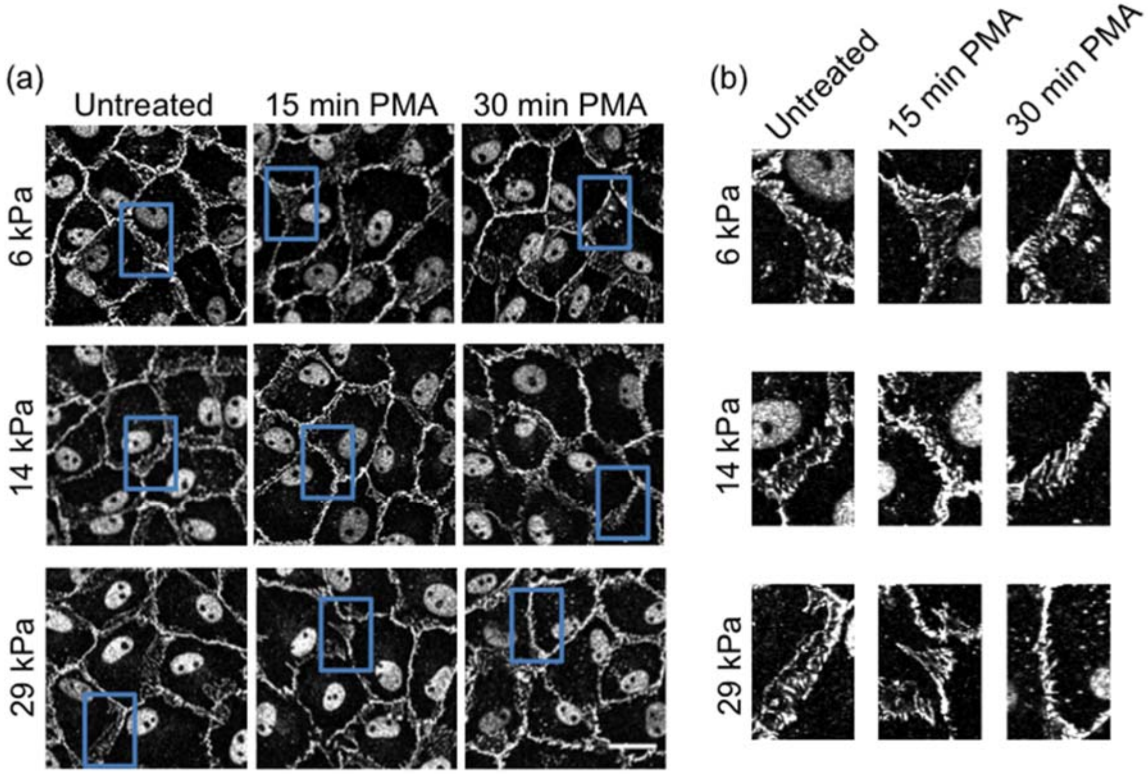

Figure 4.7. Reticular adherens junction loss was greater in endothelial cell monolayers on stiffer substrates following PMA treatment. PAEC monolayers on 6, 14, or 29 kPa gels were untreated or treated with 1 μM PMA for 15 or 30 minutes, prior to fixation and immunofluorescent labeling of the cell-cell junction protein β-catenin. Areas highlighted by rectangular regions are magnified in (b) to highlight differences in morphology. Images are magnified subsets of compressed confocal z-stacks of endothelial monolayers imaged at 60X. Scale bar is 25 μm.

To confirm that ROS led to PMA-induced junction loss, ROS scavengers were administered prior to PMA treatment. ROS scavengers were applied to cells on glass coverslips, instead of gel substrates, because junction loss following PMA exposure was most extreme in cells on glass; thus, the effect of scavenger pre-treatment on PMA-induced morphological changes was most evident in cells on coverslips. ROS scavengers themselves did not affect cell-cell junction structure, since samples treated with ROS scavengers alone still exhibited reticular junctions. Cells treated with PMA along showed wavy and invaginated junctions (indicating junction loss); this PMA-induced change in junction morphology was prevented by ROS scavengers (Figure 4.8a, b). More strikingly, ROS scavengers prevented PMA-induced actin reorganization (Figure 4.8c). In untreated cells and cells treated with the ROS scavengers, peripheral actin bands were observed. In PMA-treated cells, peripheral actin was lost and actin stress fibers were prominent. In PMA-treated cells with ROS scavengers, peripheral actin fibers were maintained. Thus ROS production appeared to be responsible for PMA-induced reticular junction loss and actin fiber formation.

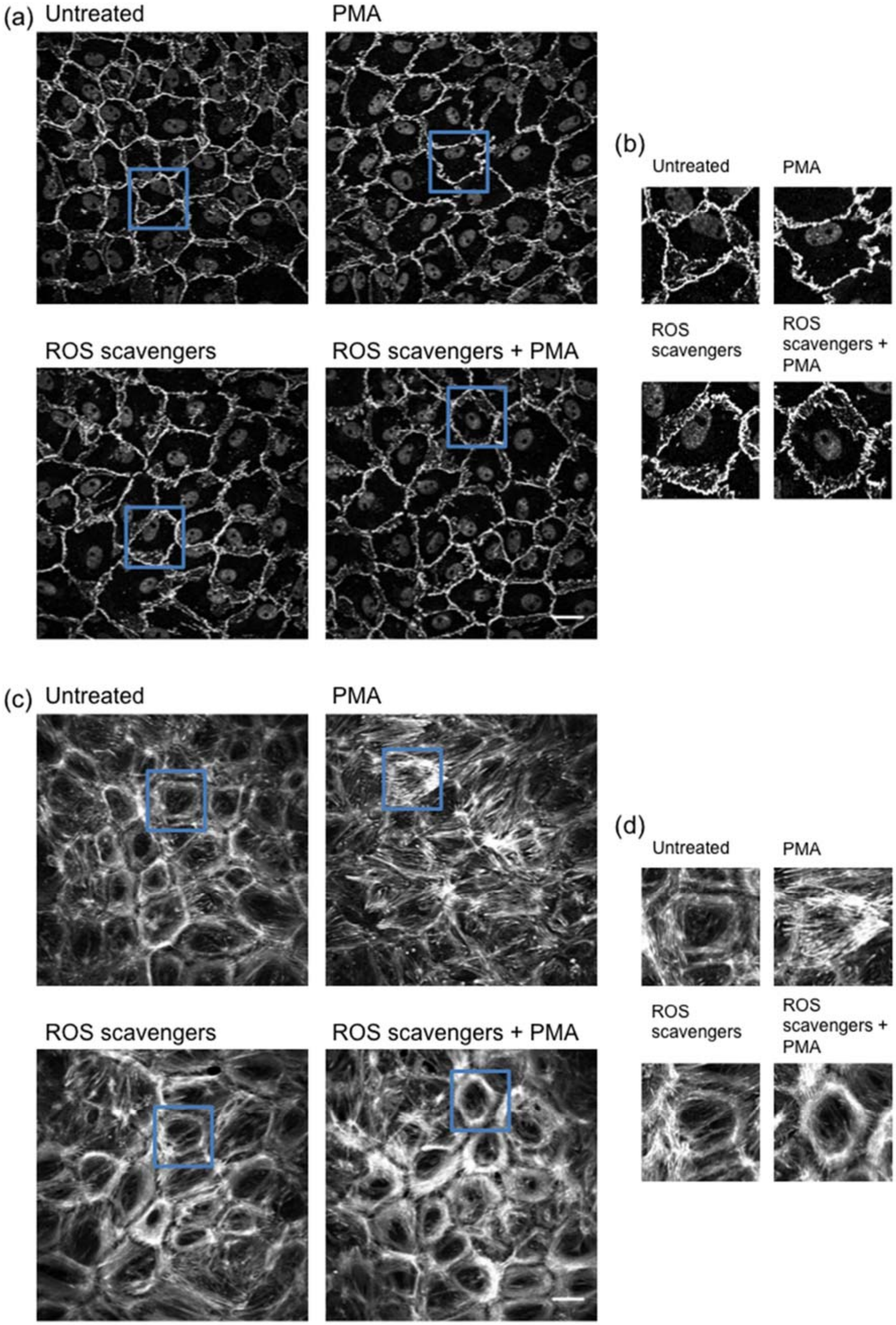
(a)
Untreated
PMA
ROS scavengers
ROS scavengers + PMA
(b)
Untreated
PMA
ROS scavengers
ROS scavengers + PMA
(c)
Untreated
PMA
ROS scavengers
ROS scavengers + PMA
(d)
Untreated
PMA
ROS scavengers
ROS scavengers + PMA

Figure 4.8. ROS scavengers prevented PMA-induced adherens junction loss and actin fiber redistribution in endothelial cells on collagen-coated glass coverslips. Endothelial cell monolayers were pre-treated with or without ROS scavengers (4 mM N-acetyl cysteine, 50 mM sodium pyruvate) for 1 hour, prior treatment with or without 1 μM PMA for 30 minutes. (a) Samples were fixed and immunofluorescently labeled for β-catenin, with individual representative cells magnified in (b); immunofluorescently labeled for actin (rhodamine phalloidin, c). Areas highlighted by rectangular regions are magnified in (d) to highlight differences in morphology. Images are compressed confocal z-stacks of endothelial monolayers imaged at 60X. Scale bar is 25 μm.

4.3.4. PMA-induced actin reorganization in the abdominal aortic endothelium of wild type and elastin haploinsufficient mice

To investigate the relevance of our *in vitro* observations to endothelial response *in vivo*, aortic segments from wild type (WT) and elastin haploinsufficient (ELN+/-) mice were exposed to PMA in an *ex vivo* cannulated system. The endothelium from the WT mouse exhibited few actin fibers (Figure 4.9). Peripheral actin fibers were slightly more prominent in the untreated ELN+/- aortic endothelium. With PMA treatment (5 μM, 30 minutes), peripheral actin was observed in the WT aortic endothelium and to a much greater extent in the ELN+/- aortic endothelium.

When VE-cadherin (green) and actin (red) images were merged (Figure 4.9), in the WT mouse aorta most peripheral actin was co-localized with VE-cadherin (indicated by yellow) following *ex vivo* PMA treatment. In the PMA-treated aortic segment from the ELN+/- mouse, more peripheral actin but less VE-cadherin labeling was observed (indicated by less yellow and more red). These merged images highlight the PMA-induced actin fiber formation differences between the two genotypes. Interestingly, little to no longitudinal actin stress fibers were observed, as are frequently observed *in vitro*.

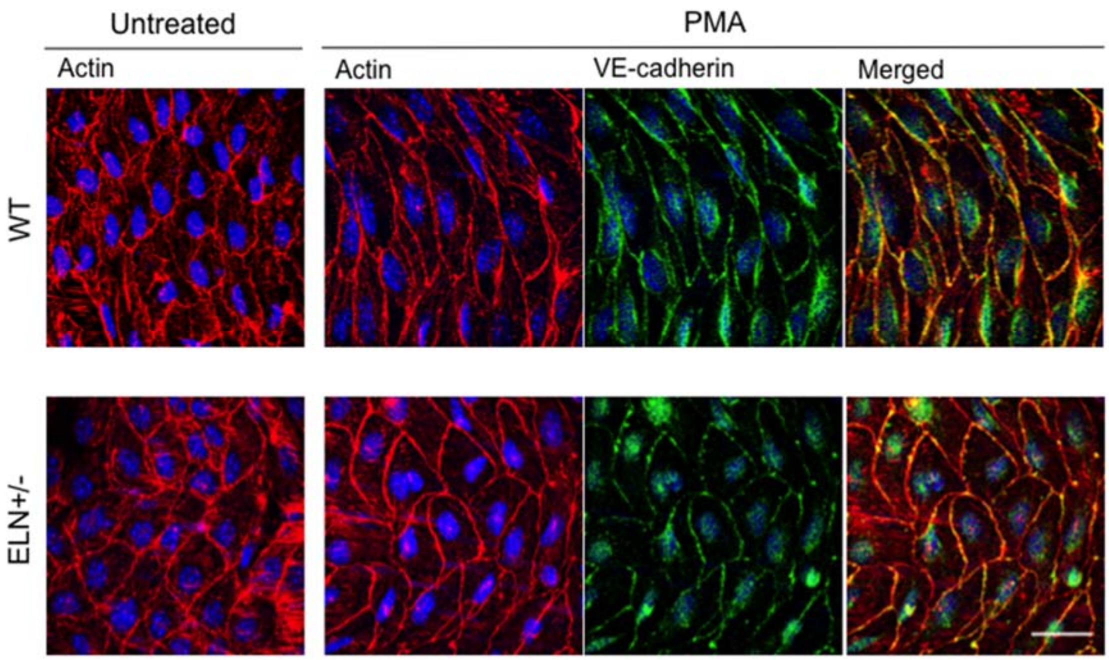

Figure 4.9. Peripheral actin fiber formation was greater in stiffer (ELN+/-) vessels in response to PMA. Abdominal aorta from WT or ELN+/- mice were either fixed without treatment (left) or treated with 5 μM PMA for 30 minutes and fixed (middle), prior to labeling actin (rhodamine phalloidin). Images on the right show both actin (red) and VE-cadherin (green), with areas of colocalization (yellow). The endothelium of intact aortae were imaged en face by confocal microscopy with 0.5 μM step size. Confocal z-stacks were compressed. Scale bar is 25 μm.

4.4. Discussion

In this chapter we demonstrated that substrate stiffening exacerbated ROS production in cultured endothelial cells in response to PMA. PMA-induced stress fiber formation was greater on stiff substrates, but stress fiber formation was not associated with increased myosin phosphorylation, suggesting that PMA did not elicit cell contractility. PKC activation was consistent among substrates, which indicated that substrate-dependent responses to PMA were not PKC dependent. Cells on stiffer substrates exhibited increased cell-cell junction loss in response to PMA, which was prevented through pre-treatment with ROS scavengers. Lastly, stiffer aortas from ELN+/- mice showed increased peripheral actin fiber formation in response to PMA.

4.4.1. Proposed mechanism

Figure 4.10 presents a potential mechanism for how PMA stimulates more ROS production in endothelial cells on stiff substrates. Since integrin activation is low on softer substrates (Figure 4.10a), Rac1 activity is maintained at a low level. Since Rac1 is essential to NADPH oxidase assembly at the cell membrane, basal NADPH oxidase activity is low on soft substrates. On stiffer substrates, integrin activation is increased, enabling greater Rac1 activation and increased NADPH oxidase complex formation (Figure 4.10b). When PMA binds and activates PKC, which initiates NADPH oxidase assembly through the phosphorylation of NADPH oxidase sub-units, the low Rac1 activity in cells on soft substrates results in minimal ROS production (Figure 4.10c). PMA stimulation of cells on stiff substrates (Figure 4.10d) results in increased ROS production through increased integrin-dependent Rac1 activation. Elevated ROS production on stiff substrates results in actin stress fiber formation and adherens junction proteins phosphorylation, which results in cell-cell junction loss [205].

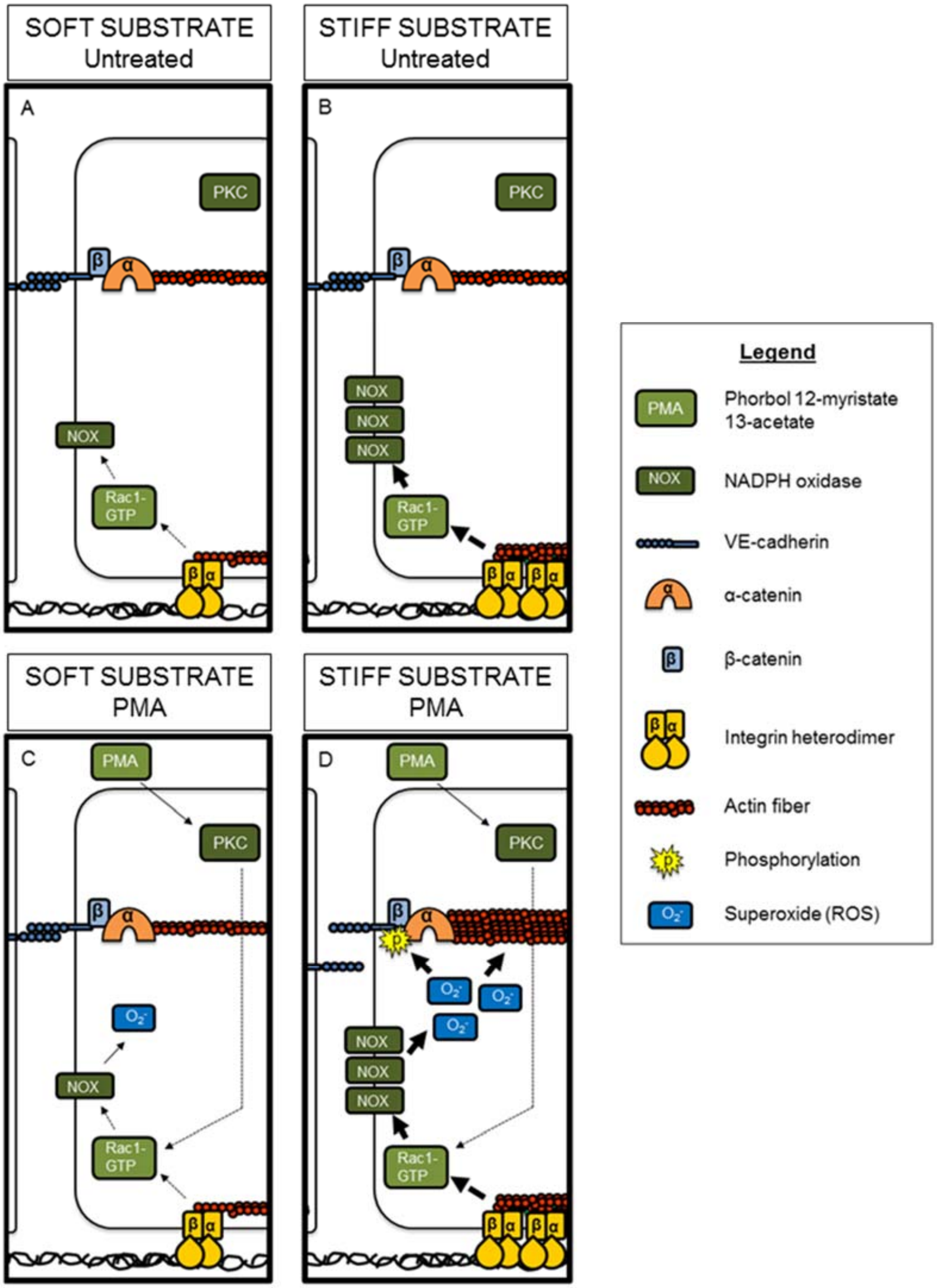

Figure 4.10. Proposed mechanism for substrate-dependent ROS-mediated cell-cell junction loss. (a) On soft substrates in untreated samples, integrin-dependent Rac1 activity and NADPH oxidase (NOX) localization to the membrane are low. (b) On stiff substrates in untreated samples, integrin-dependent Rac1 activity and NOX localization to the membrane are increased. (c) In PMA-treated cells on soft substrates, superoxide production is minimal due to low levels of NOX assembled at the cell membrane. (d) In PMA-treated cells on stiff substrates, superoxide production is elevated due to increased integrin-dependent NOX at the membrane.

4.4.2. Broader cardiovascular implications: alternative effects of endothelial superoxide and superoxide production by non-endothelial cell types

The goal of this work was to study substrate-dependent ROS-mediated endothelial cell-cell junction loss. However, ROS also leads to other adverse effects on the endothelium. Specifically, superoxide interacts with nitric oxide (NO) to form peroxynitrite ($ONOO^-$). This interaction effectively decreases the availability of NO, which is needed for vasodilation [46, 343]. Secondly, superoxide can decrease NO production through eNOS uncoupling. Under normal conditions, eNOS converts L-arginine and molecular oxygen to NO and citrulline [344]. This reaction requires several co-factors, including tetrahydrobiopterin (BH_4). eNOS uncoupling can occur when BH_4 is oxidized by superoxide and therefore is not available [345, 346]. Uncoupled eNOS produces superoxide (O_2^-) instead of NO [347]. eNOS uncoupling represents just one example of how $ONOO^-$ causes cardiovascular damage; in fact, protein nitration by $ONOO^-$ has been widely observed in a variety of cardiovascular diseases [348]. Thus, if vessel stiffness exacerbates endothelial ROS production as this work proposes, the damaging effects would go beyond endothelial barrier function.

While this study focused on endothelial-derived ROS, superoxide is also produced in other cardiovascular cell types [194]. For example, cardiomyocytes produce superoxide via NADPH oxidase. Increased superoxide was associated with heart failure; interestingly, while cardiomyocytes in non-failing and end-stage failing hearts expressed comparable NADPH oxidase sub-unit levels, p47phox membrane localization increased in failing hearts [349]. Vascular smooth muscle cells also produce ROS. In a mouse model of atherosclerosis (ApoE-/-), NADPH oxidase sub-unit p47phox knockdown resulted in decreased smooth muscle cell superoxide production and decreased total lesion area [350]. Based on superoxide and oxidized low density lipoprotein (ox-LDL) co-localization in human atherectomy samples (excised atherosclerotic plaques), ROS produced by smooth muscle cells and fibroblasts may further oxidate ox-LDL, a component of atherosclerotic lesions [351, 352]. If the effect of increased vessel stiffness on ROS production extends to vascular smooth muscle cells and cardiomyocytes, the harmful effects of oxidative stress could be amplified.

4.4.3. ROS as a therapeutic target

Oxidative stress, created through a combination of ROS overproduction and inadequate ROS inactivation, has been implicated in a variety of cardiovascular diseases; specifically, the enzyme responsible for superoxide production (NADPH oxidase) has been identified as a therapeutic target for atherosclerosis [352, 353]. However antioxidants, such as vitamin E, have shown inconsistent success in preventing cardiovascular events or improving cardiovascular function in human clinical studies. A variety of reasons behind the lackluster clinical trial results have been provided. For one, relatively low ROS levels are necessary for normal cellular functions; thus, treatments resulting in severe reduction of ROS below normal levels could be harmful. Screening of study participants for oxidative stress biomarkers has been suggested as a way of improving study results [354].

If follow-up studies confirm that increased arterial stiffness exacerbates ROS production *in vivo*, non-invasive patient screening for arterial stiffness by pulse wave velocity (PWV) could be used in conjunction with oxidative stress biomarker screening to determine the best treatment option. In elderly patients, increased arterial stiffness was strongly correlated with multiple indicators of atherosclerosis (carotid intima-media thickness, and severity of carotid and aortic plaques) [355]. In patients undergoing coronary angiography, increased superoxide production by activated neutrophils positively correlated with measurements of arterial stiffening (augmentation index and pulse pressure amplification [356]. However, to our knowledge, there has been limited investigation of the correlation between arterial stiffening and endothelial superoxide production in humans.

4.4.4. Limitations

While our work shows that PMA-induced ROS production increases with substrate stiffness, our research is not without limitations. Phorbol esters, including PMA, are found in certain plants and can cause toxicity in animals when consumed [357]. Yet the physiological relevance of endothelial response to PMA is questionable; it is not involved in the pathogenesis of any cardiovascular diseases. We chose to use PMA because it useful in isolating the effect of ROS production, as it elicits ROS-mediated cell-cell junction loss without inducing cell contractility [144, 207].

Most data presented in this chapter were from *in vitro* studies of endothelial cells on polyacrylamide gel substrates. In this *in vitro* system, cells were not exposed to shear stress or strain as they would normally experience *in vivo*. *En face* images of actin in mouse aortic endothelium were presented; however, superoxide was not detected in intact vessels under physiological conditions. Superoxide detection in vessels could better directly demonstrate increased ROS production in stiffened vessels and its effect on the observed actin reorganization.

Next, there were some limitations in the methods presented in this chapter. The dye used for ROS detection (CM-H2DCFDA) is transformed to its fluorescent form by a variety of different ROS, and as such is a general oxidative stress indicator—not specific to superoxide [358]. Since substrates stiffness-dependent ROS production has not been previously demonstrated, a general ROS dye was chosen to increase the chance of observing an effect. In future studies, an indicator specific to superoxide such as dihydroethidium, could be used to support the hypothesis that integrin activation enhances superoxide production by NADPH oxidase [359]. Lastly, immunofluorescent labeling of pMLC was used as an indirect measure of contractility. Other direct measures, such as traction force microscopy, could be used to assess cell contractility. However, pMLC labeling is specific for actinomyosin contraction and is widely accepted in the literature as an indicator of contractility.

Despite these limitations, this work illustrates a novel potential mechanism for substrate-enhanced ROS production in the endothelium; further study of the interaction between arterial stiffness and ROS holds the potential for improving therapies to prevent or ameliorate endothelial barrier dysfunction.

5. Conclusions and future work

5.1. Thesis summary

Cardiovascular diseases represent a major risk to global health, contributing to approximately one-third of all deaths worldwide [360]. Although cardiovascular diseases are diverse and develop in response to many different factors, arterial stiffening is becoming more widely recognized as a major risk factor. Increased arterial stiffness is correlated with cardiovascular mortality, coronary heart disease, and stroke [9]. Inflammation plays a role in many cardiovascular diseases, including atherosclerosis and hypertension [27, 361]; however, little is known about the combined impact of arterial stiffening and inflammation on endothelial dysfunction—specifically endothelial cell stiffening and endothelial barrier loss.

I demonstrated that dielectrophoresis can be used to detect changes in single attached endothelial cell deformability using a novel inverted quadrupole device. I further showed that vinculin localization to cell-cell junctions increased in the stiffened abdominal aorta of ELN+/- mice. I demonstrated that vinculin also localized to cell-cell junctions *in vitro* when intracellular tension was increased following exposure to inflammatory cytokines TNF-α and thrombin. This effect was enhanced on stiff substrates and was prevented through blocking the cell contractility pathway. In addition, I found that substrate stiffness modulated cell stiffening in response to TNF-α, which could impact nitric oxide production. Lastly, I investigated how substrate stiffness modulates endothelial reactive oxygen species (ROS) production. ROS-mediated cell-cell junction loss was increased on stiff substrates concomitant with actin fiber formation, but was independent of cell contractility.

Taken collectively, these data contribute to our understanding of how arterial stiffening exacerbates endothelial response to inflammation (through increased contractility and ROS production). This study also supports recent reports that vinculin localization to junctions is protective against cell-cell junction opening, a mechanism which could be potentially utilized for therapeutic interventions again endothelial barrier loss [178].

5.2. Specific discoveries

The over-arching objective of this work was to investigate how arterial stiffening influenced endothelial cell stiffening (which affects nitric oxide production) and endothelial barrier function in response to systemic inflammation. This goal was achieved through a combination of *in vitro* single cell and monolayer studies and *ex vivo* mouse aorta studies.

In Chapter 2, I presented the simulation, microfabrication, and validation of an inverted quadrupole dielectrophoretic (DEP) device for measuring single attached cell deformability, which reflects cell stiffness. I demonstrated that cell deformability in the DEP device corresponded to atomic force microscopy measurements, the gold standard for assessing cell stiffness. Differences in cell deformability were demonstrated between endothelial cells with or without cytoskeletal disruption by cytochalasin D and between transformed and untransformed mammary epithelial cells.

In Chapter 3, I demonstrated that aortic sub-endothelial stiffness was increased in genetically modified elastin haploinsufficient (ELN+/-) mice. Vinculin co-localization with VE-cadherin at endothelial cell-cell junctions in intact aortic sections correlated with sub-endothelial stiffness; vinculin was observed at cell-cell junctions in all segments, but was decreased in the softest segment (abdominal aorta of wild type mice). *In vitro*, substrate stiffening enhanced ROCK-dependent myosin phosphorylation, actin fiber formation, and vinculin co-localization with VE-cadherin following exposure of endothelial cell monolayers to TNF-α and thrombin. Substrate stiffness exacerbated thrombin-induced, but not TNF-α-induced, monolayer permeability *in vitro*. Cells on stiff 50 kPa substrates initially stiffened and then softened following TNF-α exposure, while cells on soft 6 kPa substrates softened and remained soft.

In Chapter 4, I demonstrated that substrate stiffening enhanced ROS production in endothelial monolayers in response to the PKC activator phorbol 12-myristate 13-acetate (PMA). PMA did not promote increased myosin phosphorylation at the times tested, but did induce enhanced reticular adherens junction loss and actin stress fiber formation on stiff substrates. PMA-induced junction loss and stress fiber formation were prevented by pre-treatment with ROS scavengers.

5.3. Contributions to the field

This thesis contributes to a wide variety of disciplines within the field of cell mechanobiology. The areas of contribution range from cell mechanics device development to comparisons of endothelial function *in vivo* and *ex vivo* to mechanisms underlying substrate-dependent cell-cell junction loss. The ways in which this thesis relates to the broader field of cell mechanobiology are detailed below.

5.3.1. Dielectrophoretic device

First, the dielectrophoretic (DEP) device presented in Chapter 2 represents a novel method for applying forces to attached single cells in order to access global deformability. Currently no other non-contact device is capable of deforming attached single cells. Optical stretchers are effective at deforming cells in suspension [279]; yet nearly all cell types are adhered within a tissue *in vivo*, and substrate attachment modifies cell stiffness. Specifically, integrin activation modulates both RhoA and Rac activity, which regulate actin polymerization [362]. As fibroblasts in suspension attached to fibronectin-coated surfaces, Rho activity decreased within the first 30 minutes, then increased [363]. Recently published results suggest that integrin engagement influences cell stiffness in cells that are attached but not yet spread; passivation of the attachment surface with bovine serum albumin decreased epithelial cell stiffness compared to cells attached to a non-passivated surface for 10 minutes [364]. Considering the importance of integrin activation in cell stiffness, the ability of our device to measure attached cell deformability represents a significant contribution to the field of cell mechanobiology.

In addition, this device could be transformed into a high-throughput screening device through multiplexed electrodes. An electrode array would enable multiple simultaneous measurements, which would improve the capabilities of this device as a drug-screening instrument. Various stimuli, including biochemical (e.g. drug candidates) and biomechanical (e.g. shear stress), could be applied to arrays of single cells to determine their effect on cell deformability. Simultaneous use of fluorescent dyes (such as DAF-FM diacetate for nitric oxide or dihydroethidium for superoxide) with our device would provide data linking the stimuli of interest, cell deformability, and cell function.

Thus, the adaption of the DEP device to a multiplexed format would increase the number of measurements and the use of live-cell dyes would connect cell stiffness with cell function in a high-throughput device.

Moreover, the DEP device is moveable through the use of a micromanipulator and could therefore be adapted to serve even broader purposes, such as the accurate positioning or isolation of cells in suspension. Isolating specific single cells in suspension could improve the establishment of stably transfected cell lines; transfected cells expressing fluorescent markers could be identified by fluorescence microscopy and selected using this DEP device [365]. DEP tweezers have been recently used to isolate fluorescent cells [287]. However, fabrication of the tweezers is more complicated than fabrication of our device, which is based on photolithography, a technique now widely implemented in academic laboratories.

5.3.2. Sub-endothelial stiffness in contractility-dependent endothelial monolayer barrier function and cell stiffness

Our data also show that elastin haploinsufficient (ELN+/-) animals can be used to measure the effects of arterial stiffening. Recent clinical data supporting arterial stiffening as a cardiovascular risk factor has promoted interest in animal models to study the repercussions of increased vessel stiffness [366]. Since arterial stiffness increases with age due to elastin degradation, aged animals have been used to study how the loss of vessel elasticity affects endothelial barrier function [134, 367]. However, using aged animals is problematic since long lead times are necessary to allow for the aging process to occur. Elastin haploinsufficient (ELN+/-) animals represent a more time-efficient model of arterial stiffening. This work reports, for the first time, that aortic sub-endothelial stiffness is increased in ELN+/- mice. This characterization is an important contribution to the field because it establishes this animal model as a viable alternative to using aged animals.

This work contributes to vascular biology through highlighting differences between cultured primary endothelial cells *in vitro* and endothelial cells within an intact aorta *ex vivo*. Few published studies compare and contrast immunofluorescent labeling of intact endothelium and cultured endothelial cells [145, 368-370]. While imaging of cultured primary endothelial cells provides a convenient way of observing changes in cell morphology in response to particular stimuli, the morphological changes of the endothelium *in vivo* or *ex vivo* may differ in key aspects. As one example, the actin cytoskeleton is considerably more pronounced in cultured endothelial cells compared to intact endothelium. Thus this study supports the need for *ex vivo* imaging of vessels through highlighting these differences.

Another important contribution of this work is in improving our understanding of vinculin's role in bolstering cell-cell junctions under tension. The fact that tension-dependent unraveling of α-catenin enables binding of vinculin to cell-cell adhesions is well established [175]. Relatively recent work demonstrated that vinculin localization to endothelial adherens junctions provided reinforcement against junction opening, and similar work in epithelial cells supports this conclusion [178, 311]. This thesis reports, for the first time, that vinculin recruitment to junctions is enhanced on stiff substrates following exposure to contractility-inducing agents (TNF-α, thrombin). Therapeutic interventions that enhance vinculin's ability to support cell-cell junctions could take advantage of this naturally occurring protective system; such therapies could prevent or decrease endothelial barrier loss in response to systemic inflammation, which plays a role in a variety of diseases including atherosclerosis, hypertension, rheutamoid arthritis, and sepsis.

This work enhances the understanding of the effects of substrate stiffness on endothelial monolayers. Initial work into substrate-dependent endothelial responses focused on single cells, which spread to a greater extent on stiff substrates compared to soft substrates. A study by Yeung et al from 2005 demonstrated that the circumference of single bovine aortic endothelial cells increased on PA gel substrates of increasing stiffness between 0.2 and 10 kPa; this study also showed by phase contrast microscopy that substrate stiffness did not appear to influence cell shape or size of endothelial cells within a confluent monolayer [74]. More recent studies have investigated the role of substrate in endothelial monolayers. For example, *in vitro* neutrophil transmigration through HUVEC monolayers was enhanced with substrate stiffening (0.42 to 280 kPa) through an MLCK-dependent mechanism [80]. Another study demonstrated that ROCK-mediated endothelial permeability and leukocyte transmigration through BAEC monolayers was higher on stiffer substrates [134]. However, these previous reports did not detail the effects of substrate stiffness on inflammation-induced cell-cell junction tension, as was included in our study. Thus, in addition to contributing evidence that substrate stiffness affects endothelial monolayers, this work deepens our understanding of substrate-dependent changes in junction composition.

5.3.3. Sub-endothelial stiffness in endothelial production of ROS

The role of substrate stiffness in ROS production has been demonstrated in epithelial cells, but not endothelial cells [215]. This work reports for the first time that endothelial cell monolayers on stiff substrates produce more reactive oxygen species in response to the PKC-activator PMA. While PMA is not produced in the human body, PKC activation is implicated in a variety of conditions, including endothelial barrier loss and hyperglycemia [371, 372]. If the proposed model for enhanced ROS production through increased integrin activation is confirmed *in vivo*, the implications would be wide-ranging. Tissue stiffening could potentially exacerbate the effects of any stimulus that elicits NOX-dependent superoxide production.

Improved understanding of the mechanisms underlying ROS production could impact the understanding of other diseases beyond atherosclerosis. Decreased NO-mediated vasodilation in a diabetic mouse model was attributed to increased endothelial superoxide production [373]. In addition, ROS are known to play a role in sepsis, although the vascular tissue that most contributes to septic ROS production is less clear (i.e. endothelium, smooth muscle cells, immune cells, etc.) [189, 374]. If environmental stiffness enhances ROS production in tumors, our results could have implications beyond vascular diseases. Heightened ROS has been observed in tumors, which are often stiffer than surrounding tissue [61, 375]. In fact, extracellular matrix cross-linking has been suggested to increase integrin signaling in breast cancer [60]. Since oxidative stress has been implicated in several diseases, this research on the crosstalk between tissue stiffness and ROS production could contribute to the discovery of novel therapeutic targets.

5.3.4. Clinical implications

More broadly speaking, this work supports the importance of clinical arterial stiffness screening combined with screening for system inflammation. Pulse wave velocity enables simple, non-invasive measurement of arterial stiffness. Such screening could be useful in patients at increased risk of cardiovascular disease, such as those with a family history or those being treated for a disease known to cause vascular complications, such as diabetes or rheumatoid arthritis. Since studies show that arterial stiffening precedes the development of hypertension, a major risk factor for atherosclerosis, early PWV screening of patients at risk for cardiovascular diseases could alert patients of the need to adjust diet and exercise choices. In addition, use of PWV screening in conjunction with screening for inflammation (by measuring blood levels of inflammatory markers such as TNF-α, C-reactive protein, and IL-6) could inform doctors on the best course of treatment. For example, individuals showing evidence of arterial stiffening could be good candidates for anti-TNF-α therapies, such as etanercept [376].

This work also provides evidence for a connection between arterial stiffness and ROS production and suggests a need to better understand the clinical impact of arterial stiffening on oxidative stress. Animal studies suggest cross-talk between arterial stiffening and ROS; in ELN+/- mice, both knockdown of the NADPH oxidase sub-unit p47phox and pharmacological treatment with the NADPH oxidase inhibitor apocynin were successful in reducing mean arterial pressure at 16 weeks of age [377]. In humans with elastin insufficiency (Williams-Beuren syndrome), a deletion in the gene that encodes p47phox (*NCF1*) correlated with a decreased occurrence of hypertension [378]. While anti-oxidant therapies have had inconsistent success at improving cardiovascular function in the clinic, such therapies may be more effective in individuals with increased arterial stiffness. It is possible to assess markers of superoxide production in the blood [356]; concurrent PWV and oxidative stress screening may provide improved diagnosis and treatment decisions to prevent endothelial dysfunction.

5.4. Future studies

5.4.1. Protective function of vinculin in the endothelium

Further investigation is necessary to better understand the protective role of vinculin against substrate-dependent contractility-induced cell-cell junction opening. Our studies showed that cell contractility increased with increasing substrate stiffness; however, the increase in functional endothelial permeability with increasing substrate stiffness was subtle. One possible reason for this disconnect between induced cell contractility and permeability could be that vinculin recruitment following increased intracellular tension protected against cell-cell junction opening. In fact, other recently published results support the protective properties of vinculin in age-related cardiomyocyte remodeling [313].

Future work would focus on better understanding the point at which this protective function is overwhelmed by intracellular forces. Recently published *in vitro* studies which applied increasing force to purified proteins using magnetic tweezers reported that vinculin dissociated from α-catenin at forces > 30 pN [174]. Future experiments using cultured endothelial monolayers on PA gel substrates could investigate the forces needed to break the vinculin-α-catenin association within cells. Traction force microscopy used in conjunction with cells expressing fluorescently tagged vinculin could connect the magnitude of cell-generated forces and the localization of vinculin to cell-cell junctions. Fluorescence microscopy images taken at increasing intervals following the application of a contractility stimulus could determine traction forces and cell-cell junction morphology at each time.

The elastin haploinsufficient mouse model could be used in future studies to better understand the role of vinculin in endothelial cell-cell junction maintenance *in vivo*. Specifically, vinculin could be over-expressed in ELN+/- mice to test the protective capacity of vinculin. Vessel permeability studies could be used to assess the effect of increased vinculin on basal vessel permeability and permeability following the stimulation of systemic inflammation. In addition to measuring functional endothelial barrier function, *en face* imaging of the endothelium would be required to determine if vinculin was associating with focal adhesions, cell-cell junctions, or both.

In long-term future studies, strategies to enhance the interaction between vinculin and α-catenin with the goal of eventually pharmacologically improving endothelial barrier function *in vivo* would be of key interest. Better understanding this interaction could provide new therapeutic strategies for strengthening endothelial barrier function, which would contribute to the treatment of both atherosclerosis and potentially the prevention of cancer metastasis, as breaching the endothelial barrier is one key step in the spread of circulating tumor cells.

5.4.2. Role of substrate stiffness in VE-cadherin glycosylation

VE-cadherin, the endothelial-specific adherens junction protein, is key to cell-cell junction maintenance *in vitro* and *in vivo*. Interestingly, in whole cell lysate samples separated by SDS-PAGE and probed for VE-cadherin, we observed differences in the number of bands by Western blot depending on the cell substrate. When PAEC adhered to tissue culture polystyrene (plastic), one main band was observed around 105 kDa (Figure 5.1a, lane 4). However, two bands were observed in samples from PAEC on 6, 14, and 29 kPa PA gel substrates (Figure 5.1a, lanes 1-3). In the literature, Western blots of human, mouse, bovine and porcine endothelial cells show a single VE-cadherin band. When reported, the molecular weight of the single band was between 100 and 140 kDa [379-382]. However, the predicted molecular weight of VE-cadherin is ~90 kDa, based on its amino acid sequence [383]. The observation that the ratio between the top and bottom bands was substrate-dependent, as shown in Figure 5.1b, led to further investigation for possible causes and function implications.

Protein degradation is one possible cause for the appearance of multiple bands. Multiple bands have been reported when examining VE-cadherin in HUVEC lysates (~100 and 120 kDa); in this paper the authors referred to the 100 kDa band as a degradation product without further substantiation [203]. In a later paper from the same research group, double VE-cadherin bands were observed only in the TritonX-100-soluble fraction (protein not associated with the cytoskeleton); the lower molecular weight band (~100 kDa) was absent from the TritonX-100-insoluble fraction (protein associated with the cytoskeleton). In this paper, the lower molecular weight band was again referred to as a degradation product [384].

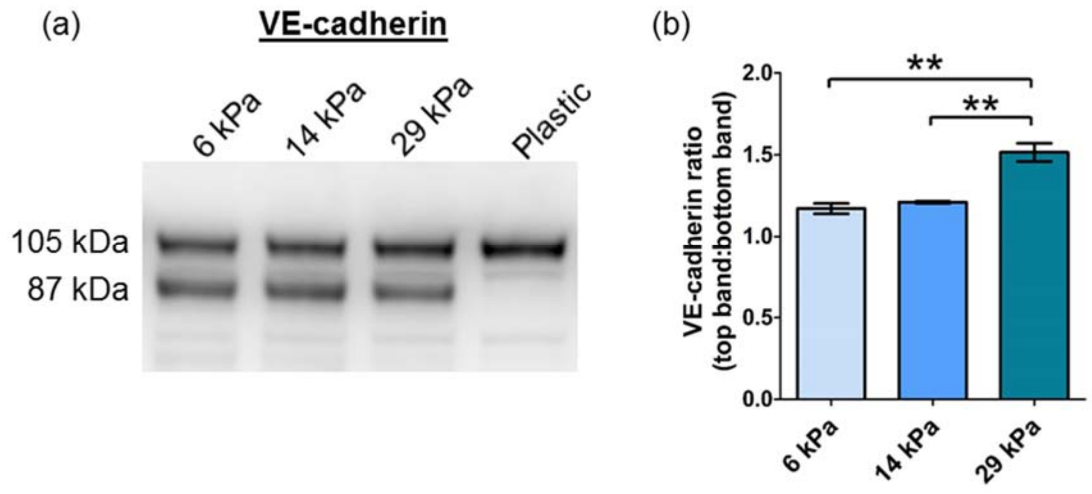

Figure 5.1. VE-cadherin molecular weight varied with substrate stiffness (a) Total VE-cadherin in confluent PAECs on 6, 14, or 29 kPa collagen-coated polyacrylamide gels or tissue culture polystyrene (plastic) was determined by Western blot (b) Higher and lower molecular weight bands in (a) were quantified. Effect of substrate stiffness on the ratio of the top and bottom bands was significant by one-way ANOVA ($p<0.01$). **$p<0.001$ by post-hoc Tukey-Kramer test.

Another possible cause of multiple bands is varying degrees of VE-cadherin glycosylation. VE-cadherin has seven extracellular glycosylation sites, and protein glycosylation can increase protein molecular weight [385]. Treating HUVECs with the enzyme peptide-N^4-(*N*-acetyl-β-glucosaminyl)asparagine amidase F (PNGase F) to remove extracellular glycans reduced the apparent molecular weight of VE-cadherin from 135 kDa to 90 kDa [383]. While it has been suggested that cell-cell junction protein glycosylation may modulate cell-cell interactions, few studies have directly investigated the functional implication on endothelial barrier function [386]. In HUVECs, removal of extracellular glycoproteins (specifically sialic acid) reduced homophilic interactions between the cell-cell junction protein platelet endothelial cell adhesion molecule (PECAM-1) [387]. Conversely, studies in epithelial cells have demonstrated that E-cadherin glycation resulted in unstable adherens junctions [388]. These reports suggest that VE-cadherin glycosylation may modulate endothelial barrier function, but more investigation is necessary to better understand the underlying mechanisms.

The preliminary data in Figure 5.1 point to a possible effect of substrate stiffness on VE-cadherin; future studies would first determine whether or not the differences in molecular weight are due to glycosylation through PNGase F treatment of PAECs on substrates of different stiffness. If the increased molecular weight of VE-cadherin in cells on stiff substrates is due to glycosylation and VE-cadherin glycosylation leads to unstable cell-cell junctions, these results suggest an alternative pathway contributing to increased endothelial monolayer permeability with substrate stiffening.

5.4.3. Further characterization of differences between the endothelia of wild type and elastin haploinsufficient mice

This thesis presents evidence that genetically modified elastin haploinsufficient (ELN+/-) mice have increased sub-endothelial stiffness. Thus, ELN+/- mice represent an interesting model in which to study the effects of increasing vessel stiffness on the endothelium. The main focus of our *ex vivo* studies was to characterize the effect of increased sub-endothelial stiffness on endothelial adherens junctions; however, some differences in basement membrane structure were observed between wild type and ELN+/- mice. Specifically, collagen IV in the basement membrane of the WT mouse thoracic aorta was homogenous at all locations. However, collagen IV was aggregated in basement membrane in the upper thoracic aorta from an ELN+/- mouse (Figure 5.2a). In the same ELN+/- vessel, aggregated collagen IV was not observed in the lower thoracic aorta (Figure 5.2b). β-catenin labeling of endothelial cell junctions shows the shorter, less elongated cells characteristic of the upper thoracic aorta (Figure 5.2c) and the more elongated endothelial cells of the lower thoracic aorta (Figure 5.2d); these differences in cell morphology confirm that Figure 5.2a depicts the thoracic aortic basement membrane while Figure 5.2b depicts the abdominal aortic basement membrane.

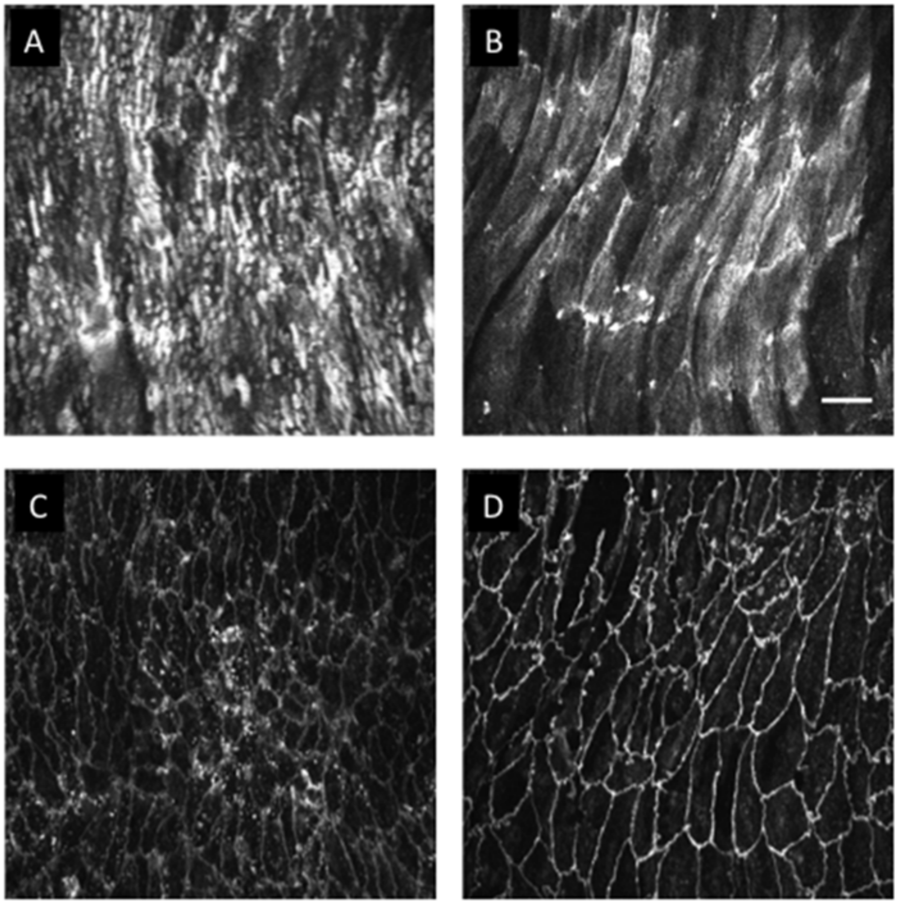

Figure 5.2. Collagen IV aggregation was observed in the basement membrane of the upper thoracic aorta but not the lower thoracic aorta in an ELN+/- mouse. An intact ELN+/- mouse aorta was labeled for collagen IV (a and b) and β-catenin (c and d). Confocal microscopy images were taken of the upper thoracic aorta (a and c) and the lower thoracic aorta (b and d). Scale bar is 25 μm.

These results warrant future investigation. The fact that elastin haploinsufficient mice exhibit accumulated, aggregated aortic sub-endothelial basement membrane has been reported in the literature. In this published study, it was noted that the accumulated basement membrane further separated the endothelium from the diminished internal elastic lamina in ELN+/- mice [44]. However, this study did not report any differences in the basement membrane structure between the thoracic and abdominal aorta, as is shown in Figure 5.2. The fact that collagen IV accumulation was not observed in the abdominal ELN+/- aorta suggests that the effect is not solely due to decreased elastin content, but stimulated by some difference between the thoracic and abdominal aortic sections—possibly intraluminal pressure or vessel extensibility.

Collagen IV aggregation has been observed in the thickened intima of human atherosclerotic plaques [389]. Yet, the effect of aggregated collagen IV on endothelial function is still under investigation [390]. Thus, better understanding of basement membrane deposition or reorganization by the endothelium in the ELN+/- mouse could potentially contribute to our understanding of atherosclerotic plaque development.

5.4.4. Inflammation-induced aortic permeability in wild type and elastin haploinsufficient mice

Characterization of aortic sub-endothelial stiffness in wild type and ELN+/- mice by atomic force microscopy presented in this thesis demonstrate that elastin haploinsufficiency is an appropriate animal model for studying the effect of vessel stiffness on endothelial function. While this work focused on structural changes to actin and cell-cell junctions in intact aortic sections from these mice, studies on vessel permeability in response to systemic inflammation in ELN+/- would also clarify the effect of decreased aortic elasticity on functional barrier loss. Vessel permeability could be determined through intraluminal injection of Evan’s blue dye or fluorescently labeled dextran, followed by imaging of the intact vessel or vessel homogenization [134, 391, 392].

The fact that ELN+/- mice develop high blood pressure contributes a confounding factor; in other words; are the effects observed due to arterial stiffness or adaptation to increased blood pressure? Future studies with this mouse model that utilize concurrent treatment to lower blood pressure would help clarify the contribution of arterial stiffening to endothelial dysfunction. In addition, the contribution of vessel stiffening to integrin-dependent cell-cell junction loss would be of particular interest, since sensing of sub-endothelial stiffness occurs at focal adhesions. The role of increased integrin activation on stiff vessels could be investigated in the ELN+/- mouse model using pharmacological inhibition of the integrin-associated signaling molecule focal adhesion kinase (FAK). This approach would be complicated by the fact that FAK is active at both focal adhesions and cell-cell junctions; however, FAK inhibition has been successful in enhancing endothelial barrier function and preventing tumor cells extravasation in mice [323, 393]. FAK inhibition prior to the stimulation of endothelial cell-cell junction loss would further elucidate the role of sub-endothelial stiffening and increased integrin activation in endothelial permeability.

References

1. Roger, V.L., et al., *Heart disease and stroke statistics-2011 update a report from the american heart association.* Circulation, 2011. **123**(4): p. E18-E209.

2. Kearney, P.M., et al., *Global burden of hypertension: Analysis of worldwide data.* Lancet, 2005. **365**(9455): p. 217-223.

3. Black, H.R.E., William J., *Hypertension: A companion to braunwald's heart disease*, H.R.E. Black, William J., Editor. 2013, Elsevier: Philadelphia, PA.

4. Nichols, W.W., *Clinical measurement of arterial stiffness obtained from noninvasive pressure waveforms.* American Journal of Hypertension, 2005. **18**(1): p. 3S-10S.

5. Gedikli, O., et al., *Effects of prehypertension on arterial stiffness and wave reflections.* Clinical and Experimental Hypertension, 2010. **32**(2): p. 84-89.

6. Laurent, S., et al., *Aortic stiffness is an independent predictor of all-cause and cardiovascular mortality in hypertensive patients.* Hypertension, 2001. **37**(5): p. 1236-1241.

7. Mitchell, G.F., et al., *Arterial stiffness and cardiovascular events the framingham heart study.* Circulation, 2010. **121**(4): p. 505-511.

8. Kaess, B.M., et al., *Aortic stiffness, blood pressure progression, and incident hypertension.* Jama-Journal of the American Medical Association, 2012. **308**(9): p. 875-881.

9. Sutton-Tyrrell, K., et al., *Elevated aortic pulse wave velocity, a marker of arterial stiffness, predicts cardiovascular events in well-functioning older adults.* Circulation, 2005. **111**(25): p. 3384-3390.

10. Laurent, S., et al., *Aortic stiffness is an independent predictor of fatal stroke in essential hypertension.* Stroke, 2003. **34**(5): p. 1203-1206.

11. Weisbrod, R.M., et al., *Arterial stiffening precedes systolic hypertension in diet-induced obesity.* Hypertension, 2013. **62**(6): p. 1105-1110.

12. Crowley, S.D., *The cooperative roles of inflammation and oxidative stress in the pathogenesis of hypertension.* Antioxidants & Redox Signaling, 2014. **20**(1): p. 102-120.

13. Faury, G., et al., *Developmental adaptation of the mouse cardiovascular system to elastin haploinsuffliciency.* Journal of Clinical Investigation, 2003. **112**(9): p. 1419-1428.

14. Marque, V., et al., *Elastic properties and composition of the aortic wall in old spontaneously hypertensive rats.* Hypertension, 1999. **34**(3): p. 415-422.

15. Wajant, H., K. Pfizenmaier, and P. Scheurich, *Tumor necrosis factor signaling.* Cell Death and Differentiation, 2003. **10**(1): p. 45-65.

16. Chrysohoou, C., et al., *Association between prehypertension status and inflammatory markers related to atherosclerotic disease - the attica study.* American Journal of Hypertension, 2004. **17**(7): p. 568-573.

17. Harrison, D.G., et al., *Inflammation, immunity, and hypertension.* Hypertension, 2011. **57**(2): p. 132-140.

18. Chae, C.U., et al., *Blood pressure and inflammation in apparently healthy men.* Hypertension, 2001. **38**(3): p. 399-403.

19. Conrad, K.P., T.M. Miles, and D.F. Benyo, *Circulating levels of immunoreactive cytokines in women with preeclampsia.* American Journal of Reproductive Immunology, 1998. **40**(2): p. 102-111.

20. Guzik, T.J., et al., *Role of the t cell in the genesis of angiotensin ii-induced hypertension and vascular dysfunction.* Journal of Experimental Medicine, 2007. **204**(10): p. 2449-2460.

21. Tran, L.T., K.M. MacLeod, and J.H. McNeill, *Chronic etanercept treatment prevents the development of hypertension in fructose-fed rats.* Molecular and Cellular Biochemistry, 2009. **330**(1-2): p. 219-228.

22. Park, S. and E.G. Lakatta, *Role of inflammation in the pathogenesis of arterial stiffness.* Yonsei Medical Journal, 2012. **53**(2): p. 258-261.

23. Mahmud, A. and J. Feely, *Arterial stiffness is related to systemic inflammation in essential hypertension.* Hypertension, 2005. **46**(5): p. 1118-1122.

24. Hansson, G.K. and A. Hermansson, *The immune system in atherosclerosis.* Nature Immunology, 2011. **12**(3): p. 204-212.

25. Ross, R., *Mechanisms of disease - atherosclerosis - an inflammatory disease.* New England Journal of Medicine, 1999. **340**(2): p. 115-126.

26. Skalen, K., et al., *Subendothelial retention of atherogenic lipoproteins in early atherosclerosis.* Nature, 2002. **417**(6890): p. 750-754.

27. Hansson, G.K., *Mechanisms of disease - inflammation, atherosclerosis, and coronary artery disease.* New England Journal of Medicine, 2005. **352**(16): p. 1685-1695.

28. Amarenco, P., et al., *Atherosclerotic disease of the aortic arch as a risk factor for recurrent ischemic stroke.* New England Journal of Medicine, 1996. **334**(19): p. 1216-1221.

29. Libby, P., P.M. Ridker, and A. Maseri, *Inflammation and atherosclerosis.* Circulation, 2002. **105**(9): p. 1135-1143.

30. Agmon, Y., et al., *Independent association of high blood pressure and aortic atherosclerosis - a population-based study.* Circulation, 2000. **102**(17): p. 2087-2093.

31. Braverman, A.C., *Braunwald's heart disease: A textbook of cardiovascular medicine*, D.P.Z. Douglas L Mann, Peter Libby, Robert O. Bonow, Eugene Braunwald, Editor. 2015, Elsevier Saunders: Philadelphia, PA.

32. Jacob, M.P., *Extracellular matrix remodeling and matrix metalloproteinases in the vascular wall during aging and in pathological conditions.* Biomedicine & Pharmacotherapy, 2003. **57**(5-6): p. 195-202.

33. Dingemans, K.P., et al., *Extracellular matrix of the human aortic media: An ultrastructural histochemical and immunohistochemical study of the adult aortic media.* Anatomical Record, 2000. **258**(1): p. 1-14.

34. Madri, J.A., et al., *The collagenous components of the subendothelium - correlation of structure and function.* Laboratory Investigation, 1980. **43**(4): p. 303-315.

35. Wolinsky, H. and S. Glagov, *Structural basis for the static mechanical properties of the aortic media.* Circulation research, 1964. **14**: p. 400-13.

36. Armentano, R.L., et al., *Assessment of elastin and collagen contribution to aortic elasticity in conscious dogs.* American Journal of Physiology, 1991. **260**(6): p. H1870-H1877.

37. Roach, M.R. and A.C. Burton, *The reason for the shape of the distensibility curves of arteries.* Canadian journal of biochemistry and physiology, 1957. **35**(8): p. 681-90.

38. Zieman, S.J., V. Melenovsky, and D.A. Kass, *Mechanisms, pathophysiology, and therapy of arterial stiffness.* Arteriosclerosis Thrombosis and Vascular Biology, 2005. **25**(5): p. 932-943.

39. Yasmin, et al., *Matrix metalloproteinase-9 (mmp-9), mmp-2, and serum elastase activity are associated with systolic hypertension and arterial stiffness.* Arteriosclerosis Thrombosis and Vascular Biology, 2005. **25**(2): p. 372-378.

40. Greenwald, S.E., *Ageing of the conduit arteries.* Journal of Pathology, 2007. **211**(2): p. 157-172.

41. Curran, M.E., et al., *The elastin gene is disrupted by a translocation associated with supravalvular aortic-stenosis.* Cell, 1993. **73**(1): p. 159-168.

42. Pober, B.R., M. Johnson, and Z. Urban, *Mechanisms and treatment of cardiovascular disease in williams-beuren syndrome.* Journal of Clinical Investigation, 2008. **118**(5): p. 1606-1615.

43. Kozel, B.A., et al., *Williams syndrome predisposes to vascular stiffness modified by antihypertensive use and copy number changes in ncf1.* Hypertension, 2014. **63**(1): p. 74-79.

44. Pezet, M., et al., *Elastin haploinsufficiency induces alternative aging processes in the aorta.* Rejuvenation Research, 2008. **11**(1): p. 97-112.

45. Le, V.P., et al., *Decreased aortic diameter and compliance precedes blood pressure increases in postnatal development of elastin-insufficient mice.* American Journal of Physiology-Heart and Circulatory Physiology, 2011. **301**(1): p. H221-H229.

46. Moncada, S., R.M.J. Palmer, and E.A. Higgs, *Nitric-oxide - physiology, pathophysiology, and pharmacology.* Pharmacological Reviews, 1991. **43**(2): p. 109-142.

47. Shesely, E.G., et al., *Elevated blood pressures in mice lacking endothelial nitric oxide synthase.* Proceedings of the National Academy of Sciences of the United States of America, 1996. **93**(23): p. 13176-13181.

48. Yanagisawa, M., et al., *A novel potent vasoconstrictor peptide produced by vascular endothelial-cells.* Nature, 1988. **332**(6163): p. 411-415.

49. Khimji, A.-K. and D.C. Rockey, *Endothelin-biology and disease.* Cellular Signalling, 2010. **22**(11): p. 1615-1625.

50. Patel, B.M. and A.A. Mehta, *Aldosterone and angiotensin: Role in diabetes and cardiovascular diseases.* European Journal of Pharmacology, 2012. **697**(1-3): p. 1-12.

51. Owens, G.K. and S.M. Schwartz, *Alterations in vascular smooth-muscle mass in the spontaneously hypertensive rat - role of cellular hypertrophy, hyperploidy, and hyperplasia.* Circulation Research, 1982. **51**(3): p. 280-289.

52. Folkow, B., *Physiological-aspects of primary hypertension.* Physiological Reviews, 1982. **62**(2): p. 347-504.

53. Engler, A.J., et al., *Matrix elasticity directs stem cell lineage specification.* Cell, 2006. **126**(4): p. 677-689.

54. Harris, A.K., P. Wild, and D. Stopak, *Silicone-rubber substrata - new wrinkle in the study of cell locomotion.* Science, 1980. **208**(4440): p. 177-179.

55. Pelham, R.J. and Y.L. Wang, *Cell locomotion and focal adhesions are regulated by substrate flexibility.* Proceedings of the National Academy of Sciences of the United States of America, 1997. **94**(25): p. 13661-13665.

56. Tse, J.R. and A.J. Engler, *Preparation of hydrogel substrates with tunable mechanical properties.* Current protocols in cell biology / editorial board, Juan S. Bonifacino ... [et al.], 2010. **Chapter 10**: p. Unit 10.16-Unit 10.16.

57. Cameron, A.R., J.E. Frith, and J.J. Cooper-White, *The influence of substrate creep on mesenchymal stem cell behaviour and phenotype.* Biomaterials, 2011. **32**(26): p. 5979-5993.

58. Discher, D.E., P. Janmey, and Y.L. Wang, *Tissue cells feel and respond to the stiffness of their substrate.* Science, 2005. **310**(5751): p. 1139-1143.

59. Reinhart-King, C.A., *How matrix properties control the self-assembly and maintenance of tissues.* Annals of Biomedical Engineering, 2011. **39**(7): p. 1849-1856.

60. Levental, K.R., et al., *Matrix crosslinking forces tumor progression by enhancing integrin signaling.* Cell, 2009. **139**(5): p. 891-906.

61. Bercoff, J., et al., *In vivo breast tumor detection using transient elastography.* Ultrasound in Medicine and Biology, 2003. **29**(10): p. 1387-1396.

62. Nahon, P., et al., *Liver stiffness measurement in patients with cirrhosis and hepatocellular carcinoma: A case-control study.* European Journal of Gastroenterology & Hepatology, 2009. **21**(2): p. 214-219.

63. Nigam, A., et al., *Relation between conduit vessel stiffness (assessed by tonometry) and endothelial function (assessed by flow-mediated dilatation) in patients with and without coronary heart disease.* American Journal of Cardiology, 2003. **92**(4): p. 395-399.

64. Califano, J.P. and C.A. Reinhart-King, *A balance of substrate mechanics and matrix chemistry regulates endothelial cell network assembly.* Cellular and Molecular Bioengineering, 2008. **1**(2-3): p. 122-132.

65. Engler, A., et al., *Substrate compliance versus ligand density in cell on gel responses.* Biophysical Journal, 2004. **86**(1): p. 617-628.

66. Engler, A.J., et al., *Embryonic cardiomyocytes beat best on a matrix with heart-like elasticity: Scar-like rigidity inhibits beating.* Journal of Cell Science, 2008. **121**(22): p. 3794-3802.

67. Moshayedi, P., et al., *Mechanosensitivity of astrocytes on optimized polyacrylamide gels analyzed by quantitative morphometry.* Journal of Physics-Condensed Matter, 2010. **22**(19).

68. Oakes, P.W., et al., *Neutrophil morphology and migration are affected by substrate elasticity.* Blood, 2009. **114**(7): p. 1387-1395.

69. Peyton, S.R. and A.J. Putnam, *Extracellular matrix rigidity governs smooth muscle cell motility in a biphasic fashion.* Journal of Cellular Physiology, 2005. **204**(1): p. 198-209.

70. Engler, A.J., et al., *Myotubes differentiate optimally on substrates with tissue-like stiffness: Pathological implications for soft or stiff microenvironments.* Journal of Cell Biology, 2004. **166**(6): p. 877-887.

71. Ulrich, T.A., E.M.D. Pardo, and S. Kumar, *The mechanical rigidity of the extracellular matrix regulates the structure, motility, and proliferation of glioma cells.* Cancer Research, 2009. **69**(10): p. 4167-4174.

72. Peyton, S.R., et al., *The use of poly(ethylene glycol) hydrogels to investigate the impact of ecm chemistry and mechanics on smooth muscle cells.* Biomaterials, 2006. **27**(28): p. 4881-4893.

73. Wood, J.A., et al., *The role of substratum compliance of hydrogels on vascular endothelial cell behavior.* Biomaterials, 2011. **32**(22): p. 5056-5064.

74. Yeung, T., et al., *Effects of substrate stiffness on cell morphology, cytoskeletal structure, and adhesion.* Cell Motility and the Cytoskeleton, 2005. **60**(1): p. 24-34.

75. Gray, D.S., J. Tien, and C.S. Chen, *Repositioning of cells by mechanotaxis on surfaces with micropatterned young's modulus.* Journal of Biomedical Materials Research Part A, 2003. **66A**(3): p. 605-614.

76. Califano, J.P. and C.A. Reinhart-King, *Substrate stiffness and cell area predict cellular traction stresses in single cells and cells in contact.* Cellular and Molecular Bioengineering, 2010. **3**(1): p. 68-75.

77. Yeh, Y.T., et al., *Matrix stiffness regulates endothelial cell proliferation through septin 9.* Plos One, 2012. **7**(10).

78. Maruthamuthu, V., et al., *Cell-ecm traction force modulates endogenous tension at cell-cell contacts.* Proceedings of the National Academy of Sciences of the United States of America, 2011. **108**(12): p. 4708-4713.

79. Byfield, F.J., et al., *Endothelial actin and cell stiffness is modulated by substrate stiffness in 2d and 3d.* Journal of Biomechanics, 2009. **42**(8): p. 1114-1119.

80. Stroka, K.M. and H. Aranda-Espinoza, *Endothelial cell substrate stiffness influences neutrophil transmigration via myosin light chain kinase-dependent cell contraction.* Blood, 2011. **118**(6): p. 1632-1640.

81. Burridge, K., et al., *Focal adhesions - transmembrane junctions between the extracellular-matrix and the cytoskeleton.* Annual Review of Cell Biology, 1988. **4**: p. 487-525.

82. Lo, S.H., *Focal adhesions: What's new inside.* Developmental Biology, 2006. **294**(2): p. 280-291.

83. Albelda, S.M. and C.A. Buck, *Integrins and other cell-adhesion molecules.* Faseb Journal, 1990. **4**(11): p. 2868-2880.

84. Hynes, R.O., *Integrins: Bidirectional, allosteric signaling machines.* Cell, 2002. **110**(6): p. 673-687.

85. Hynes, R.O., *Integrins - versatility, modulation, and signaling in cell-adhesion.* Cell, 1992. **69**(1): p. 11-25.

86. Dembo, M. and Y.L. Wang, *Stresses at the cell-to-substrate interface during locomotion of fibroblasts.* Biophysical Journal, 1999. **76**(4): p. 2307-2316.

87. Klotzsch, E., et al., *Fibronectin forms the most extensible biological fibers displaying switchable force-exposed cryptic binding sites.* Proceedings of the National Academy of Sciences of the United States of America, 2009. **106**(43): p. 18267-18272.

88. Morse, E.M., N.N. Brahme, and D.A. Calderwood, *Integrin cytoplasmic tail interactions.* Biochemistry, 2014. **53**(5): p. 810-820.

89. Turner, C.E., *Paxillin and focal adhesion signalling.* Nature Cell Biology, 2000. **2**(12): p. E231-E236.

90. Schaller, M.D., et al., *Pp125fak, a structurally distinctive protein-tyrosine kinase associated with focal adhesions.* Proceedings of the National Academy of Sciences of the United States of America, 1992. **89**(11): p. 5192-5196.

91. Schaller, M.D. and J.T. Parsons, *Focal adhesion kinase and associated proteins.* Current Opinion in Cell Biology, 1994. **6**(5): p. 705-710.

92. Guilluy, C., et al., *The rho gefs larg and gef-h1 regulate the mechanical response to force on integrins.* Nature Cell Biology, 2011. **13**(6): p. 722-U211.

93. Shen, B., M.K. Delaney, and X. Du, *Inside-out, outside-in, and inside-outside-in: G protein signaling in integrin-mediated cell adhesion, spreading, and retraction.* Current Opinion in Cell Biology, 2012. **24**(5): p. 600-606.

94. Ye, F., et al., *Recreation of the terminal events in physiological integrin activation.* Journal of Cell Biology, 2010. **188**(1): p. 157-173.

95. Bouaouina, M., Y. Lad, and D.A. Calderwood, *The n-terminal domains of talin cooperate with the phosphotyrosine binding-like domain to activate beta 1 and beta 3 integrins.* Journal of Biological Chemistry, 2008. **283**(10): p. 6118-6125.

96. Vinogradova, O., et al., *A structural mechanism of integrin alpha(iib)beta(3) "inside-out" activation as regulated by its cytoplasmic face.* Cell, 2002. **110**(5): p. 587-597.

97. Das, M., et al., *Migfilin and filamin as regulators of integrin activation in endothelial cells and neutrophils.* Plos One, 2011. **6**(10).

98. Lynch, C.D., et al., *Filamin depletion blocks endoplasmic spreading and destabilizes force-bearing adhesions.* Molecular Biology of the Cell, 2011. **22**(8): p. 1263-1273.

99. Geiger, B., et al., *Vinculin, an intracellular protein localized at specialized sites where microfilament bundles terminate at cell-membranes.* Proceedings of the National Academy of Sciences of the United States of America-Biological Sciences, 1980. **77**(7): p. 4127-4131.

100. Geiger, B., et al., *Molecular interactions in adherens-type contacts.* Journal of cell science. Supplement, 1987. **8**: p. 251-72.

101. Weller, P.A., et al., *Complete sequence of human vinculin and assignment of the gene to chromosome-10.* Proceedings of the National Academy of Sciences of the United States of America, 1990. **87**(15): p. 5667-5671.

102. Molony, L. and K. Burridge, *Molecular shape and self-association of vinculin and metavinculin.* Journal of Cellular Biochemistry, 1985. **29**(1): p. 31-36.

103. Winkler, J., H. Lunsdorf, and B.M. Jockusch, *The ultrastructure of chicken gizzard vinculin as visualized by high-resolution electron microscopy.* Journal of Structural Biology, 1996. **116**(2): p. 270-277.

104. Johnson, R.P. and S.W. Craig, *An intramolecular association between the head and tail domains of vinculin modulates talin binding.* Journal of Biological Chemistry, 1994. **269**(17): p. 12611-12619.

105. Johnson, R.P. and S.W. Craig, *F-actin binding-site masked by the intramolecular association of vinculin head and tail domains.* Nature, 1995. **373**(6511): p. 261-264.

106. Kroemker, M., et al., *Intramolecular interactions in vinculin control alpha-actinin binding to the vinculin head.* Febs Letters, 1994. **355**(3): p. 259-262.

107. Huttelmaier, S., et al., *The interaction of the cell-contact proteins vasp and vinculin is regulated by phosphatidylinositol-4,5-bisphosphate.* Current Biology, 1998. **8**(9): p. 479-488.

108. Gilmore, A.P. and K. Burridge, *Regulation of vinculin binding to talin and actin by phosphatidyl-inositol-4-5-bisphosphate.* Nature, 1996. **381**(6582): p. 531-535.

109. Turner, C.E., J.R. Glenney, and K. Burridge, *Paxillin - a new vinculin-binding protein present in focal adhesions.* Journal of Cell Biology, 1990. **111**(3): p. 1059-1068.

110. Mandai, K., et al., *Ponsin/sh3p12: An 1-afadin- and vinculin-binding protein localized at cell-cell and cell-matrix adherens junctions.* Journal of Cell Biology, 1999. **144**(5): p. 1001-1017.

111. Kioka, N., et al., *Vinexin: A novel vinculin-binding protein with multiple sh3 domains enhances actin cytoskeletal organization.* Journal of Cell Biology, 1999. **144**(1): p. 59-69.

112. Ingber, D.E., *Cellular mechanotransduction: Putting all the pieces together again.* Faseb Journal, 2006. **20**(7): p. 811-827.

113. Wang, N., J.P. Butler, and D.E. Ingber, *Mechanotransduction across the cell-surface and through the cytoskeleton.* Science, 1993. **260**(5111): p. 1124-1127.

114. del Rio, A., et al., *Stretching single talin rod molecules activates vinculin binding.* Science, 2009. **323**(5914): p. 638-641.

115. Grashoff, C., et al., *Measuring mechanical tension across vinculin reveals regulation of focal adhesion dynamics.* Nature, 2010. **466**(7303): p. 263-U143.

116. Yano, Y., J. Geibel, and B.E. Sumpio, *Tyrosine phosphorylation of pp125(fak) and paxillin in aortic endothelial cells induced by mechanical strain.* American Journal of Physiology-Cell Physiology, 1996. **271**(2): p. C635-C649.

117. Shikata, Y., et al., *Differential effects of shear stress and cyclic stretch on focal adhesion remodeling, site-specific fak phosphorylation, and small gtpases in human lung endothelial cells.* Experimental Cell Research, 2005. **304**(1): p. 40-49.

118. Klein, E.A., et al., *Cell-cycle control by physiological matrix elasticity and in vivo tissue stiffening.* Current Biology, 2009. **19**(18): p. 1511-1518.

119. Sawada, Y., et al., *Force sensing by mechanical extension of the src family kinase substrate p130cas.* Cell, 2006. **127**(5): p. 1015-1026.

120. Ehrlicher, A.J., et al., *Mechanical strain in actin networks regulates filgap and integrin binding to filamin a.* Nature, 2011. **478**(7368): p. 260-U154.

121. DeMali, K.A., X. Sun, and G.A. Bui, *Force transmission at cell-cell and cell-matrix adhesions.* Biochemistry, 2014. **53**(49): p. 7706-7717.

122. Buchsbaum, R.J., *Rho activation at a glance.* Journal of Cell Science, 2007. **120**(7): p. 1149-1152.

123. Beckers, C.M.L., V.W.M. van Hinsbergh, and G.P.v.N. Amerongen, *Driving rho gtpase activity in endothelial cells regulates barrier integrity.* Thrombosis and Haemostasis, 2010. **103**(1): p. 40-55.

124. van Buul, J.D., D. Geerts, and S. Huveneers, *Rho gaps and gefs controling switches in endothelial cell adhesion.* Cell Adhesion & Migration, 2014. **8**(2): p. 108-124.

125. Amado-Azevedo, J., E.T. Valent, and G.P.V.N. Amerongen, *Regulation of the endothelial barrier function: A filum granum of cellular forces, rho-gtpase signaling and microenvironment.* Cell and Tissue Research, 2014. **355**(3): p. 557-576.

126. Amano, M., M. Nakayama, and K. Kaibuchi, *Rho-kinase/rock: A key regulator of the cytoskeleton and cell polarity.* Cytoskeleton, 2010. **67**(9): p. 545-554.

127. Clarke, M. and J.A. Spudich, *Nonmuscle contractile proteins: The role of actin and myosin in cell motility and shape determination.* Annual review of biochemistry, 1977. **46**: p. 797-822.

128. Klee, C.B., T.H. Crouch, and P.G. Richman, *Calmodulin.* Annual Review of Biochemistry, 1980. **49**: p. 489-515.

129. Shen, Q., et al., *Myosin light chain kinase in microvascular endothelial barrier function.* Cardiovascular Research, 2010. **87**(2): p. 272-280.

130. Garcia, J.G.N., et al., *Myosin light chain kinase in endothelium: Molecular cloning and regulation.* American Journal of Respiratory Cell and Molecular Biology, 1997. **16**(5): p. 489-494.

131. Scholey, J.M., K.A. Taylor, and J. Kendrickjones, *Regulation of non-muscle myosin assembly by calmodulin-dependent light chain kinase.* Nature, 1980. **287**(5779): p. 233-235.

132. Kolodney, M.S. and R.B. Wysolmerski, *Isometric contraction by fibroblasts and endothelial-cells in tissue-culture - a quantitative study.* Journal of Cell Biology, 1992. **117**(1): p. 73-82.

133. Goeckeler, Z.M. and R.B. Wysolmerski, *Myosin light-chain kinase-regulated endothelial-cell contraction - the relationship between isometric tension, actin polymerization, and myosin phosphorylation.* Journal of Cell Biology, 1995. **130**(3): p. 613-627.

134. Huynh, J., et al., *Age-related intimal stiffening enhances endothelial permeability and leukocyte transmigration.* Science Translational Medicine, 2011. **3**(112).

135. Ishizaki, T., et al., *Pharmacological properties of y-27632, a specific inhibitor of rho-associated kinases.* Molecular Pharmacology, 2000. **57**(5): p. 976-983.

136. Narumiya, S., T. Ishizaki, and M. Uehata, *Use and properties of rock-specific inhibitor y-27632.* Regulators and Effectors of Small Gtpases, Pt D, 2000. **325**: p. 273-284.

137. Saitoh, M., et al., *Selective-inhibition of catalytic activity of smooth-muscle myosin light chain kinase.* Journal of Biological Chemistry, 1987. **262**(16): p. 7796-7801.

138. Kovacs, M., et al., *Mechanism of blebbistatin inhibition of myosin ii.* Journal of Biological Chemistry, 2004. **279**(34): p. 35557-35563.

139. Katoh, K., Y. Kano, and Y. Noda, *Rho-associated kinase-dependent contraction of stress fibres and the organization of focal adhesions.* Journal of the Royal Society Interface, 2011. **8**(56): p. 305-311.

140. Totsukawa, G., et al., *Distinct roles of rock (rho-kinase) and mlck in spatial regulation of mlc phosphorylation for assembly of stress fibers and focal adhesions in 3t3 fibroblasts.* Journal of Cell Biology, 2000. **150**(4): p. 797-806.

141. Davie, E.W., K. Fujikawa, and W. Kisiel, *The coagulation cascade - initiation, maintenance, and regulation.* Biochemistry, 1991. **30**(43): p. 10363-10370.

142. Essler, M., et al., *Thrombin inactivates myosin light chain phosphatase via rho and its target rho kinase in human endothelial cells.* Journal of Biological Chemistry, 1998. **273**(34): p. 21867-21874.

143. Birukova, A.A., et al., *Role of rho gtpases in thrombin-induced lung vascular endothelial cells barrier dysfunction.* Microvascular Research, 2004. **67**(1): p. 64-77.

144. Garcia, J.G.N., H.W. Davis, and C.E. Patterson, *Regulation of endothelial-cell gap formation and barrier dysfunction - role of myosin light-chain phosphorylation.* Journal of Cellular Physiology, 1995. **163**(3): p. 510-522.

145. van Nieuw Amerongen, G.P., et al., *Thrombin-induced endothelial barrier disruption in intact microvessels: Role of rhoa/rho kinase-myosin phosphatase axis.* American Journal of Physiology-Cell Physiology, 2008. **294**(5): p. C1234-C1241.

146. Krishnan, R., et al., *Substrate stiffening promotes endothelial monolayer disruption through enhanced physical forces.* American Journal of Physiology-Cell Physiology, 2011. **300**(1): p. C146-C154.

147. Birukova, A.A., et al., *Endothelial barrier disruption and recovery is controlled by substrate stiffness.* Microvascular Research, 2013. **87**: p. 50-57.

148. Dejana, E., *Endothelial cell-cell junctions: Happy together.* Nature Reviews Molecular Cell Biology, 2004. **5**(4): p. 261-270.

149. Lampugnani, M.G., et al., *The molecular-organization of endothelial-cell to cell-junctions - differential association of plakoglobin, beta-catenin, and alpha-catenin with vascular endothelial cadherin (ve-cadherin).* Journal of Cell Biology, 1995. **129**(1): p. 203-217.

150. Navarro, P., et al., *Catenin-dependent and -independent functions of vascular endothelial cadherin.* Journal of Biological Chemistry, 1995. **270**(52): p. 30965-30972.

151. Bazzoni, G. and E. Dejana, *Endothelial cell-to-cell junctions: Molecular organization and role in vascular homeostasis.* Physiological Reviews, 2004. **84**(3): p. 869-901.

152. Lampugnani, M.G., et al., *A novel endothelial-specific membrane-protein is a marker of cell cell contacts.* Journal of Cell Biology, 1992. **118**(6): p. 1511-1522.

153. Takeichi, M., *Cadherins - a molecular family important in selective cell-cell adhesion.* Annual Review of Biochemistry, 1990. **59**: p. 237-252.

154. Takeichi, M., *The cadherins - cell cell-adhesion molecules controlling animal morphogenesis.* Development, 1988. **102**(4): p. 639-&.

155. Navarro, P., L. Ruco, and E. Dejana, *Differential localization of ve- and n-cadherins in human endothelial cells: Ve-cadherin competes with n-cadherin for junctional localization.* Journal of Cell Biology, 1998. **140**(6): p. 1475-1484.

156. Angst, B.D., C. Marcozzi, and A.I. Magee, *The cadherin superfamily: Diversity in form and function.* Journal of Cell Science, 2001. **114**(4): p. 629-641.

157. Yap, A.S., W.M. Brieher, and B.M. Gumbiner, *Molecular and functional analysis of cadherin-based adherens junctions.* Annual Review of Cell and Developmental Biology, 1997. **13**: p. 119-146.

158. Kowalczyk, A.P., et al., *Ve-cadherin and desmoplakin are assembled into dermal microvascular endothelial intercellular junctions: A pivotal role for plakoglobin in the recruitment of desmoplakin to intercellular junctions.* Journal of Cell Science, 1998. **111**: p. 3045-3057.

159. Gates, J. and M. Peifer, *Can 1000 reviews be wrong? Actin, alpha-catenin, and adherens junctions.* Cell, 2005. **123**(5): p. 769-772.

160. Ozawa, M. and R. Kemler, *Molecular-organization of the uvomorulin-catenin complex.* Journal of Cell Biology, 1992. **116**(4): p. 989-996.

161. Meng, W. and M. Takeichi, *Adherens junction: Molecular architecture and regulation.* Cold Spring Harbor Perspectives in Biology, 2009. **1**(6).

162. Rimm, D.L., et al., *Alpha(1)(e)-catenin is an actin-binding and actin-bundling protein mediating the attachment of f-actin to the membrane adhesion complex.* Proceedings of the National Academy of Sciences of the United States of America, 1995. **92**(19): p. 8813-8817.

163. Drees, F., et al., *Alpha-catenin is a molecular switch that binds e-cadherin-beta-catenin and regulates actin-filament assembly.* Cell, 2005. **123**(5): p. 903-915.

164. Yamada, S., et al., *Deconstructing the cadherin-catenin-actin complex.* Cell, 2005. **123**(5): p. 889-901.

165. Buckley, C.D., et al., *The minimal cadherin-catenin complex binds to actin filaments under force.* Science, 2014. **346**(6209): p. 600-+.

166. Kemler, R., *From cadherins to catenins - cytoplasmic protein interactions and regulation of cell-adhesion.* Trends in Genetics, 1993. **9**(9): p. 317-321.

167. McCrea, P.D., C.W. Turck, and B. Gumbiner, *A homolog of the armadillo protein in drosophila (plakoglobin) associated with e-cadherin.* Science, 1991. **254**(5036): p. 1359-1361.

168. Butz, S., et al., *Plakoglobin and beta-catenin - distinct but closely related.* Science, 1992. **257**(5073): p. 1142-1144.

169. Cattelino, A., et al., *The conditional inactivation of the beta-catenin gene in endothelial cells causes a defective vascular pattern and increased vascular fragility.* Journal of Cell Biology, 2003. **162**(6): p. 1111-1122.

170. Behrens, J., et al., *Functional interaction of beta-catenin with the transcription factor lef-1.* Nature, 1996. **382**(6592): p. 638-642.

171. Dejana, E., *The role of wnt signaling in physiological and pathological angiogenesis.* Circulation Research, 2010. **107**(8): p. 943-952.

172. Beckers, C.M.L., et al., *Nuclear targeting of beta-catenin and p120ctn during thrombin-induced endothelial barrier dysfunction.* Cardiovascular Research, 2008. **79**(4): p. 679-688.

173. Taddei, A., et al., *Endothelial adherens junctions control tight junctions by ve-cadherin-mediated upregulation of claudin-5.* Nature Cell Biology, 2008. **10**(8): p. 923-934.

174. Yao, M., et al., *Force-dependent conformational switch of alpha-catenin controls vinculin binding.* Nature Communications, 2014. **5**.

175. Barry, A.K., et al., *Alpha-catenin cytomechanics - role in cadherin-dependent adhesion and mechanotransduction.* Journal of Cell Science, 2014. **127**(8): p. 1779-1791.

176. Yonemura, S., et al., *Alpha-catenin as a tension transducer that induces adherens junction development.* Nature Cell Biology, 2010. **12**(6): p. 533-U35.

177. le Duc, Q., et al., *Vinculin potentiates e-cadherin mechanosensing and is recruited to actin-anchored sites within adherens junctions in a myosin ii-dependent manner.* Journal of Cell Biology, 2010. **189**(7): p. 1107-1115.

178. Huveneers, S., et al., *Vinculin associates with endothelial ve-cadherin junctions to control force-dependent remodeling.* Journal of Cell Biology, 2012. **196**(5): p. 641-652.

179. Ladoux, B., et al., *Strength dependence of cadherin-mediated adhesions.* Biophysical Journal, 2010. **98**(4): p. 534-542.

180. Liu, Z.J., et al., *Mechanical tugging force regulates the size of cell-cell junctions.* Proceedings of the National Academy of Sciences of the United States of America, 2010. **107**(22): p. 9944-9949.

181. Wojciak-Stothard, B. and A.J. Ridley, *Rho gtpases and the regulation of endothelial permeability.* Vascular Pharmacology, 2002. **39**(4-5): p. 187-199.

182. Carbajal, J.M., et al., *Rock mediates thrombin's endothelial barrier dysfunction.* American Journal of Physiology-Cell Physiology, 2000. **279**(1): p. C195-C204.

183. Wojciak-Stothard, B., et al., *Regulation of tnf-alpha-induced reorganization of the actin cytoskeleton and cell-cell junctions by rho, rac, and cdc42 in human endothelial cells.* Journal of Cellular Physiology, 1998. **176**(1).

184. Marcos-Ramiro, B., D. Garcia-Weber, and J. Millan, *Tnf-induced endothelial barrier dysruption: Beyond actin and rho.* Thrombosis and Haemostasis, 2014. **112**(5).

185. McKenzie, J.A.G. and A.J. Ridley, *Roles of rho/rock and mlck in tnf-alpha-induced changes in endothelial morphology and permeability.* Journal of Cellular Physiology, 2007. **213**(1).

186. Fernandez-Martin, L., et al., *Crosstalk between reticular adherens junctions and platelet endothelial cell adhesion molecule-1 regulates endothelial barrier function.* Arteriosclerosis Thrombosis and Vascular Biology, 2012. **32**(8): p. E90-U141.

187. Millan, J., et al., *Adherens junctions connect stress fibres between adjacent endothelial cells.* Bmc Biology, 2010. **8**.

188. Nwariaku, F.E., et al., *Rho inhibition decreases tnf-induced endothelial mapk activation and monolayer permeability.* Journal of Applied Physiology, 2003. **95**(5): p. 1889-1895.

189. Li, J.M. and A.M. Shah, *Endothelial cell superoxide generation: Regulation and relevance for cardiovascular pathophysiology.* American Journal of Physiology-Regulatory Integrative and Comparative Physiology, 2004. **287**(5): p. R1014-R1030.

190. Droge, W., *Free radicals in the physiological control of cell function.* Physiological Reviews, 2002. **82**(1): p. 47-95.

191. Mohazzabh, K.M., P.M. Kaminski, and M.S. Wolin, *Nadh oxidoreductase is a major source of superoxide anion in bovine coronary-artery endothelium.* American Journal of Physiology, 1994. **266**(6): p. H2568-H2572.

192. Dworakowski, R., S.P. Alom-Ruiz, and A.M. Shah, *Nadph oxidase-derived reactive oxygen species in the regulation of endothelial phenotype.* Pharmacological Reports, 2008. **60**(1): p. 21-28.

193. Gorlach, A., et al., *A gp91phox containing nadph oxidase selectively expressed in endothelial cells is a major source of oxygen radical generation in the arterial wall.* Circulation Research, 2000. **87**(1): p. 26-32.

194. Bedard, K. and K.-H. Krause, *The nox family of ros-generating nadph oxidases: Physiology and pathophysiology.* Physiological Reviews, 2007. **87**(1): p. 245-313.

195. Li, J.M., et al., *Essential role of the nadph oxidase subunit p47(phox) in endothelial cell superoxide production in response to phorbol ester and tumor necrosis factor-alpha.* Circulation Research, 2002. **90**(2): p. 143-150.

196. Gregg, D., F.M. Rauscher, and P.J. Goldschmidt-Clermont, *Rac regulates cardiovascular superoxide through diverse molecular interactions: More than a binary gtp switch.* American Journal of Physiology-Cell Physiology, 2003. **285**(4): p. C723-C734.

197. Sawada, N., Y. Li, and J.K. Liao, *Novel aspects of the roles of rac1 gtpase in the cardiovascular system.* Current Opinion in Pharmacology, 2010. **10**(2): p. 116-121.

198. Dalle-Donne, I., et al., *The actin cytoskeleton response to oxidants: From small heat shock protein phosphorylation to changes in the redox state of actin itself.* Free Radical Biology and Medicine, 2001. **31**(12): p. 1624-1632.

199. Lum, H. and K.A. Roebuck, *Oxidant stress and endothelial cell dysfunction.* American Journal of Physiology-Cell Physiology, 2001. **280**(4): p. C719-C741.

200. Crawford, L.E., et al., *Superoxide mediated actin response in post-hypoxic endothelial cells.* Journal of Biological Chemistry, 1996. **271**(43): p. 26863-26867.

201. Moldovan, L., et al., *Redox changes of cultured endothelial cells and actin dynamics.* Circulation Research, 2000. **86**(5): p. 549-557.

202. Taulet, N., V.D. Delorme-Walker, and C. DerMardirossian, *Reactive oxygen species regulate protrusion efficiency by controlling actin dynamics.* Plos One, 2012. **7**(8).

203. Esser, S., et al., *Vascular endothelial growth factor induces ve-cadherin tyrosine phosphorylation in endothelial cells.* Journal of Cell Science, 1998. **111**: p. 1853-1865.

204. Andriopoulou, P., et al., *Histamine induces tyrosine phosphorylation of endothelial cell-to-cell adherens junctions.* Arteriosclerosis Thrombosis and Vascular Biology, 1999. **19**(10): p. 2286-2297.

205. Nwariaku, F.E., et al., *Nadph oxidase mediates vascular endothelial cadherin phosphorylation and endothelial dysfunction.* Blood, 2004. **104**(10): p. 3214-3220.

206. van Wetering, S., et al., *Reactive oxygen species mediate rac-induced loss of cell-cell adhesion in primary human endothelial cells.* Journal of Cell Science, 2002. **115**(9): p. 1837-1846.

207. Bogatcheva, N.V., et al., *Phorbol esters increase mlc phosphorylation and actin remodeling in bovine lung endothelium without increased contraction.* American Journal of Physiology-Lung Cellular and Molecular Physiology, 2003. **285**(2): p. L415-L426.

208. Waschke, J., et al., *Protein kinase c-mediated endothelial barrier regulation is caveolin-1-dependent.* Histochemistry and Cell Biology, 2006. **126**(1): p. 17-26.

209. Bogatcheva, N.V., et al., *Caldesmon is a cytoskeletal target for pkc in endothelium.* Journal of Cellular Biochemistry, 2006. **99**(6): p. 1593-1605.

210. Niedel, J.E., L.J. Kuhn, and G.R. Vandenbark, *Phorbol diester receptor co-purifies with protein kinase-c.* Proceedings of the National Academy of Sciences of the United States of America-Biological Sciences, 1983. **80**(1): p. 36-40.

211. Stasek, J.E., C.E. Patterson, and J.G.N. Garcia, *Protein-kinase-c phosphorylates caldesmon77 and vimentin and enhances albumin permeability across cultured*

bovine pulmonary-artery endothelial-cell monolayers. Journal of Cellular Physiology, 1992. **153**(1): p. 62-75.

212. Sandoval, R., et al., *Ca2+ signalling and pkc alpha activate increased endothelial permeability by disassembly of ve-cadherin junctions.* Journal of Physiology-London, 2001. **533**(2): p. 433-445.

213. Krishnan, R., et al., *Substrate stiffening promotes endothelial monolayer disruption through enhanced physical forces.* American Journal of Physiology-Cell Physiology, 2011. **300**(1): p. C146-C154.

214. Mambetsariev, I., et al., *Stiffness-activated gef-h1 expression exacerbates lps-induced lung inflammation.* Plos One, 2014. **9**(4).

215. Lee, K., et al., *Matrix compliance regulates rac1b localization, nadph oxidase assembly, and epithelial-mesenchymal transition.* Molecular Biology of the Cell, 2012. **23**(20): p. 4097-4108.

216. del Pozo, M.A., et al., *Adhesion to the extracellular matrix regulates the coupling of the small gtpase rac to its effector pak.* Embo Journal, 2000. **19**(9): p. 2008-2014.

217. del Pozo, M.A., et al., *Integrins regulate rac targeting by internalization of membrane domains.* Science, 2004. **303**(5659): p. 839-842.

218. Zhang, A.Y., et al., *Lipid raft clustering and redox signaling platform formation in coronary arterial endothelial cells.* Hypertension, 2006. **47**(1): p. 74-80.

219. Yang, B.H. and V. Rizzo, *Tnf-alpha potentiates protein-tyrosine nitration through activation of nadph oxidase and enos localized in membrane rafts and caveolae of bovine aortic endothelial cells.* American Journal of Physiology-Heart and Circulatory Physiology, 2007. **292**(2): p. H954-H962.

220. Szczygiel, A.M., et al., *Elasticity changes anti-correlate with no production for human endothelial cells stimulated with tnf-alpha.* Pflugers Archiv-European Journal of Physiology, 2012. **463**(3).

221. Kondrikov, D., et al., *Beta-actin association with endothelial nitric-oxide synthase modulates nitric oxide and superoxide generation from the enzyme.* Journal of Biological Chemistry, 2010. **285**(7).

222. Fels, J., et al., *Cortical actin nanodynamics determines nitric oxide release in vascular endothelium.* Plos One, 2012. **7**(7).

223. Lang, F., *Stiff endothelial cell syndrome in vascular inflammation and mineralocorticoid excess.* Hypertension, 2011. **57**(2).

224. Evans, E. and A. Yeung, *Apparent viscosity and cortical tension of blood granulocytes determined by micropipet aspiration.* Biophysical Journal, 1989. **56**(1): p. 151-160.

225. Jones, W.R., et al., *Alterations in the young's modulus and volumetric properties of chondrocytes isolated from normal and osteoarthritic human cartilage.* Journal of Biomechanics, 1999. **32**(2): p. 119-127.

226. Henon, S., et al., *A new determination of the shear modulus of the human erythrocyte membrane using optical tweezers.* Biophysical Journal, 1999. **76**(2): p. 1145-1151.

227. Sleep, J., et al., *Elasticity of the red cell membrane and its relation to hemolytic disorders: An optical tweezers study.* Biophysical Journal, 1999. **77**(6): p. 3085-3095.

228. Guck, J., et al., *The optical stretcher: A novel laser tool to micromanipulate cells.* Biophysical Journal, 2001. **81**(2): p. 767-784.

229. Wottawah, F., et al., *Optical rheology of biological cells.* Physical Review Letters, 2005. **94**(9).

230. Bausch, A.R., et al., *Local measurements of viscoelastic parameters of adherent cell surfaces by magnetic bead microrheometry.* Biophysical Journal, 1998. **75**(4): p. 2038-2049.

231. Wang, N. and D.E. Ingber, *Probing transmembrane mechanical coupling and cytomechanics using magnetic twisting cytometry.* Biochemistry and Cell Biology-Biochimie Et Biologie Cellulaire, 1995. **73**(7-8): p. 327-335.

232. Binnig, G., C.F. Quate, and C. Gerber, *Atomic force microscope.* Physical Review Letters, 1986. **56**(9): p. 930-933.

233. Costa, K.D. and F.C.P. Yin, *Analysis of indentation: Implications for measuring mechanical properties with atomic force microscopy.* Journal of Biomechanical Engineering-Transactions of the Asme, 1999. **121**(5): p. 462-471.

234. Gerber, C. and H.P. Lang, *How the doors to the nanoworld were opened.* Nature Nanotechnology, 2006. **1**(1): p. 3-5.

235. Cappella, B. and G. Dietler, *Force-distance curves by atomic force microscopy.* Surface Science Reports, 1999. **34**(1-3): p. 1-104.

236. Butt, H.J., B. Cappella, and M. Kappl, *Force measurements with the atomic force microscope: Technique, interpretation and applications.* Surface Science Reports, 2005. **59**(1-6): p. 1-152.

237. Muller, D.J. and Y.F. Dufrene, *Atomic force microscopy as a multifunctional molecular toolbox in nanobiotechnology.* Nature Nanotechnology, 2008. **3**(5): p. 261-269.

238. A-Hassan, E., et al., *Relative microelastic mapping of living cells by atomic force microscopy.* Biophysical Journal, 1998. **74**(3): p. 1564-1578.

239. Costa, K.D., *Single-cell elastography: Probing for disease with the atomic force microscope.* Disease Markers, 2003. **19**(2-3): p. 139-154.

240. Vinckier, A. and G. Semenza, *Measuring elasticity of biological materials by atomic force microscopy.* Febs Letters, 1998. **430**(1-2): p. 12-16.

241. Hinterdorfer, P. and Y.F. Dufrene, *Detection and localization of single molecular recognition events using atomic force microscopy.* Nature Methods, 2006. **3**(5): p. 347-355.

242. Lee, G.U., D.A. Kidwell, and R.J. Colton, *Sensing discrete streptavidin biotin interactions with atomic force microscopy.* Langmuir, 1994. **10**(2): p. 354-357.

243. Drake, B., et al., *Imaging crystals, polymers, and processes in water with the atomic force microscope* Science, 1989. **243**(4898): p. 1586-1589.

244. Piner, R.D., et al., *"Dip-pen" nanolithography.* Science, 1999. **283**(5402): p. 661-663.

245. Fuhr, G., et al., *Levitation, holding, and rotation of cells within traps made by high-frequency fields.* Biochimica Et Biophysica Acta, 1992. **1108**(2): p. 215-223.

246. Voldman, J., *Electrical forces for microscale cell manipulation.* Annual Review of Biomedical Engineering, 2006. **8**: p. 425-454.

247. Green, N.G., H. Morgan, and J.J. Milner, *Manipulation and trapping of sub-micron bioparticles using dielectrophoresis.* Journal of Biochemical and Biophysical Methods, 1997. **35**(2): p. 89-102.

248. Hughes, M.P., et al., *Manipulation of herpes simplex virus type 1 by dielectrophoresis.* Biochimica Et Biophysica Acta-General Subjects, 1998. **1425**(1): p. 119-126.

249. Voldman, J., et al., *A microfabrication-based dynamic array cytometer.* Analytical Chemistry, 2002. **74**(16): p. 3984-3990.

250. Taff, B.M. and J. Voldman, *A scalable addressable positive-dielectrophoretic cell-sorting array.* Analytical Chemistry, 2005. **77**(24): p. 7976-7983.

251. Becker, F.F., et al., *Separation of human breast-cancer cells from blood by differential dielectric affinity.* Proceedings of the National Academy of Sciences of the United States of America, 1995. **92**(3): p. 860-864.

252. Talary, M.S., et al., *Dielectrophoretic separation and enrichment of cd34+ cell subpopulation from bone-marrow and peripheral-blood stem-cells.* Medical & Biological Engineering & Computing, 1995. **33**(2): p. 235-237.

253. Rosenthal, A. and J. Voldman, *Dielectrophoretic traps for single-particle patterning.* Biophysical Journal, 2005. **88**(3): p. 2193-2205.

254. Gray, D.S., et al., *Dielectrophoretic registration of living cells to a microelectrode array.* Biosensors & Bioelectronics, 2004. **19**(7): p. 771-780.

255. Albrecht, D.R., et al., *Photo- and electropatterning of hydrogel-encapsulated living cell arrays.* Lab on a Chip, 2005. **5**(1): p. 111-118.

256. Pethig, R., et al., *Dielectrophoretic studies of the activation of human t lymphocytes using a newly developed cell profiling system.* Electrophoresis, 2002. **23**(13): p. 2057-2063.

257. Pethig, R. and M.S. Talary, *Dielectrophoretic detection of membrane morphology changes in jurkat t-cells undergoing etoposide-induced apoptosis.* Iet Nanobiotechnology, 2007. **1**(1): p. 2-9.

258. Marszalek, P. and T.Y. Tsong, *Cell fission and formation of mini cell-bodies by high-frequency alternating electric-field.* Biophysical Journal, 1995. **68**(4): p. 1218-1221.

259. Sukhorukov, V.L., H. Mussauer, and U. Zimmermann, *The effect of electrical deformation forces on the electropermeabilization of erythrocyte membranes in low- and high-conductivity media.* Journal of Membrane Biology, 1998. **163**(3): p. 235-245.

260. MacQueen, L.A., M.D. Buschmann, and M.R. Wertheimer, *Mechanical properties of mammalian cells in suspension measured by electro-deformation.* Journal of Micromechanics and Microengineering, 2010. **20**(6).

261. Guido, I., M.S. Jaeger, and C. Duschl, *Dielectrophoretic stretching of cells allows for characterization of their mechanical properties.* European Biophysics Journal with Biophysics Letters, 2011. **40**(3): p. 281-288.

262. Chen, J., et al., *Electrodeformation for single cell mechanical characterization.* Journal of Micromechanics and Microengineering, 2011. **21**(5).

263. Sims, C.E. and N.L. Allbritton, *Analysis of single mammalian cells on-chip.* Lab on a Chip, 2007. **7**(4): p. 423-440.

264. Yi, C.Q., et al., *Microfluidics technology for manipulation and analysis of biological cells.* Analytica Chimica Acta, 2006. **560**(1-2): p. 1-23.

265. Ingber, D.E., *Tensegrity i. Cell structure and hierarchical systems biology.* Journal of Cell Science, 2003. **116**(7): p. 1157-1173.

266. Wakatsuki, T., et al., *Effects of cytochalasin d and latrunculin b on mechanical properties of cells.* Journal of Cell Science, 2001. **114**(5): p. 1025-1036.

267. Coughlin, M.F., et al., *Cytoskeletal stiffness, friction, and fluidity of cancer cell lines with different metastatic potential.* Clinical & Experimental Metastasis, 2013. **30**(3): p. 237-250.

268. Wang, X.B., et al., *Theoretical and experimental investigations of the interdependence of the dielectric, dielectrophoretic and electrorotational behavior of colloidal particles.* Journal of Physics D-Applied Physics, 1993. **26**(2): p. 312-322.

269. Gagnon, Z.R., *Cellular dielectrophoresis: Applications to the characterization, manipulation, separation and patterning of cells.* Electrophoresis, 2011. **32**(18): p. 2466-2487.

270. Gascoyne, P.R.C., et al., *Dielectrophoretic separation of cancer cells from blood.* Ieee Transactions on Industry Applications, 1997. **33**(3): p. 670-678.

271. Huang, Y., et al., *Introducing dielectrophoresis as a new force field for field-flow fractionation.* Biophysical Journal, 1997. **73**(2): p. 1118-1129.

272. Huang, C., et al., *Electrokinetic measurements of dielectric properties of membrane for apoptotic hl-60 cells on chip-based device.* Biomedical Microdevices, 2007. **9**(3): p. 335-343.

273. Rosenthal, A., B.M. Taff, and J. Voldman, *Quantitative modeling of dielectrophoretic traps.* Lab on a Chip, 2006. **6**(4): p. 508-515.

274. Voldman, J., et al., *Design and analysis of extruded quadrupolar dielectrophoretic traps.* Journal of Electrostatics, 2003. **57**(1): p. 69-90.

275. McCain, M.L., et al., *Cooperative coupling of cell-matrix and cell-cell adhesions in cardiac muscle.* Proceedings of the National Academy of Sciences of the United States of America, 2012. **109**(25): p. 9881-9886.

276. Solon, J., et al., *Fibroblast adaptation and stiffness matching to soft elastic substrates.* Biophys J, 2007. **93**(12): p. 4453-61.

277. Otsu, N., *A threshold selection method from gray-level histograms.* IEEE Transactions on Systems, Man and Cybernetics, 1979. **SMC-9**(1): p. 62-66.

278. Mittal, N., A. Rosenthal, and J. Voldman, *Ndep microwells for single-cell patterning in physiological media.* Lab on a Chip, 2007. **7**(9): p. 1146-1153.

279. Guck, J., et al., *Optical deformability as an inherent cell marker for testing malignant transformation and metastatic competence.* Biophysical Journal, 2005. **88**(5): p. 3689-3698.

280. Hochmuth, R.M., *Micropipette aspiration of living cells.* Journal of Biomechanics, 2000. **33**(1).

281. Alenghat, F.J., et al., *Analysis of cell mechanics in single vinculin-deficient cells using a magnetic tweezer.* Biochemical and Biophysical Research Communications, 2000. **277**(1): p. 93-99.

282. Jaasma, M.J., W.M. Jackson, and T.M. Keaveny, *Measurement and characterization of whole-cell mechanical behavior.* Annals of Biomedical Engineering, 2006. **34**(5): p. 748-758.

283. Ingber, D.E., *Tensegrity: The architectural basis of cellular mechanotransduction.* Annual Review of Physiology, 1997. **59**: p. 575-599.

284. Wang, N., *Mechanical interactions among cytoskeletal filaments.* Hypertension, 1998. **32**(1): p. 162-165.

285. Graham, D.M., M.A. Messerli, and R. Pethig, *Spatial manipulation of cells and organelles using single electrode dielectrophoresis.* Biotechniques, 2012. **52**(1): p. 39-43.

286. Hunt, T.P. and R.M. Westervelt, *Dielectrophoresis tweezers for single cell manipulation.* Biomedical Microdevices, 2006. **8**(3): p. 227-230.

287. Menachery, A., et al., *Dielectrophoretic tweezer for isolating and manipulating target cells.* Iet Nanobiotechnology, 2011. **5**(1): p. 1-7.

288. Rettig, J.R. and A. Folch, *Large-scale single-cell trapping and imaging using microwell arrays.* Analytical Chemistry, 2005. **77**(17): p. 5628-5634.

289. Ameri, S.K., et al., *All electronic approach for high-throughput cell trapping and lysis with electrical impedance monitoring.* Biosensors & Bioelectronics, 2014. **54**: p. 462-467.

290. Weis, S., et al., *Endothelial barrier disruption by vegf-mediated src activity potentiates tumor cell extravasation and metastasis.* Journal of Cell Biology, 2004. **167**(2): p. 223-229.

291. Weis, S.M., *Vascular permeability in cardiovascular disease and cancer.* Current Opinion in Hematology, 2008. **15**(3): p. 243-249.

292. Tabas, I., K.J. Williams, and J. Boren, *Subendothelial lipoprotein retention as the initiating process in atherosclerosis - update and therapeutic implications.* Circulation, 2007. **116**(16): p. 1832-1844.

293. Libby, P., et al., *Inflammation in atherosclerosis from pathophysiology to practice.* Journal of the American College of Cardiology, 2009. **54**(23): p. 2129-2138.

294. Worrall, N.K., et al., *Tnf-alpha causes reversible in vivo systemic vascular barrier dysfunction via no-dependent and -independent mechanisms.* American Journal of Physiology-Heart and Circulatory Physiology, 1997. **273**(6): p. H2565-H2574.

295. Skoog, T., et al., *Plasma tumour necrosis factor-alpha and early carotid atherosclerosis in healthy middle-aged men.* European Heart Journal, 2002. **23**(5): p. 376-383.

296. Bruunsgaard, H., et al., *Ageing, tumour necrosis factor-alpha (tnf-alpha) and atherosclerosis.* Clinical and Experimental Immunology, 2000. **121**(2): p. 255-260.

297. Del Porto, F., et al., *Response to anti-tumour necrosis factor alpha blockade is associated with reduction of carotid intima-media thickness in patients with active rheumatoid arthritis.* Rheumatology, 2007. **46**(7): p. 1111-1115.

298. Najjar, S.S., et al., *Pulse wave velocity is an independent predictor of the longitudinal increase in systolic blood pressure and of incident hypertension in the baltimore longitudinal study of aging.* Journal of the American College of Cardiology, 2008. **51**(14): p. 1377-1383.

299. Duprez, D.A. and J.N. Cohn, *Arterial stiffness as a risk factor for coronary atherosclerosis.* Current atherosclerosis reports, 2007. **9**(2): p. 139-44.

300. Willum-Hansen, T., et al., *Prognostic value of aortic pulse wave velocity as index of arterial stiffness in the general population.* Circulation, 2006. **113**(5): p. 664-70.

301. Mattace-Raso, F.U.S., et al., *Arterial stiffness and risk of coronary heart disease and stroke - the rotterdam study.* Circulation, 2006. **113**(5): p. 657-663.

302. Mong, P.Y., et al., *Activation of rho kinase by tnf-alpha is required for jnk activation in human pulmonary microvascular endothelial cells.* Journal of Immunology, 2008. **180**(1): p. 550-558.

303. Peng, J., et al., *Protein kinase c-alpha signals p115rhogef phosphorylation and rhoa activation in tnf-alpha-induced mouse brain microvascular endothelial cell barrier dysfunction.* Journal of Neuroinflammation, 2011. **8**.

304. Tinsley, J.H., F.A. Hunter, and E.W. Childs, *Pkc and mlck-dependent, cytokine-induced rat coronary endothelial dysfunction.* Journal of Surgical Research, 2009. **152**(1): p. 76-83.

305. Garcia, J.G.N., F.M. Pavalko, and C.E. Patterson, *Vascular endothelial-cell activation and permeability responses to thrombin.* Blood Coagulation & Fibrinolysis, 1995. **6**(7): p. 609-626.

306. Bogatcheva, N.V., J.G.N. Garcia, and A.D. Verin, *Molecular mechanisms of thrombin-induced endothelial cell permeability.* Biochemistry-Moscow, 2002. **67**(1): p. 75-84.

307. Peloquin, J., et al., *Indentation measurements of the subendothelial matrix in bovine carotid arteries.* Journal of Biomechanics, 2011. **44**(5): p. 815-821.

308. Wagenseil, J.E., et al., *Reduced vessel elasticity alters cardiovascular structure and function in newborn mice.* Circulation Research, 2009. **104**(10): p. 1217-U233.

309. Oldenburg, J. and J. de Rooij, *Mechanical control of the endothelial barrier.* Cell and Tissue Research, 2014. **355**(3): p. 545-555.

310. Leerberg, J.M. and A.S. Yap, *Vinculin, cadherin mechanotransduction and homeostasis of cell-cell junctions.* Protoplasma, 2013. **250**(4): p. 817-829.

311. Thomas, W.A., et al., *Alpha-catenin and vinculin cooperate to promote high e-cadherin-based adhesion strength.* Journal of Biological Chemistry, 2013. **288**(7): p. 4957-4969.

312. Huveneers, S. and J. de Rooij, *Mechanosensitive systems at the cadherin-f-actin interface.* Journal of Cell Science, 2013. **126**(2): p. 403-413.

313. Kaushik, G., et al., *Vinculin network-mediated cytoskeletal remodeling regulates contractile function in the aging heart.* Science translational medicine, 2015. **7**(292): p. 292ra99-292ra99.

314. Wu, D.-J., et al., *Effects of fasudil on early atherosclerotic plaque formation and established lesion progression in apolipoprotein e-knockout mice.* Atherosclerosis, 2009. **207**(1): p. 68-73.

315. Shi, J. and L. Wei, *Rho kinases in cardiovascular physiology and pathophysiology: The effect of fasudil.* Journal of Cardiovascular Pharmacology, 2013. **62**(4): p. 341-354.

316. Eisa-Beygi, S. and X.-Y. Wen, *Could pharmacological curtailment of the rhoa/rho-kinase pathway reverse the endothelial barrier dysfunction associated with ebola virus infection?* Antiviral Research, 2015. **114**: p. 53-56.

317. Dejana, E., F. Orsenigo, and M.G. Lampugnani, *The role of adherens junctions and ve-cadherin in the control of vascular permeability.* Journal of Cell Science, 2008. **121**(13): p. 2115-2122.

318. Sidibe, A. and B.A. Imhof, *Ve-cadherin phosphorylation decides: Vascular permeability or diapedesis.* Nature Immunology, 2014. **15**(3): p. 215-217.

319. Angelini, D.J., et al., *Tnf-alpha increases tyrosine phosphorylation of vascular endothelial cadherin and opens the paracellular pathway through fyn activation in human lung endothelia.* American Journal of Physiology-Lung Cellular and Molecular Physiology, 2006. **291**(6): p. L1232-L1245.

320. Abaci, H.E., et al., *Recapitulating physiological and pathological shear stress and oxygen to model vasculature in health and disease.* Scientific Reports, 2014. **4**.

321. Sun, X., et al., *Enhanced interaction between focal adhesion and adherens junction proteins: Involvement in sphingosine 1-phosphate-induced endothelial barrier enhancement.* Microvascular Research, 2009. **77**(3): p. 304-313.

322. Chen, X.L., et al., *Vegf-induced vascular permeability is mediated by fak.* Developmental Cell, 2012. **22**(1): p. 146-157.

323. Jean, C., et al., *Inhibition of endothelial fak activity prevents tumor metastasis by enhancing barrier function.* Journal of Cell Biology, 2014. **204**(2): p. 247-263.

324. Schaller, M.D., *Cellular functions of fak kinases: Insight into molecular mechanisms and novel functions.* Journal of Cell Science, 2010. **123**(7): p. 1007-1013.

325. Zebda, N., O. Dubrovskyi, and K.G. Birukov, *Focal adhesion kinase regulation of mechanotransduction and its impact on endothelial cell functions.* Microvascular Research, 2012. **83**(1): p. 71-81.

326. Senyo, S.E., Y.E. Koshman, and B. Russell, *Stimulus interval, rate and direction differentially regulate phosphorylation for mechanotransduction in neonatal cardiac myocytes.* Febs Letters, 2007. **581**(22): p. 4241-4247.

327. Lim, S.-T.S., *Nuclear fak: A new mode of gene regulation from cellular adhesions.* Molecules and Cells, 2013. **36**(1): p. 1-6.

328. Levental, I., P.C. Georges, and P.A. Janmey, *Soft biological materials and their impact on cell function.* Soft Matter, 2007. **3**(3): p. 299-306.

329. Chaudhuri, O., et al., *Substrate stress relaxation regulates cell spreading.* Nature Communications, 2015. **6**.

330. Kohn, J.C., et al., *Cooperative effects of matrix stiffness and fluid shear stress on endothelial cell behavior.* Biophysical Journal, 2015. **108**(3): p. 471-478.

331. Galie, P.A., et al., *Application of multiple levels of fluid shear stress to endothelial cells plated on polyacrylamide gels.* Lab on a Chip, 2015. **15**(4): p. 1205-1212.

332. Ray, P.D., B.-W. Huang, and Y. Tsuji, *Reactive oxygen species (ros) homeostasis and redox regulation in cellular signaling.* Cellular Signalling, 2012. **24**(5): p. 981-990.

333. Briones, A.M. and R.M. Touyz, *Oxidative stress and hypertension: Current concepts.* Current Hypertension Reports, 2010. **12**(2): p. 135-142.

334. Judkins, C.P., et al., *Direct evidence of a role for nox2 in superoxide production, reduced nitric oxide bioavailability, and early atherosclerotic plaque formation in apoe(-/-) mice.* American Journal of Physiology-Heart and Circulatory Physiology, 2010. **298**(1): p. H24-H32.

335. Violi, F., et al., *Reduced atherosclerotic burden in subjects with genetically determined low oxidative stress.* Arteriosclerosis Thrombosis and Vascular Biology, 2013. **33**(2): p. 406-+.

336. Moy, A.B., et al., *Phorbol ester-mediated pulmonary artery endothelial barrier dysfunction through regulation of actin cytoskeletal mechanics.* American Journal of Physiology-Lung Cellular and Molecular Physiology, 2004. **287**(1): p. L153-L167.

337. Brandes, R.P., N. Weissmann, and K. Schroeder, *Nox family nadph oxidases in mechano-transduction: Mechanisms and consequences.* Antioxidants & Redox Signaling, 2014. **20**(6): p. 887-898.

338. McNally, J.S., et al., *Role of xanthine oxidoreductase and nad(p)h oxidase in endothelial superoxide production in response to oscillatory shear stress.* American Journal of Physiology-Heart and Circulatory Physiology, 2003. **285**(6): p. H2290-H2297.

339. Tzima, E., et al., *Activation of rac1 by shear stress in endothelial cells mediates both cytoskeletal reorganization and effects on gene expression.* Embo Journal, 2002. **21**(24): p. 6791-6800.

340. Yeh, L.H., et al., *Shear-induced tyrosine phosphorylation in endothelial cells requires rac1-dependent production of ros.* American Journal of Physiology-Cell Physiology, 1999. **276**(4): p. C838-C847.

341. Usatyuk, P.V. and V. Natarajan, *Regulation of reactive oxygen species-induced endothelial cell-cell and cell-matrix contacts by focal adhesion kinase and adherens junction proteins.* American Journal of Physiology-Lung Cellular and Molecular Physiology, 2005. **289**(6): p. L999-L1010.

342. Kevil, C.G., et al., *Role of cadherin internalization in hydrogen peroxide-mediated endothelial permeability.* Free Radical Biology and Medicine, 1998. **24**(6): p. 1015-1022.

343. Huie, R.E. and S. Padmaja, *The reaction of no with superoxide.* Free Radical Research Communications, 1993. **18**(4): p. 195-199.

344. Walsh, T., T. Donnelly, and D. Lyons, *Impaired endothelial nitric oxide bioavailability: A common link between aging, hypertension, and atherogenesis?* Journal of the American Geriatrics Society, 2009. **57**(1): p. 140-145.

345. Landmesser, U., et al., *Oxidation of tetrahydrobiopterin leads to uncoupling of endothelial cell nitric oxide synthase in hypertension.* Journal of Clinical Investigation, 2003. **111**(8): p. 1201-1209.

346. Cosentino, F., et al., *Reactive oxygen species mediate endothelium-dependent relaxations in tetrahydrobiopterin-deficient mice.* Arteriosclerosis Thrombosis and Vascular Biology, 2001. **21**(4): p. 496-502.

347. Stuehr, D., S. Pou, and G.M. Rosen, *Oxygen reduction by nitric-oxide synthases.* Journal of Biological Chemistry, 2001. **276**(18): p. 14533-14536.

348. Turko, I.V. and F. Murad, *Protein nitration in cardiovascular diseases.* Pharmacological Reviews, 2002. **54**(4): p. 619-634.

349. Heymes, C., et al., *Increased myocardial nadph oxidase activity in human heart failure.* Journal of the American College of Cardiology, 2003. **41**(12): p. 2164-2171.

350. Barry-Lane, P.A., et al., *P47phox is required for atherosclerotic lesion progression in apoe(-/-) mice.* Journal of Clinical Investigation, 2001. **108**(10): p. 1513-1522.

351. Azumi, H., et al., *Superoxide generation in directional coronary atherectomy specimens of patients with angina pectoris - important role of nad(p)h oxidase.* Arteriosclerosis Thrombosis and Vascular Biology, 2002. **22**(11): p. 1838-1844.

352. Madamanchi, N.R., A. Vendrov, and M.S. Runge, *Oxidative stress and vascular disease.* Arteriosclerosis Thrombosis and Vascular Biology, 2005. **25**(1): p. 29-38.

353. Drummond, G.R., et al., *Combating oxidative stress in vascular disease: Nadph oxidases as therapeutic targets.* Nature Reviews Drug Discovery, 2011. **10**(6): p. 453-471.

354. Sugamura, K. and J.F. Keaney, Jr., *Reactive oxygen species in cardiovascular disease.* Free Radical Biology and Medicine, 2011. **51**(5): p. 978-992.

355. van Popele, N.M., et al., *Association between arterial stiffness and atherosclerosis - the rotterdam study.* Stroke, 2001. **32**(2): p. 454-460.

356. Wykretowicz, A., et al., *Augmentation index, pulse pressure amplification and superoxide anion production in patients with coronary artery disease.* International Journal of Cardiology, 2005. **99**(2): p. 289-294.

357. Goel, G., et al., *Phorbol esters: Structure, biological activity, and toxicity in animals.* International Journal of Toxicology, 2007. **26**(4): p. 279-288.

358. Bass, D.A., et al., *Flow cytometric studies of oxidative product formation by neutrophils - a graded response to membrane stimulation.* Journal of Immunology, 1983. **130**(4): p. 1910-1917.

359. Carter, W.O., P.K. Narayanan, and J.P. Robinson, *Intracellular hydrogen-peroxide and superoxide anion detection in endothelial-cells.* Journal of Leukocyte Biology, 1994. **55**(2): p. 253-258.

360. Naghavi, M., et al., *Global, regional, and national age-sex specific all-cause and cause-specific mortality for 240 causes of death, 1990-2013: A systematic analysis for the global burden of disease study 2013.* Lancet, 2015. **385**(9963): p. 117-171.

361. Bautista, L.E., et al., *Independent association between inflammatory markers (c-reactive protein, interleukin-6, and tnf-alpha) and essential hypertension.* Journal of Human Hypertension, 2005. **19**(2): p. 149-154.

362. DeMali, K.A., K. Wennerberg, and K. Burridge, *Integrin signaling to the actin cytoskeleton.* Current Opinion in Cell Biology, 2003. **15**(5): p. 572-582.

363. Ren, X.D., W.B. Kiosses, and M.A. Schwartz, *Regulation of the small gtp-binding protein rho by cell adhesion and the cytoskeleton.* Embo Journal, 1999. **18**(3): p. 578-585.

364. Pietuch, A. and A. Janshoff, *Mechanics of spreading cells probed by atomic force microscopy.* Open Biology, 2013. **3**(7).

365. Kain, S.R., et al., *Green fluorescent protein as a reporter of gene-expression and protein localization.* Biotechniques, 1995. **19**(4): p. 650-655.

366. Huveneers, S., M.J.A.P. Daemen, and P.L. Hordijk, *Between rho(k) and a hard place the relation between vessel wall stiffness, endothelial contractility, and cardiovascular disease.* Circulation Research, 2015. **116**(5): p. 895-908.

367. Belmin, J., et al., *Age-related-changes in endothelial permeability and distribution volume of albumin in rat aorta.* American Journal of Physiology, 1993. **264**(3): p. H679-H685.

368. van Nieuw Amerongen, G.P., et al., *Involvement of rho kinase in endothelial barrier maintenance.* Arteriosclerosis Thrombosis and Vascular Biology, 2007. **27**(11): p. 2332-2339.

369. Schnittler, H., et al., *Actin filament dynamics and endothelial cell junctions: The ying and yang between stabilization and motion.* Cell and Tissue Research, 2014. **355**(3): p. 529-543.

370. Hakanpaa, L., et al., *Endothelial destabilization by angiopoietin-2 via integrin beta 1 activation.* Nature Communications, 2015. **6**.

371. Churchill, E., et al., *Pkc isozymes in chronic cardiac disease: Possible therapeutic targets?* Annual Review of Pharmacology and Toxicology, 2008. **48**: p. 569-599.

372. Brownlee, M., *Biochemistry and molecular cell biology of diabetic complications.* Nature, 2001. **414**(6865): p. 813-820.

373. Bagi, Z., A. Koller, and G. Kaley, *Superoxide-no interaction decreases flow- and agonist-induced dilations of coronary arterioles in type 2 diabetes mellitus.* American Journal of Physiology-Heart and Circulatory Physiology, 2003. **285**(4): p. H1404-H1410.

374. Peters, K., et al., *Molecular basis of endothelial dysfunction in sepsis.* Cardiovascular Research, 2003. **60**(1): p. 49-57.

375. Trachootham, D., J. Alexandre, and P. Huang, *Targeting cancer cells by ros-mediated mechanisms: A radical therapeutic approach?* Nature Reviews Drug Discovery, 2009. **8**(7): p. 579-591.

376. Maki-Petaja, K.M., et al., *Rheumatoid arthritis is associated with increased aortic pulse-wave velocity, which is reduced by anti-tumor necrosis factor-alpha therapy.* Circulation, 2006. **114**(11): p. 1185-1192.

377. Campuzano, V., et al., *Reduction of nadph-oxidase activity ameliorates the cardiovascular phenotype in a mouse model of williams-beuren syndrome.* Plos Genetics, 2012. **8**(2).

378. Del Campo, M., et al., *Hemizygosity at the ncf1 gene in patients with williams-beuren syndrome decreases their risk of hypertension.* American Journal of Human Genetics, 2006. **78**(4): p. 533-542.

379. Adam, A., A. Sharenko, and P. Vincent, *Tyrosine phosphorylation of ve-cadherin following activation of src-family kinases is not sufficient to decrease endothelial barrier function.* Faseb Journal, 2009. **23**.

380. Gavard, J. and J.S. Gutkind, *Vegf controls endothelial-cell permeability by promoting the beta-arrestin-dependent endocytosis of ve-cadherin.* Nature Cell Biology, 2006. **8**(11): p. 1223-U17.

381. Schulte, D., et al., *Stabilizing the ve-cadherin-catenin complex blocks leukocyte extravasation and vascular permeability.* Embo Journal, 2011. **30**(20): p. 4157-4170.

382. Wang, Y.X., et al., *Integrins regulate ve-cadherin and catenins: Dependence of this regulation on src,, but not on ras.* Proceedings of the National Academy of Sciences of the United States of America, 2006. **103**(6): p. 1774-1779.

383. Geyer, H., et al., *Characterization of human vascular endothelial cadherin glycans.* Glycobiology, 1999. **9**(9): p. 915-925.

384. Lampugnani, M.G., et al., *Cell confluence regulates tyrosine phosphorylation of adherens junction components in endothelial cells.* Journal of Cell Science, 1997. **110**: p. 2065-2077.

385. Suzuki, S., K. Sano, and H. Tanihara, *Diversity of the cadherin family - evidence for 8 new cadherins in nervous-tissue.* Cell Regulation, 1991. **2**(4): p. 261-270.

386. Scott, D.W. and R.P. Patel, *Endothelial heterogeneity and adhesion molecules n-glycosylation: Implications in leukocyte trafficking in inflammation.* Glycobiology, 2013. **23**(6): p. 622-633.

387. Kitazume, S., et al., *Alpha 2,6-sialic acid on platelet endothelial cell adhesion molecule (pecam) regulates its homophilic interactions and downstream antiapoptotic signaling.* Journal of Biological Chemistry, 2010. **285**(9): p. 6515-6521.

388. Liwosz, A., T. Lei, and M.A. Kukuruzinska, *N-glycosylation affects the molecular organization and stability of e-cadherin junctions.* Journal of Biological Chemistry, 2006. **281**(32): p. 23138-23149.

389. Katsuda, S., et al., *Collagens in human atherosclerosis - immunohistochemical analysis using collagen type-specific antibodies.* Arteriosclerosis and Thrombosis, 1992. **12**(4): p. 494-502.

390. Duner, P., et al., *Increased aldehyde-modification of collagen type iv in symptomatic plaques - a possible cause of endothelial dysfunction.* Atherosclerosis, 2015. **240**(1): p. 26-32.

391. Amerongen, G.P.V., et al., *Simvastatin improves disturbed endothelial barrier function.* Circulation, 2000. **102**(23): p. 2803-2809.

392. You, D., et al., *Increase in vascular permeability and vasodilation are critical for proangiogenic effects of stem cell therapy.* Circulation, 2006. **114**(4): p. 328-338.

393. Grinnell, K.L. and E.O. Harrington, *Interplay between fak, pkc delta, and p190rhogap in the regulation of endothelial barrier function.* Microvascular Research, 2012. **83**(1): p. 12-21.

Vita

Full name: Rebecca Jane Urbano
Place and Date of Birth: Kennett Square, PA on June 1, 1984

EDUCATION

Drexel University	Philadelphia, PA
Ph.D. in Mechanical Engineering	Graduated August 2015
BS/MS in Biomedical Engineering	Graduated June 2007

PROFESSIONAL EXPERIENCE

Merck & Co., Inc.—Bioprocess Analytical and Formulation Sciences	
Staff Biologist	November 2008 to July 2011
Biochemist	July 2007 to November 2008
Centocor, Inc. (Janssen)—Clinical Pharmacology and Experimental Medicine	
Part-Time Assistant Scientist	September 2006 to July 2007
Co-op student	April to September 2006
Merck & Co., Inc.—Viral Vaccine Engineering Services	
Co-op student	March to September 2005
Centocor, Inc. (Janssen)—Process Development	
Co-op student	May to September 2004

PUBLICATIONS & PATENTS

R. Lownes Urbano and A. Morss Clyne. Cell-substrate interactions. In *Molecular and Cellular Biomechanics*. Ed. Bradley Layton, Pan Stanford Publishing.

R. Lownes Urbano and A. Morss Clyne. An inverted dielectrophoretic device for analysis of attached single cell stiffness (in review).

A. Canver, O. Ngo, **R. Lownes Urbano**, A. Morss Clyne. Endothelial cell collective migration depends on substrate stiffness via ROCK and α_5 pathways (in review).

R. Lownes Urbano and A. Morss Clyne. Patent application filed, April 2015. "Dielectrophoretic device for cell mechanics".

A. Bertolotti-Ciarlet, W. Wang, **R. Lownes,** P. Pristatsky, Y. Fang, T. McKelvey, Y. Li, J. Drummond, T. Prueksaritanont, J. Vlasak. Impact of methionine oxidation on the binding of human IgG1 to FcRn and Fc gamma receptors. Molecular Immunology. 2009 May; 46(8-9): 1878-82.

POSTER PRESENTATIONS

R. Lownes Urbano, C. Furia, P. Osei-Owusu, and A. Morss Clyne. TNF-α-induced adherens junction disruption increases with substrate stiffness in endothelial cell monolayers. Biomedical Engineering Society (Cellular and Molecular Bioengineering), 2015.

R. Lownes Urbano and A. Morss Clyne. Microfabrication of a dielectrophoretic device for high-throughput analysis of single cell stiffness. Biomedical Engineering Society, 2013.

R. Lownes Urbano and A. Morss Clyne. A second generation dielectrophoretic device to quantify endothelial cell mechanical properties under normal and diabetic conditions. Vasculata, 2012.